

# **STUDIES OF AMORPHOUS SILICON**

by

**Robert Donald McLeod**

A thesis  
presented to the University of Manitoba  
in partial fulfillment of the  
requirements for the degree of  
Doctor of Philosophy  
in  
Electrical Engineering

Winnipeg, Manitoba, 1985

© Robert Donald McLeod, 1985

Advisor: Dr. H.C. Card

Examiners:

Dr. K.C. Kao

Dr. H.D. Gesser

Dr. A.M. Gole

Dr. D.L. Pulfrey

STUDIES OF AMORPHOUS SILICON

BY

ROBERT DONALD McLEOD

A thesis submitted to the Faculty of Graduate Studies of  
the University of Manitoba in partial fulfillment of the requirements  
of the degree of

DOCTOR OF PHILOSOPHY

© 1985

Permission has been granted to the LIBRARY OF THE UNIVERSITY OF MANITOBA to lend or sell copies of this thesis, to the NATIONAL LIBRARY OF CANADA to microfilm this thesis and to lend or sell copies of the film, and UNIVERSITY MICROFILMS to publish an abstract of this thesis.

The author reserves other publication rights, and neither the thesis nor extensive extracts from it may be printed or otherwise reproduced without the author's written permission.

## ABSTRACT

This thesis concerns itself with a study of amorphous silicon ( $a-Si$ ). Primarily it was an experimental investigation. Basic electrical and optical properties were obtained for  $a-SiN_x:H$ , a material of increasing commercial interest for xerography. Two deposition systems were developed; i) an electron beam evaporation system which attempted to facilitate the incorporation of hydrogen into the growing film by reactive evaporation, and ii) a microwave glow discharge system where the plasma could be contained by an externally applied dc magnetic field. The evaporation system was only moderately successful, whereas the microwave glow discharge was very successful in producing high quality films which displayed a considerable variation of properties governed primarily by the plasma confinement. The effect of hydrogen incorporation in  $a-Si$  was exploited to advance  $a-Si:H$  systems for archival storage. The material was found to be well suited as a material for both optical and electron beam interrogated systems. The theoretical contribution of this thesis is in advancing a discussion of fractal geometry which we consider as providing an alternative perspective for the study of disordered semiconductors, in particular of hydrogenated amorphous silicon. Experimentally observed anomalies such as transient photoconductivity, linear electronic density of states, and the hydrogen dependence of the dc conductivity were discussed in terms of a fractal structure which undergoes a fractal to Euclidean crossover.

## **ACKNOWLEDGEMENT**

I would like to express my sincere appreciation to my friend and mentor Dr. H.C. Card. I am also deeply indebted to my friends and colleges, in particular W. Pries and S.R. Mejia. I would like to acknowledge the financial support of the Natural Sciences and Engineering Research Council of Canada as well as the financial and moral support of my wife and best friend Sandra.

## TABLE OF CONTENTS

	Page
ABSTRACT	iv
ACKNOWLEDGEMENTS	v
Chapter 1: General Overview	1
1.1: Introduction	1
1.2: Methods of Fabrication	1
1.3: Characterization Techniques	3
1.4: Application of Amorphous Semiconductors	4
1.5: Basic Device Physics	4
1.6: References for Chapter 1	9
Chapter 2: Undoped Amorphous $SiN_x$ Alloy Semiconductors	11
2.1: Introductory Remarks	11
2.2: Experimental Methods and Characterization	12
2.3: Discussion of Optical Measurements	14
2.4: Discussion of Electrical Measurements	17
2.5: Conclusions of Chapter 2	22
2.6: References for Chapter 2	23
Chapter 3: Microwave Deposition of $a-Si:H$	25
3.1: The Effect of Deposition Parameters on $a-Si:H$ Fabricated by Microwave Glow Discharge Techniques	26
3.1.1: Introductory Remarks	26
3.1.2: System Configuration	26
3.1.3: Experimental Conditions	28
3.1.4: Film Characterization	29
3.2: Microwave Plasmas under Electron Cyclotron Resonance	32
3.2.1: Introductory Remarks	32
3.2.2: System Configuration	33
3.2.3: Preliminary Experimental Results	36

3.2.4: Film Characterization	39
3.3: Conclusions for Chapter 3	42
3.4: References for Chapter 3	43
Chapter 4: Activated Reactive Evaporation of $a-Si:H$	44
4.1: Introductory Remarks	44
4.2: Experimental Techniques	45
4.3: Film Characterization	46
4.4: Conclusions of Chapter 4	50
4.5: References for Chapter 4	51
Chapter 5: $a-Si:H$ for Archival Storage	52
5.1: Introductory Remarks	52
5.2: Archival Storage Media	52
5.3: Experimental Details	53
5.4: Discussion	53
5.5: Conclusions of Chapter 5	57
5.6: References for Chapter 5	58
Chapter 6: Interpretation of Amorphous Silicon Behavior using Fractal Geometry	59
6.1: Introduction	59
6.2: Background: Fractal Geometry	59
6.3: Experimentally Observed Properties of $a-Si:H$	64
6.3.1: Experimental DOS	65
6.3.2: Dispersive Transport and $a-Si:H$	66
6.3.3: Experimental Dark Conductivity	67
6.4: Fractals and $a-Si:H$	67
6.4.1: Fractals and the DOS	68
6.4.1.1: Accounting for the linear DOS; a $k$ -space approach	69
6.4.1.2: Accounting for the linear DOS; a real space approach	74
6.4.1.3: Nonhomogeneous Fractals as Appropriate Representations of $a-Si:H$	76
6.4.2: Fractals and Dispersive Transport	82
6.4.3: Fractals and the dc Conductivity	90
6.4.3.1: The percolation probability	91

6.4.3.2: $\sigma(p)$ ; The conductivity	92
6.4.3.3: $s_{av}$ ; The mean cluster size	93
6.4.3.4: $l_{av}$ ; The characteristic length	93
6.4.3.5: Percolation and $a-Si:H$	94
6.5: Conclusions of Chapter 6	97
6.6: References for Chapter 6	98
Chapter 7: Conclusions	100

## LIST OF FIGURES

- [2.1] Refractive index vs. photon energy for undoped  $a-SiN_x:H$  films, with composition  $x$  (N/Si ratio) as a parameter. ( $0 \leq x \leq 0.64$ )
- [2.2] Optical absorption coefficient vs. photon energy for undoped  $a-SiN_x:H$  films with nitrogen content  $x$  as a parameter. ( $0 \leq x \leq 0.64$ )
- [2.3] Dark conductivity vs. temperature for undoped  $a-SiN_x:H$  films, with composition  $x$  as a parameter.
- [2.4] Optical energy gap of undoped  $a-SiN_x:H$  films, with composition  $x$  as a parameter.
- [2.5] Refractive index at  $h\nu = 0.5 \text{ eV}$  of undoped  $a-SiN_x:H$  films vs. composition  $x$ .
- [2.6] The  $B$ -parameter in  $\alpha h\nu = B(h\nu - E_{opt}^2)$  vs. nitrogen content  $x$  for  $a-SiN_x:H$  films.  $B \approx (\Delta E)^{-1}$  where  $\Delta E$  is the extent of the tail states.
- [2.7] Conductivity parameter  $\sigma_1$  for extended-state conduction as in the first term of Equ.2.3, determined from experiment at high temperature, assuming  $\sigma_d \approx \sigma_0 \exp(-E_1/kT)$ .
- [2.8] Conductivity in the low temperature region interpreted according to Mott's model of variable-range hopping at  $E_f$ . Plotted as  $\log(\sigma T^{1/2})$  vs.  $T^{-1/4}$  for comparison with theory.
  
- [3.1] Configuration of the coaxial line-type microwave plasma system.
- [3.2] Configuration of the short-circuited waveguide chamber
- [3.3] Variation of the magnetic field profile along the axis of the waveguide chamber with coil current  $I_c$ .
- [3.4] Variation of the deposition rate profile along the axis of the chamber with coil current  $I_c$ . Horizontal orientation: solid tokens.
- [3.5] Dark conductivity and photo-conductivity of  $a-Si:H$  films grown in a microwave glow discharge as a function of magnetic field (coil current).
- [3.6] The effect of the magnetic field on the infrared absorption spectrum of  $a-Si:H$  grown in a microwave glow discharge.

- [3.7] SEM micrograph illustrating the columnar structure of one of the H films.
  - [3.8] Modified short-circuited waveguide configuration.
  - [3.9] Variation of the magnetic field profile along the axis of the chamber as a function of coil current.
  - [3.10] Overall system configuration.
  - [3.11] A scaled up design for industrial applications.
  - [3.12] Dependence of the  $[SiH]$  and  $[H_\alpha]$  emission intensities upon magnetic field current for a 10%  $SiH_4$  in  $H_2$  gas mixture.
  - [3.13] Photographic illustration of the effect of the magnetic field upon the confinement of the plasma. a)15 A coil current. b)17 A coil current. c)19 A coil current. d)21 A coil current.
  - [3.14] Electrical and optical properties of  $a-Si:H$  thin films as functions of magnetic confinement (coil current).
- 
- [4.1] Schematic of the ARE deposition system.
  - [4.2] Deposition rate ( $\mu m/min$ ) vs. partial pressure of  $H_2$ . Dashed line represents the 90% confidence limits.
  - [4.3] Conductivity and extended state activation energy vs. partial pressure of  $H_2$ , corresponding to probe voltages of 0 and 200 volts.
  - [4.4] Refractive index at 0.5 eV (long wavelength) vs. partial pressure of  $H_2$ , corresponding to probe voltage of 0 and 200 volts.
  - [4.5] Optical gap  $E_{opt}$  vs. partial pressure of  $H_2$ , corresponding to probe voltages of 0 and 200 volts.
- 
- [5.1] Ratio of change in optical reflectivity to original reflectivity, measured at  $\lambda = 632.8 \text{ nm}$ , and the electrical conductivity (in  $S \text{ cm}^{-1}$ ) of  $a-Si:H$  film (thickness  $0.3 \mu m$ ) vs. remaining  $H$  content following  $Ar$  laser irradiation (514 nm) or thermal annealing. Dashed line indicates theoretical calculations based upon a simple two layer film model [5.7].
  - [5.2] Refractive index  $n$  and the extinction coefficient  $k$  vs.  $H$  content in  $a-Si:H$  film ( $d = 0.3 \mu m$ ).

- [5.3] Normalized excess temperature profiles ( $T - T_{ambient}$ ) during steady-state argon laser irradiation for various Gaussian intensity distributions  $I = I_0 \exp(-r^2/\omega^2)$  with  $T_{max} = I_0 \pi^{1/2} \omega / 2k$  where  $\omega$  = beam waist and  $k$  = thermal conductivity.
- [6.1] Generator used in the construction of a fractal curve.
- [6.2] Generation of the fractal curve by iteratively applying the generator of Fig.6.1.
- [6.3] Measured length of the fractal curve as a function of the measuring rod.
- [6.4] Generation of a fractal by iteratively removing the inner triangular regions.
- [6.5] Density of the fractal pattern as a function of the measuring unit
- [6.6] Dependence of the dc conductivity upon the incorporated  $H$  in  $a-Si:H$  alloys [6.14]
- [6.7] Density of vibrational states. The solid curve represents the crossover from the phonon to fracton regimes [6.17].
- [6.8] Vibrational density of states for pure  $a-Si$  [6.18].
- [6.9]  $N(E)$  vs.  $E$  illustrating the consequences of fractal geometry.
- [6.10] Crossover of the electronic density of states at the energy corresponding to the correlation length  $\xi$ .
- [6.11] Experimentally determined vibrational density of states for fused silica [6.22].
- [6.12] Effect of hydrogen on the electronic DOS and hence  $\tilde{d}$  [6.9].
- [6.13] Hydrogen partial vibrational density of states for  $a-Si:H$  [6.18].
- [6.14] Transient photo-conductivity [6.25]. a) Experimental setup. b) Normal transport. c) Dispersive transport.
- [6.15] Time evolution of the charge packet or carrier density profile [6.25]. a) Normal transport. b) Dispersive transport.
- [6.16] The Vandalized Grid [6.25].
- [6.17] The conductance parameter in the percolation model.

[6.18] Behavior of the characteristic parameters associated with the percolation model;  $s_{av}, J_{av}, \sigma(p), P(p)$  [6.25].

[6.19] The modified percolation model for a  $-Si:H$

# CHAPTER 1

## GENERAL OVERVIEW

### 1.1. Introduction

In this chapter, our aim is not to be comprehensive in describing the present state of amorphous semiconducting materials. Instead, this chapter will provide an outline of current fabrication techniques, experimental characterization methods, and will touch upon some of the applications of amorphous materials, topics which are relevant to the material of later chapters. An attempt will be made to delineate current theories and models that have been proposed to describe the amorphous state. Since most work on amorphous semiconductors has focused on tetrahedrally bonded amorphous solids, much of the following discussion will be based upon hydrogenated amorphous silicon ( $a-Si:H$ ) as a representative material. This is also consistent with the theme of  $a-Si:H$  properties which form the experimental basis of this thesis. An additional reason for basing the discussion on  $a-Si:H$  is that it has been widely studied by other workers and an abundance of literature is available for this material.

### 1.2. Methods of Fabrication

One of the striking differences between amorphous and crystalline silicon is that the absorption coefficient for crystalline silicon in the visible spectrum is approximately an order of magnitude less than that for the amorphous material. This implies that if crystalline silicon were to be used as solar cell material it would have to be approximately  $50\mu m$  thick, whereas if amorphous silicon were to be used it would only have to be  $1\mu m$  thick in order to absorb the same amount of incident radiation. For this reason, much of the development in amorphous materials has been restricted to thin films. The chronological development of thin film fabrication techniques is roughly as follows; electron-beam or thermal evaporation [1.1], dc and rf sputtering [1.2,1.3], reactive sputtering [1.4], and plasma enhanced chemical vapor deposition (PECVD) [1.5]. Other fabrication techniques are basically combinations or variations of these methods of deposition [1.6,1.7]. Details of these fabrication techniques can be found in S. Mejia's M.Sc dissertation [1.8].

Each method of deposition has advantages and disadvantages. For example,<sup>1</sup> the e-beam evaporation systems have attributes of high deposition rates and excellent film uniformity, but suffer from poor electrical properties primarily due to an extremely high density of states within the bandgap [1.9]. It is accepted that the incorporation of atomic hydrogen in the  $a-Si$  network reduces the density of these gap states and enhances both the electrical properties and the optoelectronic properties. Several evaporation systems have been suggested, which attempt to facilitate the incorporation of atomic hydrogen [1.10].<sup>2</sup> Sputter deposited material suffers from ion and electron bombardment, but in reactive plasmas, where  $H_2$  is added to the sputtering gas, incorporation of atomic hydrogen is facilitated.<sup>3</sup> The difficulty of  $H$  incorporation is overcome in PECVD systems where the gas employed is usually some combination of  $SiH_4$  and  $H_2$ . Disadvantages associated with PECVD or glow discharge (GD) systems as they are often referred to, is the difficulty associated with incorporating materials such as  $Al$  or  $Sn$  which are not directly available in a gaseous form.<sup>4</sup> Variations of CVD techniques (eg. HOMO-CVD [1.11]) have been developed which could potentially overcome some of these difficulties, but associated with HOMO-CVD is the disadvantage of it being a hot wall technique as opposed to conventional CVD methods which employ an rf susceptor.<sup>2</sup> One distinct advantage of these CVD methods is the wide selection of metal-organic reactants which can be used in the vapor stream to incorporate a variety of metals.

<sup>2</sup> The largest single factor in the development of  $a-Si:H$  technology was the fortuitous discovery of the beneficial effects of the incorporation of atomic hydrogen. For this reason the PECVD fabrication techniques with their inherent  $H$  incorporation ability have dictated both the academic and industrial development of the  $a-Si:H$  technology. Until recently, the development of photovoltaic devices has dominated the philosophy of desirable amorphous semiconductor properties. With a photovoltaic emphasis in mind, PECVD systems came to the forefront in fabrication technology. In Chapter 2, we discuss our experimental research on the optoelectronic properties of amorphous silicon-nitrogen alloys, which are expected to find many other applications in device technology.

PECVD is a complex process that is still not well understood. Nevertheless, its wide use for thin film fabrication has stimulated research aimed at understanding and improving this technique. Major contributions towards this

goal have consisted of studying film properties as functions of plasma power, gas flow, gas pressure, reactant concentrations, etc. [1.12,1.13]. It should be noted that the effect of the frequency of the electro-magnetic excitation of the plasma on the film properties is virtually unknown. Very little information is available in the literature about PECVD systems operating in the 50 MHz to microwave range. Consequently, one of the motivations for this study has been to fabricate and characterize thin amorphous films deposited at a plasma excitation frequency in the frequency range: specifically at 2.45 GHz [1.14]. This work is described in Chapter 3.

With the advent of many new applications for  $a-Si:H$  based systems, there has been rejuvenated interest in exploiting the advantages associated with alternative fabrication techniques. To this end, part of this work was devoted to developing an alternative method of  $a-Si:H$  deposition, including the fabrication and characterization of thin films prepared by Activated Reactive Evaporation (ARE) [1.15,1.16]. Chapter 4 describes the results of this research.

### 1.3. Characterization Techniques

This section provides an overview of the most common characterization techniques used in this thesis. These methods provide information about composition, morphology, optical properties and electronic properties of thin films. Several techniques are also available for studying plasma properties which can then be related to the film properties.

In determining morphology, scanning electron microscopy and X-ray diffraction techniques are employed. Composition information is obtained from IR spectroscopy and energy dispersive X-ray analysis. Optical properties are obtained via visible and near IR spectroscopy and corroborated by spectrally resolved ellipsometry [1.17]. Electrical properties are primarily derived from the temperature dependence of dark-conductivity ( $\sigma_d$ ) and spectrally resolved photo-conductivity measurements. The electrical properties are perhaps the most sensitive parameters monitored and provide an excellent benchmark for producing optimal thin films.

Many more sophisticated techniques are currently employed in other laboratories, but those listed above are the most common. For example, photoluminescence, SIMS and Auger analysis, as well as ESR and photoemission spectroscopy have all been reported in the literature. For preliminary system

development and film characterization the techniques employed here are usually sufficient.

#### **1.4. Applications of Amorphous Semiconductors**

The primary motivating force behind the development of the  $a-Si:H$  technology has been the quest for photovoltaic power. Solar cell efficiencies have been reported at greater than 10% [1.18,1.19], a considerable triumph considering that just over a decade ago there was controversy regarding the possibility of doping  $a-Si$ . Following the development of  $a-Si:H$  for photovoltaic devices came a host of other applications.

Several applications of  $a-Si:H$  are in the area of xerography, vidicon devices, field effect devices, CCD arrays, threshold switching, and archival storage. Part of this study included applying  $a-Si:H$  as a media for archival storage, for both optical and electron-beam interrogated systems, as described in Chapter 5. Another material extensively studied (Chapter 2) was nitrogenated  $a-Si:H$  as mentioned above, with applications in xerography and integrated circuits.

#### **1.5. Basic Device Physics**

There are several models currently employed to understand the basic amorphous material and device physics and to describe the experimentally-observed phenomena. This section includes a brief discussion of the amorphous state and then outlines several of the most common theories in the literature. Finally it outlines an area which we feel is relevant to amorphous materials, and will advance the conjecture that amorphous materials display fractal behavior.

Amorphous semiconductors are characterized by the repetition of one or more basic molecular units without the structure associated with an infinite periodic array. That is, amorphous materials lack long range order of constituent atoms, but they are not completely disordered on the atomic scale. There exists strong correlation and ordering up to third or fourth nearest-neighbours, with respect to bond angle and bond length. It is the short range order that provides the amorphous solid with much of its crystalline-like behavior. As a consequence of the lack of long range order, the most powerful theorem in the theory of crystalline solids, known as Bloch's theorem, is however no longer valid. This is because Bloch's theorem depends upon translational invariance

of the crystalline unit cell.

Most amorphous systems are a combination of fully coordinated and defective amorphous states. Defective amorphous states, eg. unsaturated dangling bonds, combined with nearest-neighbour bond length and bond angle fluctuations give rise to strong electronic scattering and short coherence length of one-electron wave functions. Under these conditions many argue that the momentum selection rules break down, creating one of the most important differences between the amorphous and crystalline states. Furthermore, the preservation of short range order is argued to be responsible for an 'energy gap' and band edges. Near the band edges, fluctuations in the atomic configuration give rise to fluctuations in the potential experienced by an electron. These fluctuations are responsible for band-tail localized states. Transitions between localized states are allowed only to the extent that there is spatial overlap of the localized wave functions. Point defects within the material such as dangling, or unsatisfied, silicon bonds are expected to also yield a high density of defect states within the gap.

The first general theory or model to be discussed is attributed to N.F. Mott and E.A. Davis [1.20], although significant contributions are often credited to Cohen, Fritzsche and Ovshinsky [1.21]. The Davis-Mott model was largely based upon experimental observations. Optical absorption measurements suggested the existence of an energy gap  $E_{opt}$ ; which was interpreted to be a consequence of the short-range order. An observed temperature dependence of conductivity similar to that found in semiconductors, suggested that  $E_{opt}$  separated the extended states in the valence and conduction bands. Initial difficulties associated with doping or shifting the position of the Fermi level led Mott to postulate the existence of a finite density of states  $N(E)$  at the Fermi level  $E_F$ . This finite density of states at  $E_F$  was argued to result from defects in the atomic network. In view of the activated nature of the conductivity these states would have to be localized. Mott then derived an expression for conduction in localized states at the Fermi level, which has since become known as Mott's  $T^{-1/4}$  law. In the Davis-Mott model the lack of long-range order is claimed to be responsible for band-tail localized states. Conduction in the band-tail localized states is expected to contribute most strongly in the temperature range between conduction in extended states and conduction at  $E_F$ . Before leaving the Davis-Mott model, we point out that Mott predicted a mobility edge at the transition energy between the extended and localized states in

the bands.

The second model to be discussed here is attributed to M.H. Brodsky [1.22]. It is referred to as the quantum-well model; although originally based upon  $a-Si:H$ , it is speculated to be relevant to other amorphous semiconductor systems as well. As opposed to macroscopic models, the quantum-well representation is based upon a microscopic structural picture, and its band structure consequences. The assumption is that the potential disturbance about the  $Si-H$  bond is finite. Electrons or holes near band gap energies see different potentials near  $Si-H$  bonds than they do near  $Si-Si$  bonds. The result of this is that different regions of space have different band-gaps. There are regions containing only  $Si$  atoms bounded by barrier regions with larger band-gaps due to nearby  $Si-H$  bonds. The barrier heights would be somewhat less than what would be expected for head-on impact with  $Si-H$  bonds. The reduced barrier heights for a given  $Si$  region would be determined by the minimum of the saddle between peaks centered at the  $Si-H$  bonds. Electrons with energy less than this reduced barrier would be localized while electrons with energy greater than the reduced barrier would become delocalized. A similar argument holds for holes. The quantum well nature of the  $a-Si:H$  system is due to the bounded  $a-Si$  wells having quantized energy levels. The number and location of each energy level depends on the well's dimension, and a macroscopic average is claimed to yield a band of localized levels. Brodsky has indicated areas where the quantum well model has been correlated to several experimental observations, but also points out the need for further research. One such area of research would be the examination of spatially-coincident quantum wells.

The third and final model to be briefly discussed is the small polaron model attributed to Emin and Holstein [1.23]. Emin and Holstein argue that when the one-electron Hamiltonian is coupled with electron-phonon interaction and phonon Hamiltonians, a negative perturbation in the system Hamiltonian occurs when the electron is confined to a region on the order of the atomic spacing. The coupling between the compressed one-electron wavefunction and the phonon wavefunction combine to form a stable state, that is, a small polaron. The term polaron refers to the quasi-particle comprising the self-trapped electron and the associated atomic displacement pattern. The small polaron model is argued to be directly applicable to electrons directly above the mobility edge in amorphous semiconductors. Below the mobility edge, in

the localized state regime, the electron-phonon interaction and phonon Hamiltonians enhance and reinforce localization. Emin argues that the disorder associated with amorphism facilitates the formation of polarons, and that manifestations of polaronic formation should be made evident from transport experiments. The mobility of small-polarons is expected to be quite small, since self-trapped carriers can only move in response to alterations in the carrier-induced potential well which confines the carrier. Motion of the small-polaron in disordered systems is always by phonon-assisted hopping. At sufficient  $T$ , the electronic small-polaron hopping motion is activated with an activation energy. Emin points out several qualitative modrelations between experimental observations and the small-polaron model, but also notes that there remains much work to be done in understanding disordered systems. The small polaron model of Emin and Holstein has not yet been widely accepted by those working in the field of amorphous semiconductors.

An alternative perspective will be presented in Chapter 6 of this thesis based upon fractal geometry, and its relevance to the understanding of amorphous materials such as  $a-Si:H$ . Such a perspective has been very illuminating in recent studies of other disordered systems. Our argument is that there is enough experimental and theoretical evidence to warrant further study along these lines. One reason to suspect an underlying fractal-geometrical basis for the physics of amorphous semiconductors is the absence of translational invariance in these materials. Instead, there is in disorder nothing to preclude dilation invariance, and indeed there are many physical arguments in favor of such a 'symmetry'. Several experimental results also lead us to seriously consider the role of fractals. These results are the experimentally-determined conduction band density of states, which displays a linear energy dependence as opposed to the quadratic dependence commonly associated with three dimensional homogeneous solids, and the experimentally-observed dispersive transport. Another reason to suspect fractal behavior is due to the fabrication process itself, in that many natural growth mechanisms display stochastic fractal behavior. One can also consider the dependence of the fractal geometry upon the degree of incorporation of atomic  $H$  in an  $a-Si:H$  network. These ideas will be more fully presented in Chapter 6.

In summary, it is fairly clear that there is still a great deal of effort required to understand the basic physics of amorphous materials. It is among the goals of the thesis to contribute to this understanding both experimentally and

theoretically. The experimental results are intended to stand alone, and to directly contribute to the knowledge base of amorphous materials. The theoretical discussion of Chapter 6 is primarily intended to introduce many researchers working in the area of amorphous materials to an alternative representation, which we expect to provide at least complementary insight into the basis of their behavior. The following chapters describe the work which has been completed towards this goal.

## 1.6. References for Chapter 1

- [1.1] S.K. Bahl and S.M. Bhagat, *J. Non-Cryst. Solids*, 17, 409 (1975).
- [1.2] G.K. Wehner and G.S. Anderson, *Handbook of Thin Film Technology*, (Ed. L.T. Maissel, McGraw Hill, 1970).
- [1.3] M.H. Brodsky, R.S. Title, K. Weiser, and G.D. Pettit, *Phys. Rev. B*, 1, 2632 (1970).
- [1.4] E.C. Freeman and W. Paul, *Phys. Rev. B*, 18, 4288 (1978).
- [1.5] P.G. LeComber, A. Madan, and W.E. Spear, *J. Non-Cryst. Solids*, 11, 219 (1972).
- [1.6] N. Szydlo, N. Chartier, N. Proust, J. Maginarino, and D. Kaplan, *Appl. Phys. Lett.*, 40, 988 (1982).
- [1.7] B. Drevillon, J. Huc, A. Lloret, J. Perrin, G. deRosney, and J.P.M. Schmitt, *Appl. Phys. Lett.*, 37, 646 (1980).
- [1.8] S.R. Mejjia, M.Sc. Thesis, Dept. of Elec. Eng., U. of Manitoba (1983).
- [1.9] R. Grigorovici, *Mater. Res. Bull.*, 3, 13 (1968).
- [1.10] L. Kubler, J.J. Koulmann, R. Haug and A. Jaegle, *Solid State Comm.*, 48, 61 (1983).
- [1.11] B.A. Scott, R.M. Plecenik, and E.E. Simonyi, *Appl. Phys. Lett.*, 39, 73 (1981).
- [1.12] P. Kocian, *J. Non-Cryst. Solids*, 35&36, 195 (1980).
- [1.13] T.D. Moustakas, D.A. Anderson, and W. Paul, *Solid State Comm.*, 23, 155 (1977).
- [1.14] S.R. Mejjia, R.D. McLeod, K.C. Kao and H.C. Card, *Proc. 10th. Int. Conf. on Amorphous and Liquid Semiconductors, Tokyo, Aug.22-26*, 727 (1983).
- [1.15] A.C. Raguram and R.F. Bunshah, *J. Vac. Sci. Technol.*, 9, 1389 (1972).
- [1.16] R.F. Bunshah and A.C. Raguram, *J. Vac. Sci. Technol.*, 9, 1385 (1972).
- [1.17] H. Adashi and K.C. Kao, *J. Appl. Phys.*, 51, 6326 (1981).
- [1.18] Y. Kuwano, M. Ohnishi, N. Nishiwaki, S. Tsuda, T. Fukatsu, K. Enomoto, Y. Nakashima, and T. Tarui, *17th IEEE Photo-Voltaic Spec. Conf., Sept.27-30, San Diego*, 1338 (1982).

- [1.19] A. Catalino, R.V. D'Aiello, J. Dresner, B. Faughnan, A. Firester, J. Kane, H. Schade, Z.E. Smith, G. Swartz, and A. Triano, *ibid.*, 1421 (1982).
- [1.20] N.F. Mott and E.A. Davis, *Electronic Processes in Non-Crystalline Materials*, (2nd. ed., Clarendon Press, Oxford, 1979).
- [1.21] M.H. Cohen, H. Fritzche, and S.R. Ovshinsky, *Phys. Rev. Lett.*, 22, 1065 (1969).
- [1.22] M.H. Brodsky, *Solid State Comm.*, 36, 55 (1980).
- [1.23] D. Emin and T. Holstein, *Phys. Rev. Lett.*, 36, (1976).
- [1.24] K. Nakashima and K.C. Kao, *Thin Solid Films*, 41, L29 (1977).
- [1.25] P.W. Anderson, *Phys. Rev.*, 109, 1422 (1958).
- [1.26] A.M. Saperstein, *Am. J. Phys.*, 51, 1127 (1983).
- [1.27] B.B. Mandelbrot, *The Fractal Nature of Geometry*, (Freeman and Company, San Francisco, 1977).

## CHAPTER 2

### Undoped Amorphous $\text{SiN}_x$ Alloy Semiconductors \*

The work on nitrogenated  $a\text{-Si:H}$  was a collaboration between our laboratory and the Sendai group in Japan. The Sendai group prepared the films in an rf glow discharge, in which the nitrogen incorporation was facilitated by introducing various amounts of  $\text{N}_2$  into the gas mixture. Our laboratory was responsible for the optical and electrical characterization of the deposited films as well as their interpretation. The work was further subdivided between T.V. Herak, who was responsible for the optical characterization and the present author, who was responsible for the electrical and opto-electronic characterization. Specifically the electrical and optical properties of undoped  $a\text{-SiN}_x\text{:H}$  thin films were measured for  $0 \leq x \leq 0.6$ . It was observed that the activation energy for extended-state electron conduction as well as the optical gap were unaffected for  $\text{N}$  content  $x \leq 0.4$ . Based upon the temperature dependence of dark conductivity it may be argued that the product  $N_c \mu_n$  increased by a factor of 10 with  $\text{N}$  incorporation. It was found that a rapid conversion from a tetrahedral network to an  $a\text{-Si}_3\text{N}_4$  network occurred when  $x$  increased above  $\approx 0.4$ .

#### 2.1. Introductory Remarks

The purpose of this chapter is to describe the effects of the incorporation of nitrogen into amorphous hydrogenated silicon films on the energy distribution of electronic states, and the resultant influence on the carrier transport properties. The  $a\text{-SiN}_x\text{:H}$  films were prepared by rf glow-discharge in a  $\text{SiH}_4\text{-N}_2\text{-H}_2$  ambient. Several properties of this material including the composition ( $\text{N}$  and  $\text{H}$  content), the dependence of conductivity and photoconductivity upon doping with boron and phosphorus, and the correlation with fabrication conditions, have been presented earlier [2.1-2.4]. In this chapter, we investigate the behavior of undoped  $a\text{-SiN}_x\text{:H}$  films, by a detailed study of the temperature dependence of the dark conductivity and of the optical properties and their dependence upon nitrogen content.

\*The contents of this chapter are adapted from the Journal Non-Crystalline Solids, vol. 69, pp 39-48, 1984.

Other workers have reported on various properties of  $a-SiN_x:H$  prepared by alternative methods, including sputtering in an  $Ar-H_2-N_2$  ambient, glow-discharge in  $SiH_4-NH_3-H_2$ , chemical vapor deposition [2.5-2.11], and most recently by microwave glow discharge [2.12].

## 2.2. Experimental Methods and Characterization

The details of the fabrication process, the corroboration of the amorphous structure and the dependence of the film composition upon fabrication parameters have been explained previously [2.1-2.4]. The degree of nitrogen incorporation into the material has been determined both by infrared absorption and Auger analysis [2.2]. For the samples discussed in this chapter, the substrates were glass, the substrate temperature during deposition was  $250^\circ C$ , the chamber pressure was 1-2.5 torr, and the rf power density was  $0.1 Wcm^{-2}$ . Film thicknesses were in the range from 0.8 to  $1.5 \mu m$ .

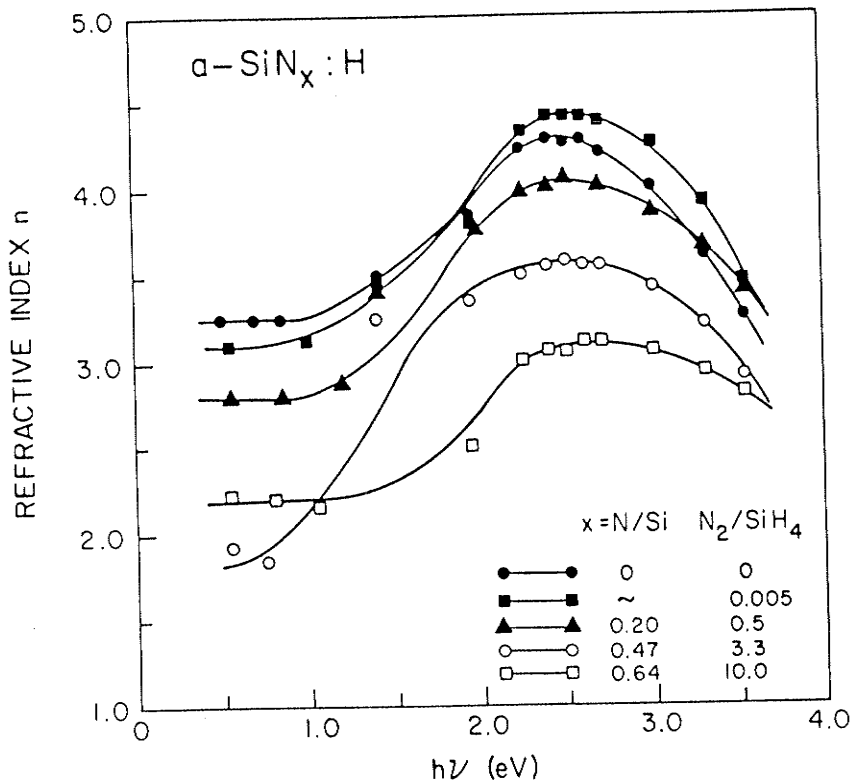


Figure 2.1: Refractive index vs. photon energy for undoped  $a-SiN_x:H$  films, with composition  $x$  (N/Si ratio) as a parameter. ( $0 \leq x \leq 0.64$ )

In the present work, we have determined the spectral dependence of the refractive index ( $n$  and  $k$ ) using spectrally-resolved ellipsometry by a method

described earlier for other amorphous thin films [2.13,2.14]. Our experience to date has been that ellipsometric data have yielded results for optical absorption which are 5-10% greater than other techniques. In view of the fact that the general trend of  $N$  in a  $-SiN_x:H$  was being sought, this presented no real difficulty, in that the trends would still be present in spite of the absolute error. From the extinction coefficient  $k$ , one may deduce the optical absorption coefficient  $\alpha$  by the relation

$$\alpha = 4\pi \frac{k}{\lambda} \quad (2.1)$$

The dependence of  $n$  and  $\alpha$  upon photon energy is shown in Figs. 2.1 and 2.2 where the  $N_2/SiH_4$  mole fraction in the gas phase was the experimental parameter. The  $N/Si$  ratio in the films has been determined earlier [2.2] and for convenience the conversion to  $N/Si$  has been made in Figs. 2.1 and 2.2. It should also be noted that as the  $N_2/SiH_4$  mole fraction increases from 0 to 10, the hydrogen content decreases from approximately 14% to 8% [2.1], although there was substantial scatter in the data.

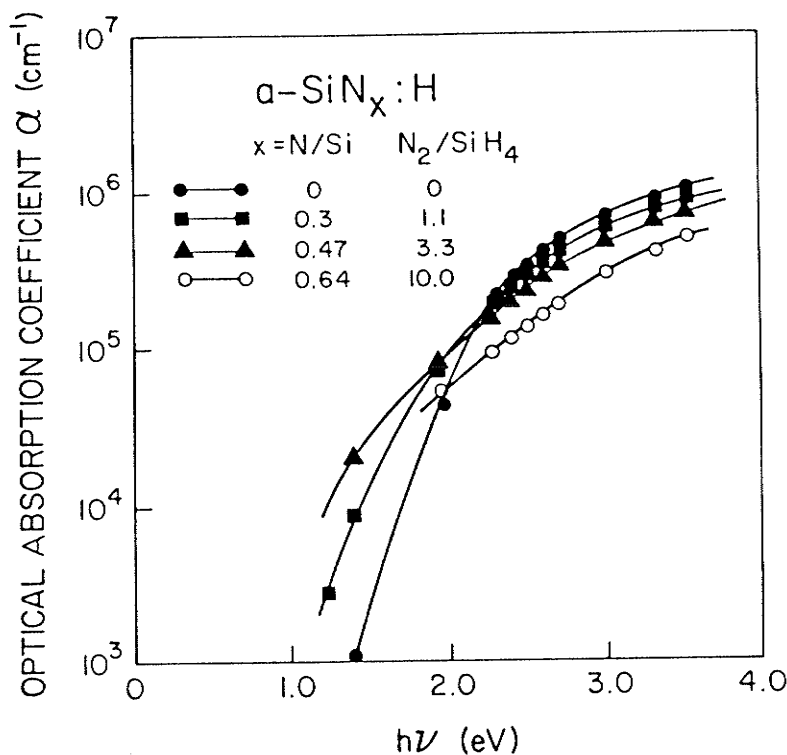


Figure 2.2: Optical absorption coefficient vs. photon energy for undoped  $a-SiN_x:H$  films with nitrogen content  $x$  as a parameter. ( $0 \leq x \leq 0.64$ )

The dark conductivity, with its dependence on nitrogen content and temperature, is shown in Fig. 2.3. The conductivity exhibited linear (ohmic) behavior for applied electric fields  $\leq 5 \times 10^3 \text{Vcm}^{-1}$ . Measurements employed gap-type surface electrodes with 1.5 mm spacing; currents were obtained under steady-state conditions using a Keithley 602 electrometer.

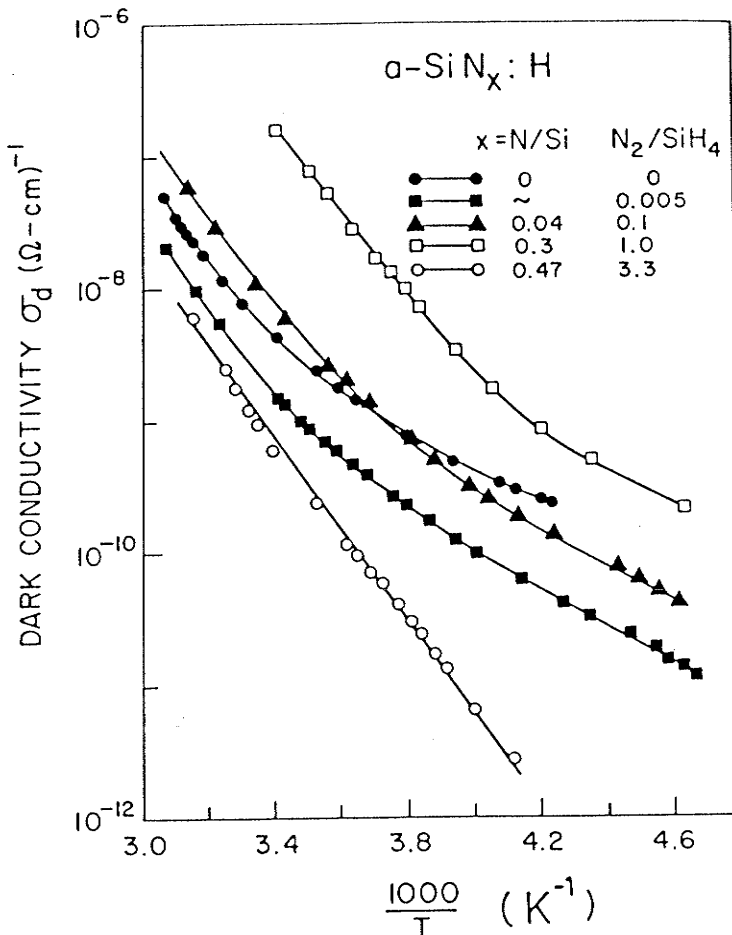


Figure 2.3: Dark conductivity vs. temperature for undoped  $a\text{-SiN}_x\text{:H}$  films, with composition  $x$  as a parameter.

### 2.3. Discussion of Optical Measurements

From the spectrally-resolved ellipsometry measurements and spectrophotometry results, we have inferred the value of the optical energy gap  $E_{opt}$ , by assuming parabolic bands for the extended states [2.15]. Although this assumption may not be entirely accurate (see chap.6) it allows for the comparison of these films with the literature, where the assumption of parabolic bands in determining  $E_{opt}$  is widely used. The dependence of  $E_{opt}$  upon nitro-

gen content was found to be in close agreement with the earlier determination from absorption measurements [2.3], and is shown in Fig. 2.4. The principal observation from Fig. 2.4 is that  $E_{opt} \approx 1.6-1.7\text{eV}$  independent of nitrogen content below a threshold concentration of  $N/Si \approx 0.4$ , with a rapid increase in  $E_{opt}$  above this concentration. It may be argued that there is also an increase in  $E_{opt}$  as  $N$  is initially introduced to the network. In this case the  $N$  may be considered to be having a similar effect as the  $H$ , namely in relaxing the amorphous network.

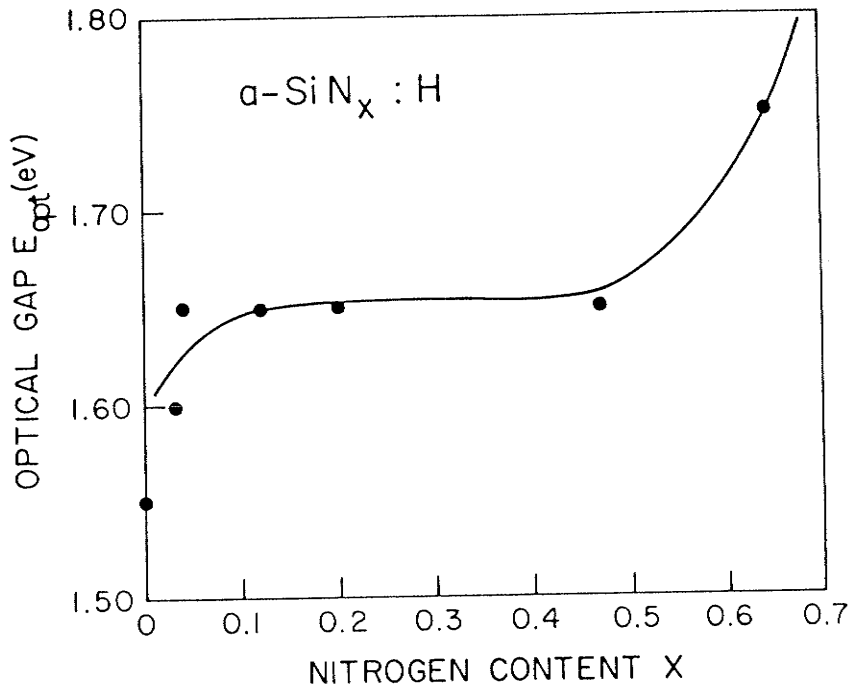


Figure 2.4: Optical energy gap of undoped  $\alpha\text{-SiN}_x\text{:H}$  films, with composition  $x$  as a parameter.

In addition, a plot of the refractive index  $n$  at photon energy  $h\nu=0.5\text{eV}$  is presented in Fig. 2.5. We observe that for nitrogen content well above that required for the increase in  $E_{opt}$  of Fig. 2.4,  $n$  approaches the value for amorphous silicon nitride  $\text{Si}_3\text{N}_4$  [2.16]. The interpretation of the conductivity data in the next section also leads to the conclusion that for the highest  $N_2/\text{SiH}_4$  ratios during fabrication, the film becomes  $\text{Si}_3\text{N}_4$ , which is an excellent insulator.

For parabolic bands, the optical absorption coefficient  $\alpha$  may be approximated by the well-known expression

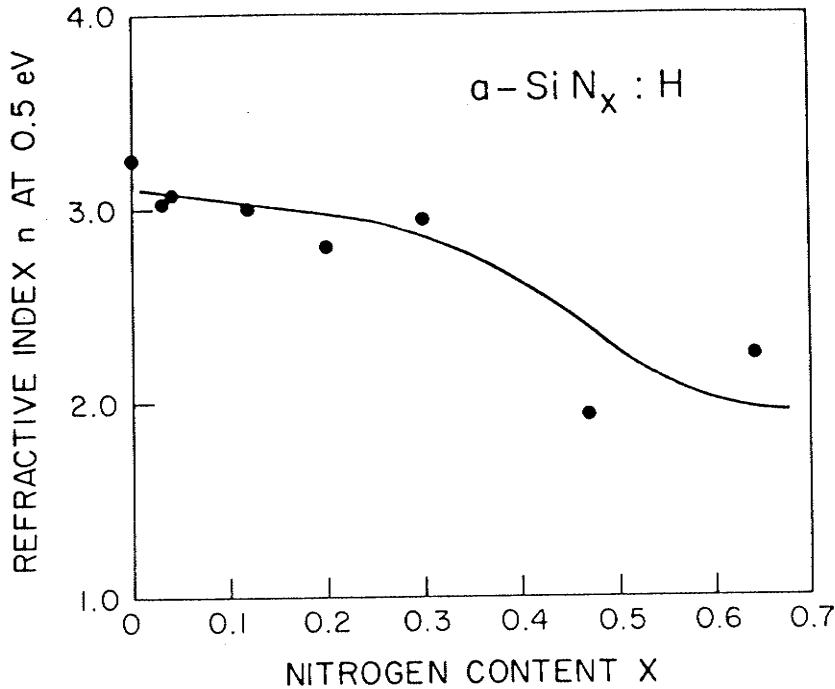


Figure 2.5: Refractive index at  $h\nu = 0.5 \text{ eV}$  of undoped  $\alpha\text{-SiN}_x\text{:H}$  films vs. composition  $x$ .

$$\alpha h\nu = B(h\nu - E_{opt})^2 \quad (2.2)$$

This is the expression employed above to obtain  $E_{opt}$  from measurements of  $\alpha$  vs.  $h\nu$ . In Equ.2.2, the parameter  $B$  is also a useful diagnostic of the material, since it is inversely proportional to the extent  $\Delta E$  of the tail states at the conduction and valence band edges. It has been shown [2.17] that

$$B \approx \pi^2 \sigma_o (n_1 c \Delta E)^{-1} \quad (2.3)$$

where  $\sigma_o$  is the minimum metallic conductivity,  $n_1$  is the refractive index, and  $c$  is the velocity of light.

The parameter  $B$  obtained from our optical data is shown in Fig. 2.6. These results indicate that the extent of the tail states in  $\alpha\text{-SiN}_x\text{:H}$  films increases with  $N$  content  $x$ .

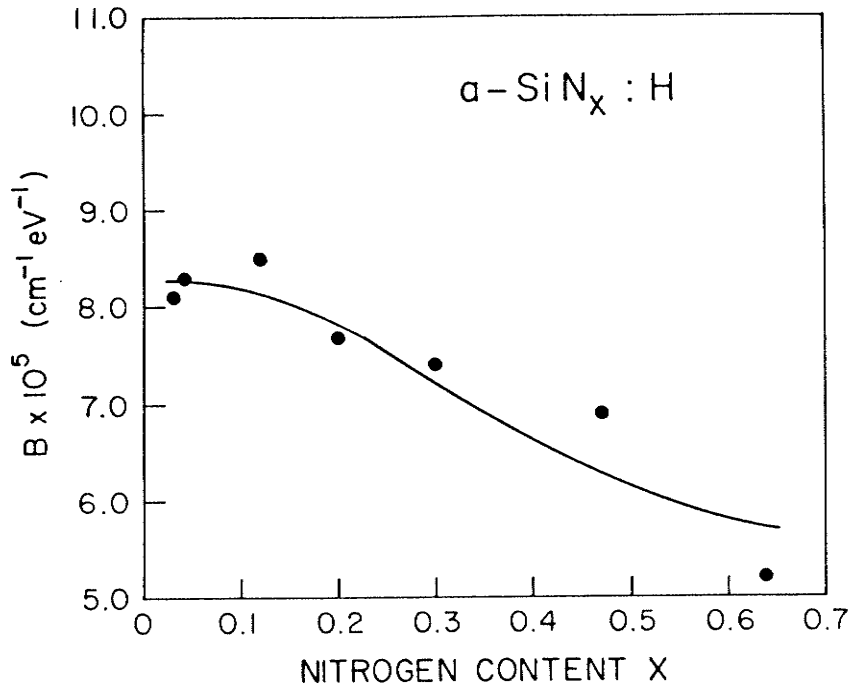


Figure 2.6: The  $B$ -parameter in  $\alpha h\nu = B(h\nu - E_{opt}^2)$  vs. nitrogen content  $x$  for  $a-SiN_x:H$  films.  $B \approx (\Delta E)^{-1}$  where  $\Delta E$  is the extent of the tail states.

#### 2.4. Discussion of Electrical Measurements

The temperature dependence of the dark conductivity (Fig. 2.3) may be understood on the basis of earlier treatments of  $a-Si:H$  thin films [2.18], with some modifications to take account of the effects of nitrogen incorporation. We describe the dark conductivity by

$$\sigma_d = \sigma_1 \exp\left(-\frac{E_1}{kT}\right) + \sigma_2 \exp\left(-\frac{E_2}{kT}\right) + \sigma_3 \exp\left(-\frac{C_3}{T^{1/4}}\right) \quad (2.4)$$

where the first term is due to conduction in extended states. This is known, on the basis of dependence on  $B$  and  $P$  doping, to be electron conduction in our undoped films [2.2]. Thus we have that

$$E_1 = E_c - E_f \quad (2.5)$$

where  $E_c$  defines the mobility edge in the conduction band of the  $a-SiN_x:H$  films and  $E_f$  is the energy of the Fermi level in darkness. Following Nagels [2.18], we have also that

$$\sigma_1 = e \mu_o N_c \exp\left(\frac{\gamma}{k}\right) \quad (2.6)$$

where  $\mu_o$  is the mobility in the extended states,  $N_c$  is their effective density (taken at  $E_c$ ),  $\gamma$  is obtained from the (linear) dependence of the energy gap upon temperature and  $k$  is Boltzmann's constant.

The second term in Equ.2.4 represents electron transport in the band tails below  $E_c$ , and the third term is due to variable-range hopping conduction at the Fermi level. The latter process may be further interpreted using the model of Mott [2.19] in which

$$C_3 \approx \left(18 \frac{\lambda^3}{kN(E_f)}\right)^{1/4} \quad (2.7)$$

where  $\lambda$  is the decay rate of the localized wave functions, and  $N(E_f)$  is the density of localized states at the Fermi level.

It is to be noted that  $\sigma_3$  in Equ.2.3 can also be expressed in an analytical form containing  $\lambda$  and  $N(E_f)$ , in which case it varies as  $(N(E_f)/T)^{1/2}$ . In general, however, this leads to unrealistic values for these quantities; several earlier workers attribute this to an uncertainty in the appropriate expression for  $\sigma_3$  [2.20,2.21]. Even with this uncertainty, however,  $\sigma_3$  is expected to increase approximately as  $N(E_f)^{1/2}$ .

Based on the dependence of  $\sigma_d$  upon  $T$  in the high-temperature range, we have found that  $E_c - E_f \approx 0.62-0.65\text{eV}$ , independent of nitrogen content, provided one does not exceed the threshold concentration  $N/Si \approx 0.4$  discussed above. It should be mentioned that until recently there was considerable controversy regarding the doping of  $a\text{-Si:H}$  by  $N$ . Several groups reported a decrease in the activation energy as  $N$  was incorporated; it was thought that  $N$  was being incorporated tetrahedrally, donating an electron to the lattice. More recently this has been discovered not to be the case, but rather that the  $N$  is incorporated trivalently, with the lone pair electrons remaining with the  $N$  atom. In Fig. 2.7 we show the dependence of  $\sigma_1$  upon nitrogen content.  $\sigma_1$  in Fig.2.7 increases by a factor of  $\approx 10$ , as the nitrogen content  $x$  increases from 0 to approximately 0.3, then decreases with further increases in  $x$ .

We may express  $\sigma_1$  by Equ.2.6. We are assuming that electron transport is dominant over hole transport for the undoped material, an assumption which

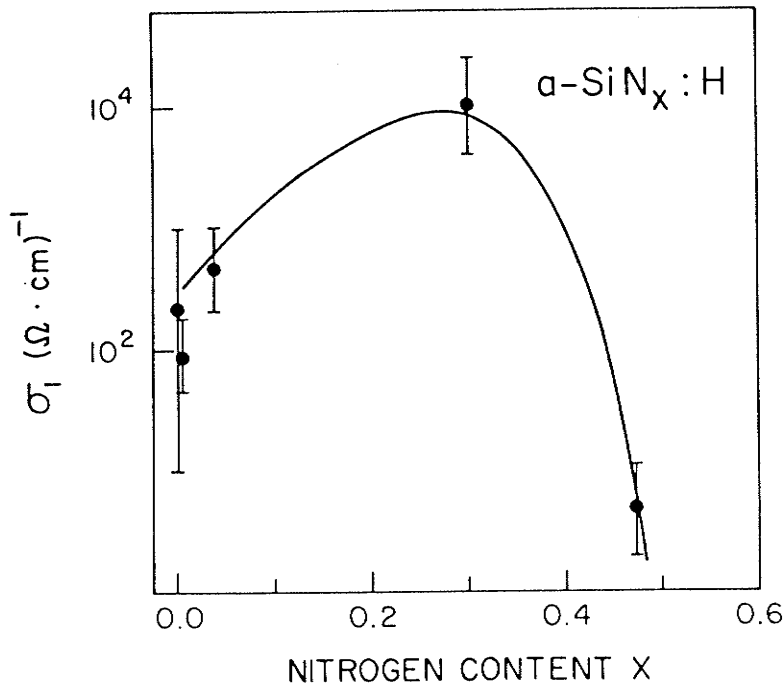


Figure 2.7: Conductivity parameter  $\sigma_1$  for extended-state conduction as in the first term of Equ.2.3, determined from experiment at high temperature, assuming  $\sigma_d \approx \sigma_1 \exp(-E_1/kT)$ .

has been verified for the same material by introducing dopants [2.2]. If we further assume that  $N_c$  is not greatly affected by the nitrogen content  $x$  for the small values of  $x$  during which  $\sigma_1$  increases, we may interpret Fig. 2.7 as an increased mobility by the same factor of  $\approx 10$  due to the nitrogen incorporation. Several researchers have recently reported [2.12] that for microwave plasma preparation of  $a\text{-SiN}_x\text{:H}$  they found a two phase structure, namely  $a\text{-Si:H}$  and  $a\text{-Si}_3\text{N}_4$ . If this were the case for these films, and since transport in  $a\text{-Si}_3\text{N}_4$  is by holes with a high density of defects which effectively trap electrons, no noticeable increase in  $\sigma_1$ , should have been noticed. As such we are led to believe that the nitrogen in our case is incorporated uniformly at least initially with a more gradual transition to  $a\text{-Si}_3\text{N}_4$  as more nitrogen is added. This does not exclude the existence of a two phase structure in which  $a\text{-Si}_3\text{N}_4$  is formed in clusters, but indicates that this formation begins after a background of  $a\text{-SiN}_x\text{:H}$  has been established. Finally, the increase in  $\sigma_1$  is very much larger than any effects arising from an uncertainty in the activation energies  $E_1$ , as is evident from the high-temperature region in Fig. 2.3. Another question which should simultaneously be addressed is the

possible effect of any micro-crystallinity in a multiphase structure.

In the intermediate temperature range, we have attempted to obtain  $\sigma_2$  and  $E_2$  in Equ.2.4 from our experimental data. Once we remove the contributions from the first term in Equ.2.4, which represents extended-state conduction, the current which remains is well described by the  $\exp(-C_3/T^{1/4})$  dependence of the third term. In other words, the contributions from the second term in Equ.2.4, which represents band tail conduction, are too small to be resolved in our experiment. We therefore assume that the transport is either dominated by extended state conduction or by hopping at the Fermi level, depending upon T.

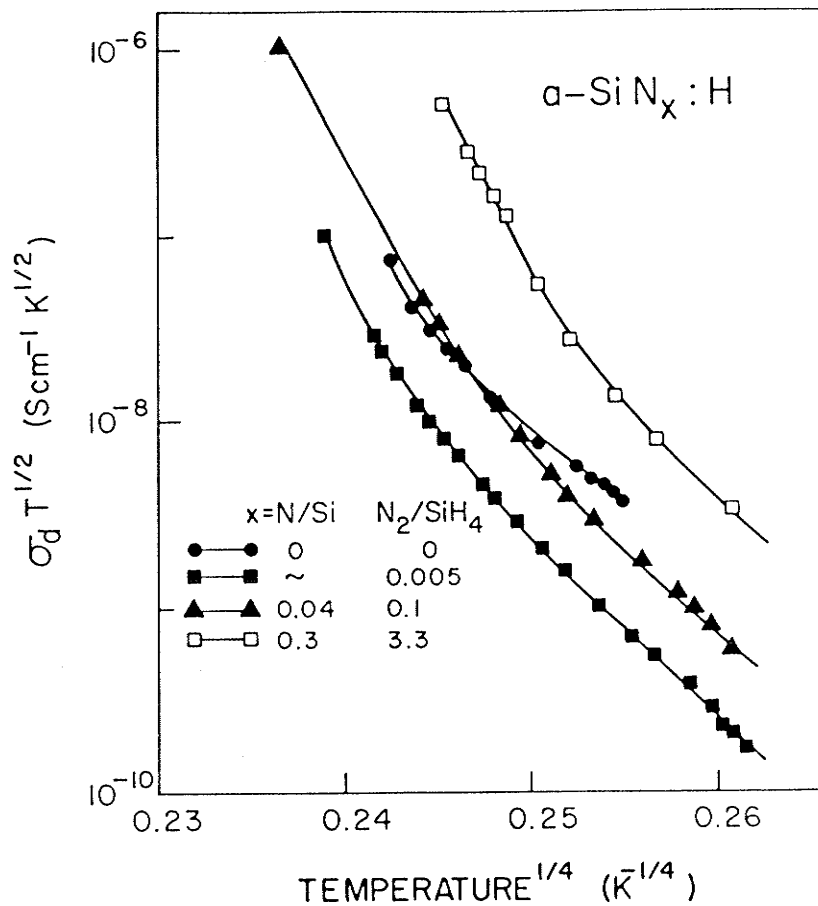


Figure 2.8: Conductivity in the low temperature region interpreted according to Mott's model of variable-range hopping at  $E_f$ . Plotted as  $\log(\sigma T^{1/2})$  vs.  $T^{-1/4}$  for comparison with theory.

Figure 2.8 shows the conductivity in the lowest temperature region, plotted to bring out the correspondence with the third term in Equ.2.3. Since there is

a  $T^{-1/2}$  dependence in  $\sigma_3$  [2.20] we expect a linear relation between  $\log(\sigma T^{1/2})$  and  $(T_o/T)^{1/4}$  in this region. On the basis of these results, and adopting a value for  $\lambda$  of  $10^{-7}$  cm (a 10Å radius for the localized wave functions), we obtain, using Equ.2.7, an estimate of the density of states at the Fermi level of  $N(E_f) \approx 1.1 \times 10^{17} \text{cm}^{-3} \text{eV}^{-1}$ . Furthermore  $N(E_f)$  appears to increase very modestly with N concentration if one considers  $\sigma_3$  to behave as  $N(E_f)^{1/2}$ . This is opposite to the case with boron-doped samples, where  $N(E_f)$  is obtained in the lower part of the energy gap [2.2]

There are a number of further observations which we have made on the  $a\text{-SiN}_x\text{:H}$  samples from this study:

- (1) The photoconductivity is only slightly dependent on the nitrogen concentration, attaining a maximum value of  $10^{-4} (\Omega \text{cm})^{-1}$  (at an optical intensity  $\approx 10^{16} \text{photons/cm}^2 \text{s}$ ) for  $N/\text{Si} \approx 0.2$ , for which case  $\sigma_{ph}/\sigma_d \approx 10^4$ . Further increases in  $\sigma_{ph}/\sigma_d$  to  $\approx 10^6$  can be obtained by the addition of small amounts of boron doping [2.2].
- (2) The spectral dependence of photoconductivity may be controlled to some extent by the nitrogen content.
- (3) The response (and decay) times for the photogenerated carriers, as determined by transient photoconductivity measurements, increases by approximately one order of magnitude, from 5 s to 50 s, as the wavelength increases from 600 to 900 nm. This is associated with photoexcitation into the shallow (band tail) states, but requires further study to fully understand the kinetics. The most important observation made during the transient photoconductivity was the non-exponential decay of the persistent photocurrent; this is consistent with the discussion of dispersive transport in Chapter 6.
- (4) Nitrogen incorporation also tends to reduce the Staebler-Wronski effect in  $a\text{-Si:N}_x\text{:H}$ .

Since the observations (1) and (2) are similar to results presented previously, [2.2] we do not enlarge on these results explicitly here.

## 2.5. Conclusions of Chapter 2

On the basis of the optical and electrical measurements of undoped amorphous  $SiN_x:H$  films presented in this chapter and the above discussion we may conclude that at least for films prepared by radio-frequency glow-discharge in a  $SiH_4-N_2-H_2$  ambient:

- (1) Nitrogen does not act as a donor impurity except for a very small  $N$  concentration region, since the activation energy for extended-state conduction is unchanged for  $0 \leq x \leq 0.4$ . The optical gap is also approximately constant in this range of  $x$ . It is believed that the nitrogen is being incorporated trivalently into the amorphous network and not tetrahedrally, at least for concentration  $x \leq 0.4$ .
- (2) The electron mobility for conduction in the extended states may be improved by nitrogen incorporation.
- (3) The density of states at the Fermi energy (in the upper part of the bandgap) is approximately independent of nitrogen content, at least for  $x \leq 0.3$ .
- (4) The ratio of photoconductivity to dark conductivity is improved by nitrogen incorporation but to a lesser extent than with both nitrogen and weak boron doping.
- (5) The extent of the tail states increases with the degree of nitrogen incorporation, but conduction in these states provides at most a minor contribution to the total current.
- (6) There is a precipitous conversion from the tetrahedral structure to  $Si_3N_4$  above  $x = 0.4$ . Below this nitrogen content we may regard the material as similar to a-Si:H with the differences outlined above.

## 2.6. References for Chapter 2

- [2.1] H. Watanabe, K. Katoh and M. Yasui, Japan J. Appl. Phys. 21, L341 (1982).
- [2.2] H. Watanabe, K. Katoh and M. Yasui, Thin Solid Films, 106, 263 (1983).
- [2.3] H. Watanabe, K. Katoh, M. Yasui, and Y. Shibata, *Proc. 10th Int. Conf. on Amorphous and Liquid Semiconductors*, Tokyo, Japan, Aug. 22-26, 1983; J. Non. Cryst. Solids, 59&60, 837 (1983).
- [2.4] H. Watanabe, K. Katoh and M. Yasui, Japan. J. Appl. Phys., 23(1), (1984).
- [2.5] J. Baixeras, D. Mencaraglia and P. Andro, Phil. Mag., 37, 403 (1978).
- [2.6] R.W. Griffith, F.J. Kampas, P.E. Vanier, and M.D. Hirsch, J. Non. Cryst. Solids, 35 & 36, 391 (1980).
- [2.7] W.Y. Xu, Z.L. Sun, Z.P. Wang, and D.L. Lee, J. de Physique, C4, supp. 10, 695 (1981).
- [2.8] S.M. Pietruszko, K.L. Narasimhan and S. Guha, Phil. Mag., 43, 357 (1981).
- [2.9] H. Kurata, M. Hirose and Y. Osaka, Japan J. Appl. Phys., 20, L811 (1981).
- [2.10] T. Noguchi, S. Usui, A. Sawada, Y. Kanoh and M. Kikuchi, Japan J. Appl. Phys., 21, L485 (1982).
- [2.11] G. Sasaki, M. Kondo, S. Fujita, and A. Sasaki, Japan J. Appl. Phys., 21, 1394 (1982).
- [2.12] A. Chayahara, M. Ueda, T. Hamasaki and Y. Osaka, Japan. J. Appl. Phys., 24, 19 (1984).
- [2.13] H. Adachi and K.C. Kao, J. Appl. Phys., 51, 6326 (1980).
- [2.14] K.C. Kao, R.D. Mcleod, C.H. Leung, H.C. Card, and H. Watanabe, J. Phys D: Appl. Phys., 16, 1801 (1983).
- [2.15] J. Tauc, in *The Optical Properties of Solids*, ed. F. Abeles, North-Holland: Amsterdam, p. 277 (1970).
- [2.16] S.M. Sze, *Physics of Semiconductor Devices*, (2nd Edition, Wiley: New York, p. 852, 1981).

- [2.17] E.A. Davis and N.F. Mott, *Phil. Mag.*, 22, 903 (1970).
- [2.18] P. Nagels, in *Amorphous Semiconductors*, ed. M. Brodsky, (Springer: New York, p. 123, 1979).
- [2.19] N.F. Mott, *Phil. Mag.*, 19, 835 (1969).
- [2.20] S.K. Bahl and S.M. Bhagat, *J. Non. Cryst. Solids*, 17, 409 (1975).
- [2.21] D.K. Paul and S.S. Mitra, *Phys. Rev. Lett.*, 31, 1000 (1973).

## CHAPTER 3

### Microwave Deposition of $a-Si:H$

The development of the microwave glow discharge system was motivated by the desire to explore alternative deposition systems and to exploit their inherent advantages. Towards this goal our laboratory developed several microwave sputtering and glow discharge systems. The development of the current system as well as film deposition and characterization was primarily the responsibility of S.R. Meija and the present author. A patent for the system is currently being sought. Chronologically, the development of microwave plasma processing in the Materials Laboratory at the University of Manitoba is roughly as follows. Initially a discharge tube was located in a rectangular to coaxial cavity transition. The system suffered severe limitations including sputtering of the discharge tube as well as requiring several hundred watts of microwave power to sustain the discharge. A second generation system was then developed which primarily consisted of an evacuated waveguide chamber where the plasma could be confined via a dc magnetic field. Preliminary results were presented at the 10th International Conference on Liquid and Amorphous Semiconductors. The waveguide chamber system has undergone an extensive development cycle and has evolved to include microwave plasma excitation under conditions of electron cyclotron resonance (ECR), as well as magnetic-confinement Reactive-Ion-Etching (RIE). The improved system and experimental results will be presented in Rome at the 11th International Conference of Liquid and Amorphous Semiconductors. Simultaneously journal publication is anticipated in the Review of Scientific Instruments.

Specifically, this chapter will present a discussion of the electrical and optical properties of  $a-Si:H$  thin films fabricated in a microwave glow discharge. The first section will describe the initial waveguide system and present the results from the 10th ICALS conference, while the second section will outline some system improvements and present some of the results which were obtained for the 11th ICALS meeting. In both cases the properties are dependent upon the substrate orientation with respect to the electric field, and upon the degree of magnetic confinement. The final section of this chapter will present conclusions based upon this work and indicate several areas where further research is required.

### 3.1. The Effect of Deposition Parameters on $a-Si:H$ Fabricated by Microwave Glow Discharge Techniques \*

The first section of this chapter focuses on some of our preliminary efforts in the development of a microwave plasma thin film deposition system.

#### 3.1.1. Introductory Remarks

Initial studies in our laboratory of microwave deposition systems were motivated by the desire to explore alternative methods for the fabrication of amorphous semiconducting materials. In particular the plasma physics and chemistry at microwave frequencies are expected to depart significantly from those at lower frequencies; in the former case the ionized species in the plasma are no longer able to follow the oscillations of the electric field. For example, the bombardment of the growing film by these ions will be reduced at microwave frequencies. Other differences are expected to arise as a consequence of the lifetime associated with an excited species in that, for the duration of excitation in an rf field, the electric field is approximately constant, whereas the lifetime is much longer than the period of the microwave excitation. Another difference which may be the more important is the electron temperature, in the case of rf plasma the electron temperature is approximately 1eV, whereas for microwave excitation the electron temperature is at least an order of magnitude greater. Previous studies of  $a-Si:H$  deposition from microwave plasmas have been troubled by incorporation of unwanted impurities, such as oxygen, into the films [3.1,3.2]. The techniques described in this chapter eliminate these difficulties, and further result in a very flexible system for controlling the properties of the semiconductor films.

#### 3.1.2. System Configurations

Two distinct microwave glow-discharge systems have been investigated for the deposition of  $a-Si:H$ . The first of these, shown in Fig.3.1, is the earliest system, which has the configuration of a coaxial line with the plasma acting as the center conductor. This system has been described in detail elsewhere [3.2,3.3]; it had an inherent limitation by virtue of the radial electric field which promotes sputtering of the quartz discharge tube and subsequent incorporation

The contents of this section have been presented at the 10th International Conference on Liquid and Amorphous Semiconductors, Japan (1983), and published in the J. Non-Cryst. Solids, vol.59-60, pp 727-730, 1983.

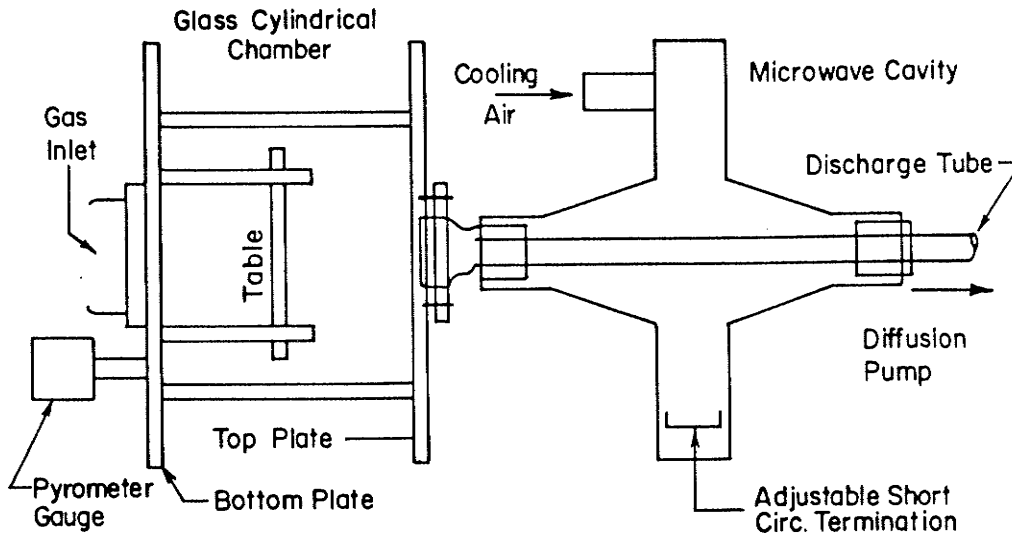


Figure 3.1: Configuration of the coaxial line-type microwave plasma system.

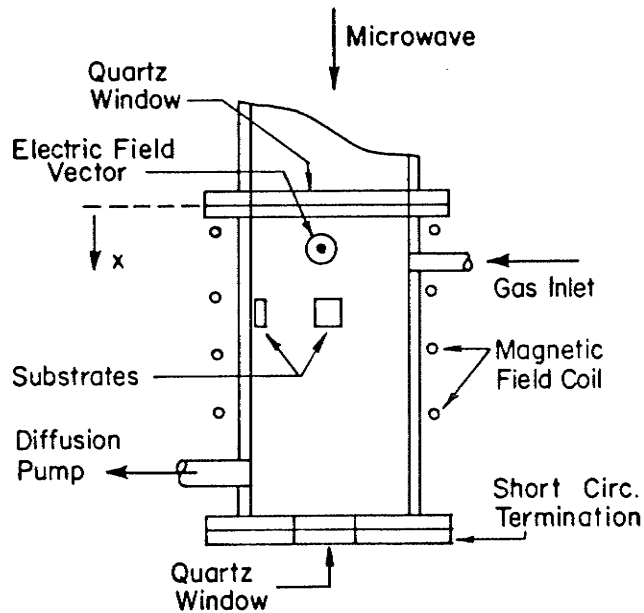


Figure 3.2: Configuration of the short-circuited waveguide chamber

of oxygen into the growing film [3.2-3.4]. In the second system, shown in Fig.3.2, deposition occurs inside a copper WR-284 waveguide in which the microwave plasma may be confined by an external dc magnetic field. This system operates at a microwave power on the order of 10W, which is an order

of magnitude lower than that required for the system of Fig.3.1. The system of Fig.3.2 also allows the substrates to be placed with their surfaces either parallel or normal to the direction of the electric field in the waveguide operating in the  $TE_{10}$  mode.

### 3.1.3. Experimental Conditions

For the results presented in the first section of this chapter, the following deposition conditions were employed: gas composition 10 %  $SiH_4$ , 45 %  $H_2$ , 45%  $Ar$ , total flow rate 30 sccm, microwave power 45W, gas pressure 0.1 torr, substrate temperature  $200^\circ C$ . An axial dc magnetic field was applied to the waveguide by means of an external coaxial coil; the coil current  $I_c$  was varied over the range 0-22A, which resulted in magnetic field profiles as shown in Fig.3.3. This magnetic field determined the profile of the deposition rate along the waveguide as shown in Fig.3.4. The symbols V and H in Fig.3.4 refer to the orientation of the substrates as vertical or horizontal in the waveguide chamber; the electric field is therefore parallel (V) and perpendicular (H) to the surface of the substrates in the two cases.

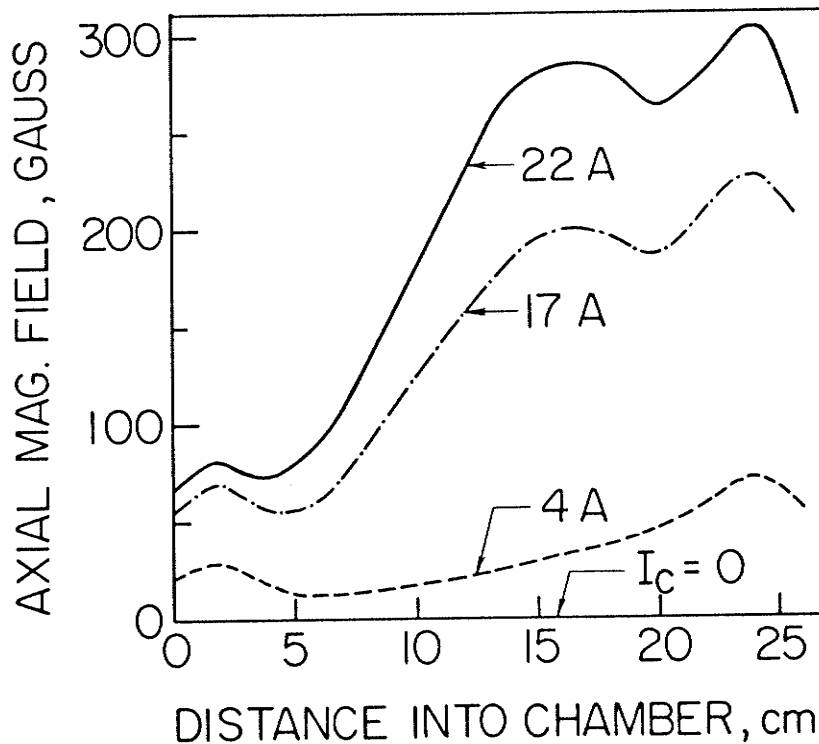


Figure 3.3: Variation of the magnetic field profile along the axis of the waveguide chamber with coil current  $I_c$ .

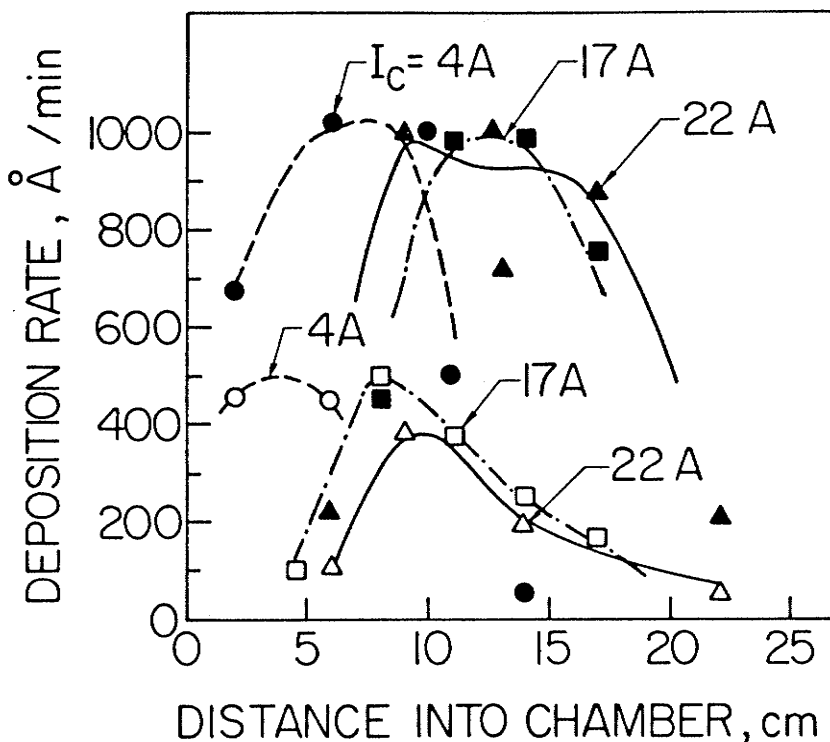


Figure 3.4: Variation of the deposition rate profile along the axis of the chamber with coil current  $I_c$ . Horizontal orientation: solid tokens.

Optical emission spectroscopy of the plasma was conducted during the deposition of the films. The composition of the plasma (intensity of  $[SiH]$  band  $[H_\alpha], [Ar]$  lines) was monitored, as well as impurities such as  $Cu$  or  $O_2$ ; these impurities were not observed for the operating conditions employed, although at the time the instrumentation resolution was poor. X-ray microanalysis of the samples similarly revealed no observable impurities, again limited to detectable amounts of approximately 1at%, with atomic mass greater than fluorine.

### 3.1.4. Film Characterization

Scanning electron microscopy, X-ray diffraction, IR and visible spectrophotometry, conductivity and photoconductivity were used to characterize the deposited films. Samples mounted horizontally (H) consistently exhibited a columnar growth structure, whereas no columnar structure was observed for vertically (V) mounted samples. All films were amorphous. The optical gap  $E_{opt}$  was consistently larger (by  $\approx 0.05eV$ ) for the V samples than for H samples; the same trend was observed for the B value ( $B = \text{gradient of } (\alpha h \nu)^{1/2}$ )

vs  $h\nu$  above  $E_{opt}$ ). Typical values for  $E_{opt}$  and  $B$  were 1.7 eV and  $4 \times 10^5 \text{ cm}^{-1} \text{ eV}^{-1}$ , respectively. As the V samples were consistently thinner than the H samples, the difference in the optical gap data may be a consequence of the thickness dependence of the optical gap.

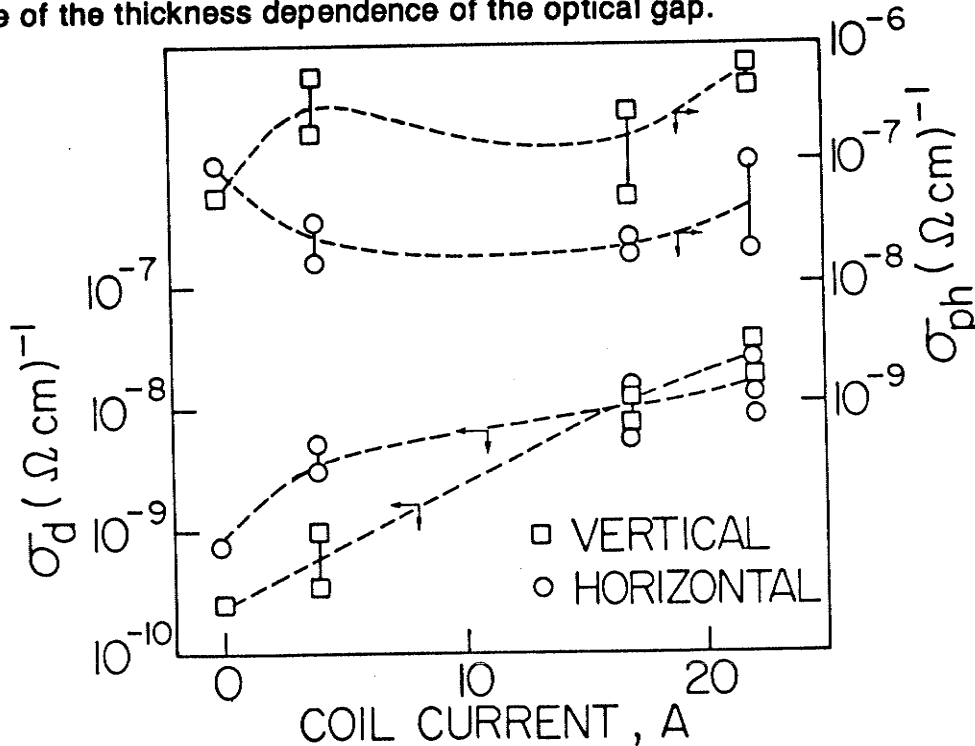


Figure 3.5: Dark conductivity and photo-conductivity of  $a\text{-Si:H}$  films grown in a microwave glow discharge as a function of magnetic field (coil current).

Figure 3.5 shows the typical dependence of the dark conductivity and the photoconductivity of the  $a\text{-Si:H}$  films upon the axial magnetic field (coil current), for both V and H samples.  $\sigma_{ph}/\sigma_d$  was larger for V than for H samples, in the best cases (not shown) attaining a value of more than  $10^3$ . Results from infrared spectrophotometry are shown in Fig.3.6. Pronounced absorption at  $2000$  and  $2090 \text{ cm}^{-1}$ , which we interpret as  $\text{SiH}$  and  $(\text{SiH}_2)_n$  stretch modes (since peaks at  $890$  and  $845 \text{ cm}^{-1}$  were also observed) [3.5], is enhanced by the magnetic field. We have also observed a higher degree of hydrogen incorporation in the H samples, which on the basis of our other observations we conclude is associated with the columnar structure. A rather spectacular SEM micrograph was fortuitously obtained clearly illustrating the columnar structure. This micrograph is reproduced in Fig.3.7; the tooth shaped object is an isolated column which broke away from the thin film.

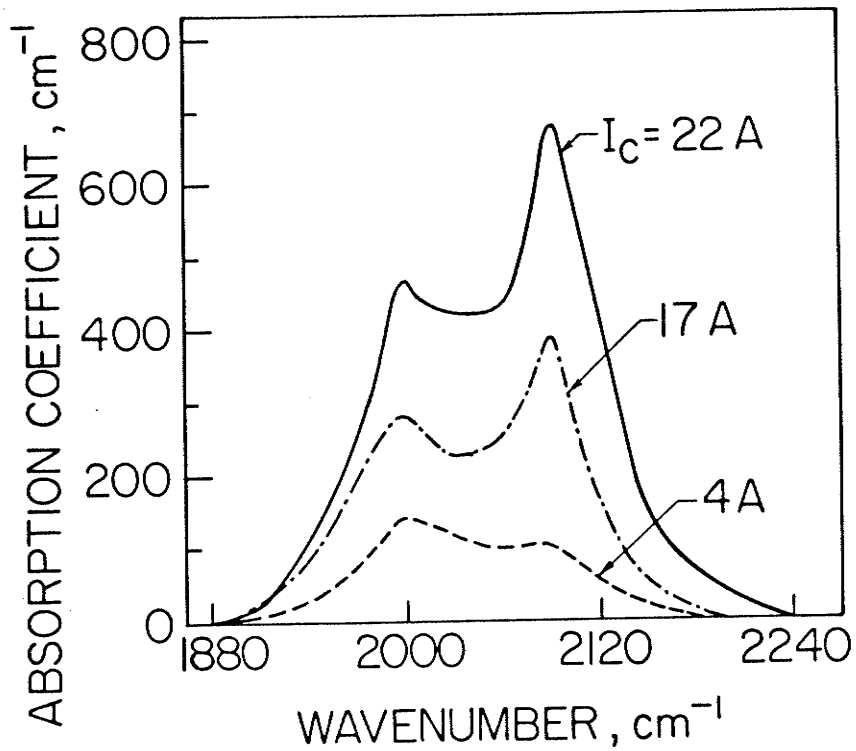


Figure 3.6: The effect of the magnetic field on the infrared absorption spectrum of a-Si:H grown in a microwave glow discharge.

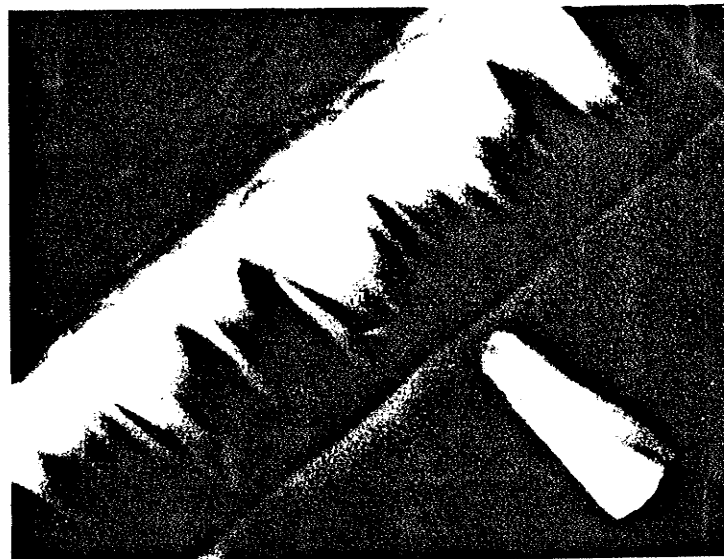


Figure 3.7: SEM micrograph illustrating the columnar structure of one of the H films.

Results of further studies on the films deposited in this system can be found in S. Mejia's M. Sc. thesis [3.6]. From the infrared absorption as well as the photoconductivity results, a significant percentage of oxygen was found to be present in the films, obviously contributing to the films' relatively poor electronic properties. In any event, this work has helped to provide a foundation for subsequent studies and has provided several directives. The next section describes details of the system improvements and presents preliminary results obtained from the new system.

### **3.2. Microwave Plasmas under Electron Cyclotron Resonance \***

Subsequent to the findings of the previous section, directions for system improvement became evident. Specifically, these improvements were required to obtain a more desirable magnetic field profile as well as to improve gas handling and vacuum facilities. The following section outlines some of the improvements, as well as some of the immediate results and ramifications. The present system has not only been found to be well-suited to the deposition of thin films, but also finds application in the area of magnetic confinement reactive ion etching (RIE). Advantages of the improved system are again anticipated to be derived from the departures of the usual plasma chemistry associated with conventional rf systems. This coupled with an improved gas handling network, vacuum system, and magnetic field profile should facilitate this effort. The modified microwave plasma reactor displays excellent plasma controllability over a wide range of operating conditions. The system configuration, optical emission spectroscopy of the plasma, as well as several thin film properties will be presented in this next section.

#### **3.2.1. Introductory Remarks**

As we have previously seen, one of the primary motivations for considering microwave plasmas is the fact that they are electrodeless. Traditionally microwave discharges have been produced by simply placing a discharge tube inside a waveguide or cavity, at locations of high electric fields [3.7]. Several

---

The results of this section will be presented at the 11th International Conference on Liquid and Amorphous Semiconductors to be held in Rome, Sept., (1985).

extensions and modifications to these techniques have followed [3.3,3.8]. Much of the early difficulty was associated with sputtering of the discharge tubes and surrounding structures; this difficulty was associated with both microwave and rf systems. As we have seen, subsequent modifications to these systems included magnetic confinement of the plasma [3.9,3.10]. This has quite naturally led to systems which exploit conditions of electron cyclotron resonance (ECR).

This section describes an extension to the microwave plasma system, and demonstrates experimentally that microwave excitation of plasmas undergoing ECR due to an external dc magnetic field, presents a viable alternative to rf plasma processing. In particular, this system presents alternatives for the fabrication of amorphous semiconductors as well as for dry etching. In addition, studying microwave excited plasmas may also help to determine the effect of frequency and the distribution of electron energies on plasma chemistry in general.

### 3.2.2. System Configuration

The microwave plasma system primarily consists of a short circuited or matched stainless steel waveguide chamber constructed in our workshop (dimensions equivalent to WR-284), in which the plasma may be confined by an externally applied dc magnetic field, as shown in Fig.3.8. Under ECR conditions the power requirements are typically on the order of 1W. A maximum in the absorbed power is observed when the magnetic field is approximately 15-17 A, the coil current required to obtain ECR conditions.

The primary mode of operation for the waveguide is again the  $TE_{10}$  at a frequency of 2.45 GHz. The modified system includes gas lines which are bakable and provides a base pressure of  $10^{-6}$  torr, with diffusion pumping. A cold trap is also used to freeze out impurities due in part to backstreaming of gas from the rotary pump. The evacuated chamber is 45cm in length with several ports for plasma analysis. As opposed to the earlier system, two external coils are mounted coaxially to the waveguide chamber providing a mirror-like magnetic field along the axis of the waveguide as shown in Fig.3.9. The mirror-like magnetic field employed confines the plasma in both the transverse and longitudinal directions of the chamber. This is accomplished by forcing electrons to travel in a spiral path around the axis of the chamber confining the electrons and thus the plasma to a region between the peaks as shown in

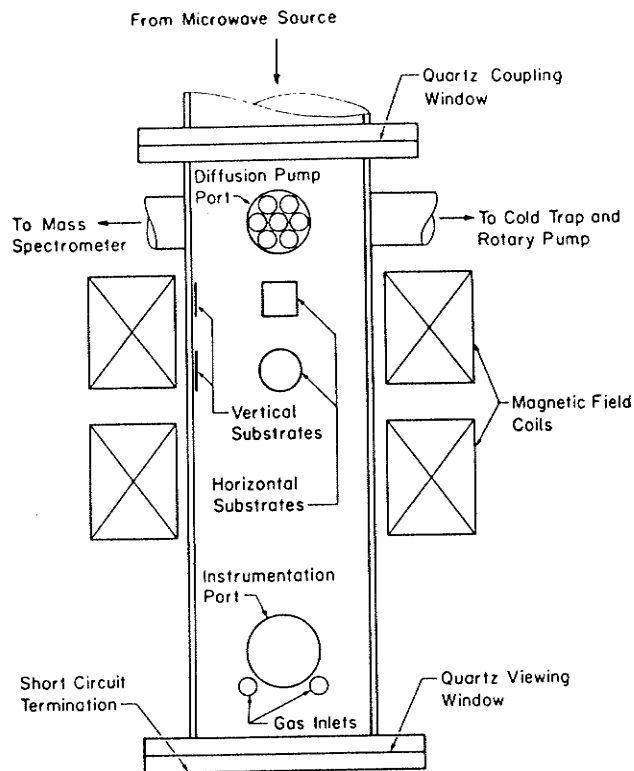


Figure 3.8: Modified short-circuited waveguide configuration.

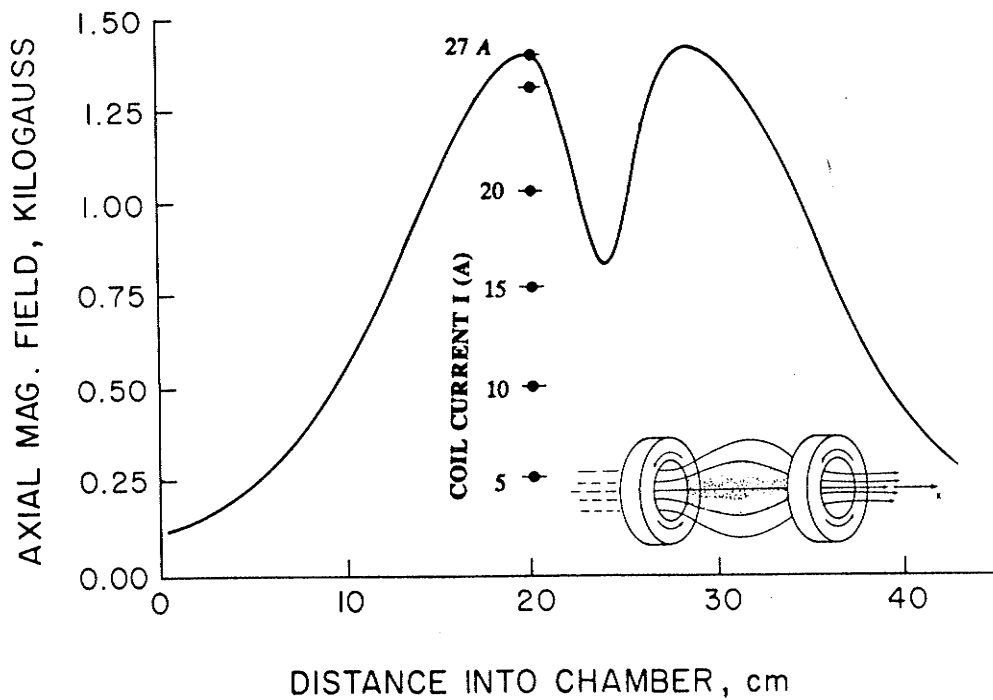


Figure 3.9: Variation of the magnetic field profile along the axis of the chamber as a function of coil current.

Fig.3.9.

The function of the coils is not only to provide magnetic confinement which reduces electron and ion bombardment, but also to allow for plasma excitation under conditions of ECR, which theoretically occurs at 875 Gauss at the microwave operating frequency of 2.45 GHz. The gyro radius for a proton in this system is on the order of  $1mm$ ; as such the plasma is well confined. The magnetic field profile is easily adjusted by varying the coil currents, coil separation, or by employing magnetic short circuits along the outside of the wave-guide. With these facilities the plasma may also be conveniently pulsed by modulating the coil current around 15 amps ( the critical coil current required to obtain ECR conditions). The present system also allows for substrate heating using either internal or external heaters; in either case, only local heating of the chamber is required. The overall system configuration is shown in Fig.3.10.

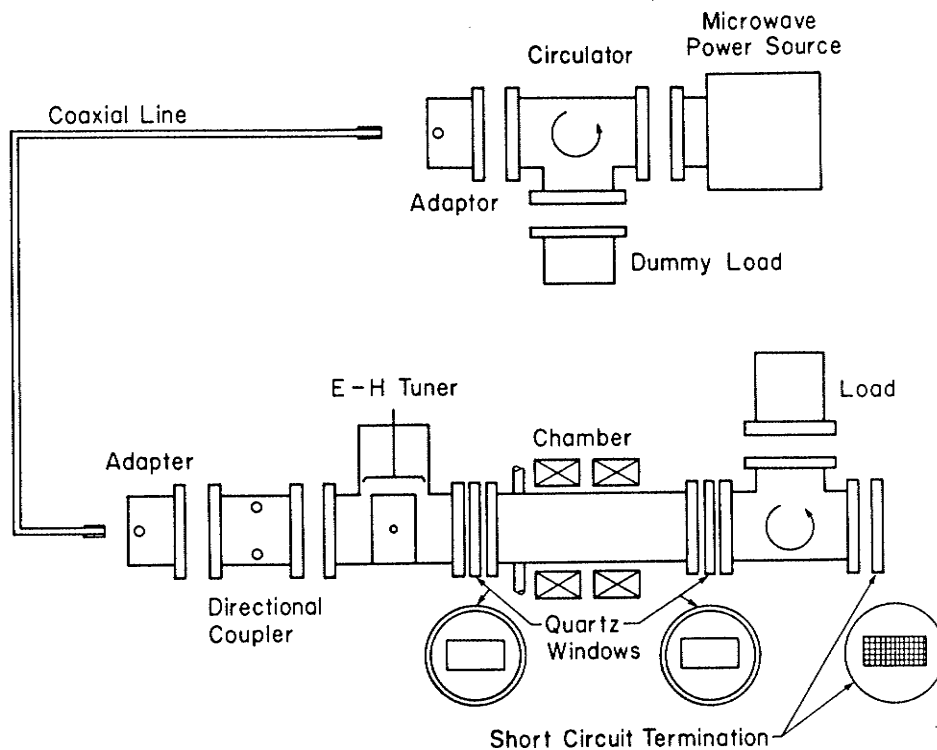


Figure 3.10: Overall system configuration.

### 3.2.3. Preliminary Experimental Results

The plasma conditions are monitored by real-time optical emission spectroscopy (OES) and electron mass spectroscopy. Preliminary plasma studies have utilized high purity argon, helium and hydrogen for comparison with results from large volume microwave plasmas [3.9]. The system is readily scaled-up for industrial applications; one alternative configuration is shown in Fig. 3.11. Subsequent studies have included the deposition of a-Si:H thin films from silane and hydrogen plasmas for comparison with films prepared by conventional rf plasmas.

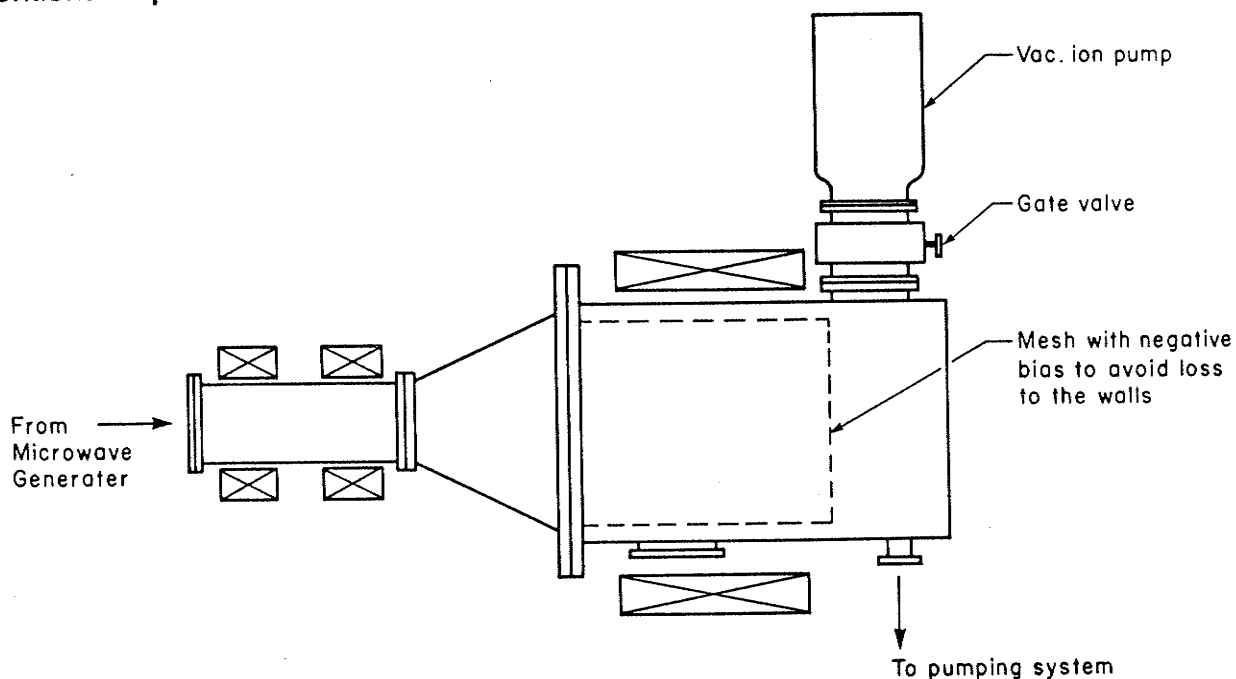


Figure 3.11: A scaled-up design for industrial applications.

Preliminary infrared spectroscopy results revealed primarily an  $SiH$  vibrational mode with only a small absorption due to the  $SiH_2$  mode. This is in contrast to the results presented in the previous section where an increase in the magnetic field below ECR conditions manifested itself in the proliferation of the  $(SiH_2)_n$  vibrational mode. Although direct comparison is inappropriate, this is an interesting and beneficial property of the modified microwave plasma reactor. The proliferation of the  $(SiH_2)$  mode in the earlier system may have been a result of  $Ar$  in the gas mixture. The initial system required the  $Ar$  to maintain a stable plasma.

Figure 3.12 illustrates the radiated emission intensity from  $[SiH]$  and  $[H_\alpha]$  lines versus magnetic field current. Prior to the OES experiments, the chamber was initially evacuated to a base pressure of  $< 10^{-6}$  torr after several hours of baking to remove any water vapor which may have been present. Argon was used to purge a cold trap several times prior to converting from a diffusion pump to a high throughput rotary pump. A gas mixture of 10%  $SiH_4$  in  $H_2$  was used for the investigation. During the experiment the chamber was held at a pressure of 0.13 torr, the flow was controlled by a needle valve and a high throughput valve throttled to maintain constant pressure. An absorbed microwave power on the order of 4W was used throughout, except for low magnetic field where the power was increased to approximately 10 W; the power required to sustain a plasma well below ECR. As can be seen from Fig.3.12 there is a strong dependence of the emission intensities upon the magnetic field confinement, although there is little variation in the ratio. This is invariance to some results obtained for similar studies when a magnetic field is employed to confine an rf plasma [3.11]. For example, the  $[H_\alpha]$  line was in general greater than the  $[SiH]$  line. This is in contrast to rf plasmas where the  $[SiH]$  line usually dominates, although it is the author's opinion that in many cases it is the  $[SiH]$  complexes that are often included in the calculation of the actual  $[SiH]$  line; thereby accounting for possible discrepancies. Below 15 A coil current (the condition which corresponds to ECR), a plasma could not be obtained unless the flow was reduced to the lowest level or the power increased. This non-resonant plasma also contained a rather large background of undetermined constituents, which may be attributed to backstreaming at the reduced flow rate. In all cases the emission intensity from  $[SiH]$  increased with increasing flow. The insert contains a typical OES spectrum illustrating the absence of detectable impurities. In particular, no detectable oxygen was found from the OES for these plasma conditions.

One will also note that the insert of Fig. 3.12 contains a large background, which resembles black-body radiation above the cutoff frequency of the quartz lenses used for the light collection. These spectrums have the background subtracted and as such do not represent black body radiation due to microwave heating, but rather a manifestation of the bremsstrahlung radiation. This provides a direct means of obtaining the electron energy distribution; typically the electron temperature was found to be 10eV. We have noticed a

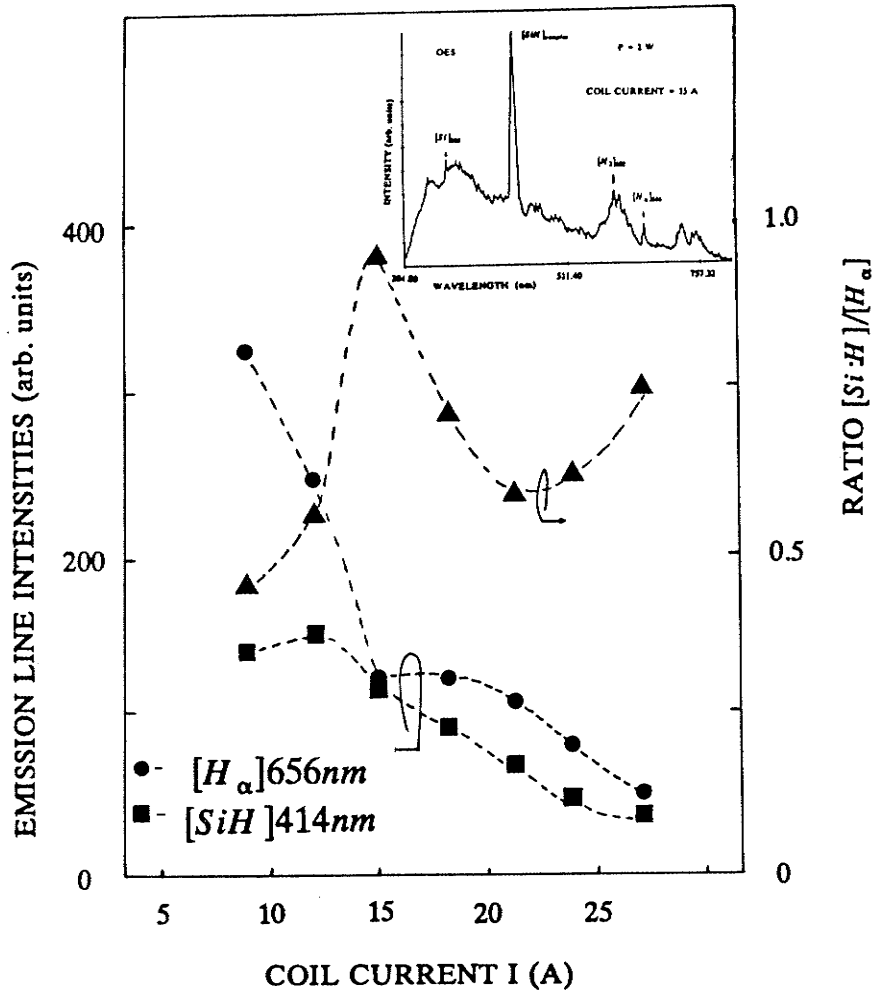


Figure 3.12: Dependence of the [SiH] and [H<sub>α</sub>] emission intensities upon magnetic field current for a 10% SiH<sub>4</sub> in H<sub>2</sub> gas mixture.

slight shift in the peak of this continuum toward higher energies as the magnetic field is increased beyond ECR. This shift indicates the presence of more energetic electrons and results in more emissions at higher energies, clearly illustrating one of the differences between microwave plasmas above ECR conditions and below ECR conditions. As we have previously indicated, the power requirements to sustain a stable plasma were found to be on the order of 1 W under ECR conditions, a reduction in the microwave power requirements by greater than 1 order of magnitude as compared to non-resonant plasmas discussed in the previous section. In addition to this Ar was not required to sustain or stabilize the plasma.

Figure 3.13 illustrates photographically the effect of further increases in the magnetic field confinement beyond ECR conditions. One additional feature

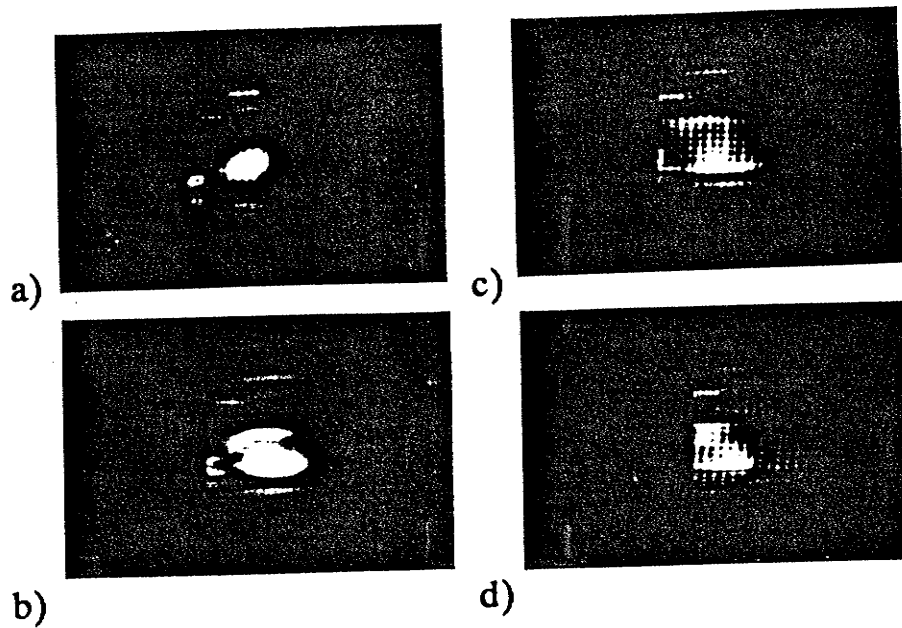


Figure 3.13: Photographic illustration of the effect of the magnetic field upon the confinement of the plasma. a)15 A coil current. b)17 A coil current. c)19 A coil current. d)21 A coil current.

to note is that the plasma mode could also be altered considerably as the plasma parameters were varied. Further investigation is required to determine the effect of the mode on the plasma chemistry. Although not shown it should be stressed that the plasma parameters are easily controllable, allowing for a wide variety of operating conditions. Thus a fine tuning of the microwave power and the magnetic field allows for a careful selection of concentrations of reactive species. This concept when applied to RIE is expected to produce a high selectivity required for etching by allowing for enhancement of the desired constituents with the concomitant suppression of the unwanted species

### 3.2.4. Film Characterization

As we have mentioned the work on thin film deposition was motivated by the desire to study alternative deposition techniques for the fabrication of amorphous semiconductors. It is anticipated that the present system may exhibit advantages arising from departures in the usual plasma chemistry corresponding to conventional rf systems. In particular, preliminary results indicate that the emission lines from  $[SiH]$  and  $[H_{\alpha}]$  vary monotonically as functions of applied field for plasmas confined beyond ECR conditions. It was found that when the microwave power was sufficiently increased ( beyond 20

W ) such that a non-resonant plasma could be sustained, the emission intensities displayed a resonance phenomena reaching a maximum intensity at ECR conditions. This has also been verified as the conditions corresponding to maximum power absorption.

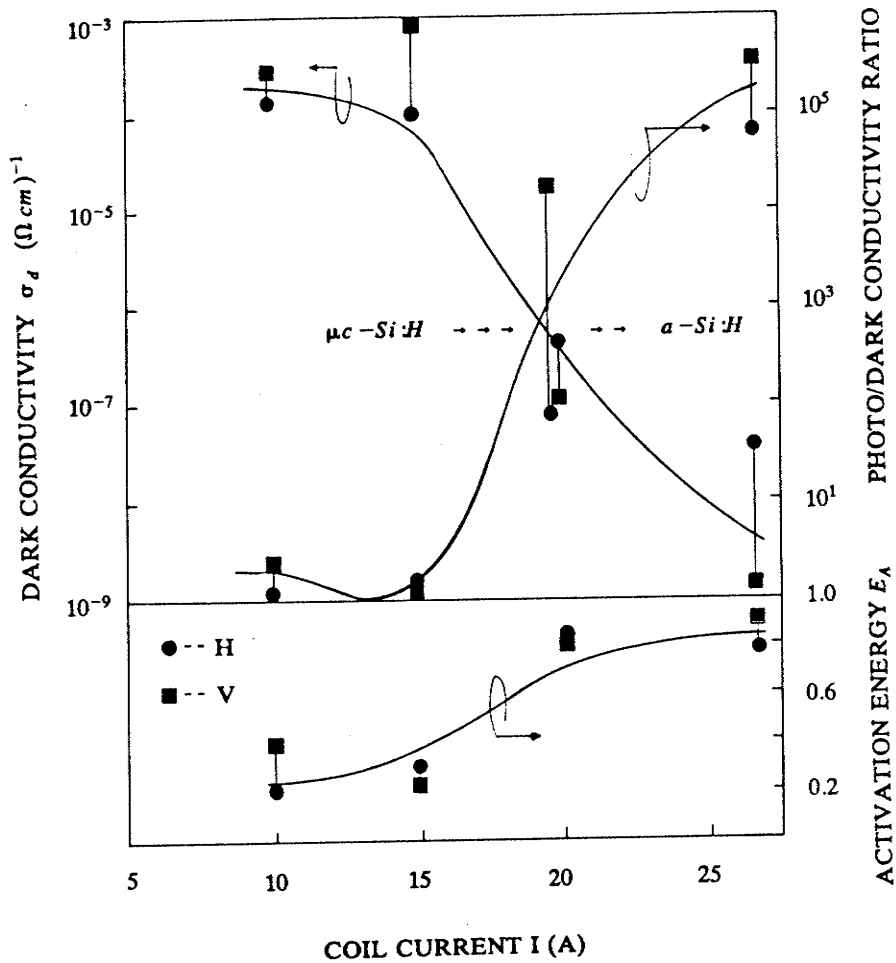


Figure 3.14: Electrical and optical properties of  $a\text{-Si:H}$  thin films as functions of magnetic confinement (coil current). Photon flux  $1 \times 10^{15} (\text{cm}^{-2} \text{s}^{-1})$  @ 6328 Å.

To further illustrate differences between microwave and rf plasmas, and illustrate the versatility of the microwave plasma system,  $a\text{-Si:H}$  samples were fabricated. The following conditions were employed: pressure 0.13 torr, substrate temperature  $150^\circ \text{C}$ , and minimum microwave power ( $\approx 1 \text{W}$ ). As we are most interested in the effect of the magnetic field, the coil current was the primary adjustable variable. Typical characterization parameters such as the dark-conductivity, photo-conductivity, activation energy and optical gap are

shown in Fig.3.14. Comparing the results of Fig.3.14 with the literature, little difference is apparent between our films, prepared by microwave glow discharge above ECR, and films prepared under similar conditions in a conventional rf reactor. On the other hand, when one considers the function of the magnetic confinement, significant variation in the film properties are found. X-ray data has revealed that the films undergo a microcrystalline to amorphous phase transition as the magnetic field is increased; this is corroborated by the functional dependence of  $\sigma_d$  and the activation energy. In spite of the microcrystalline structure at low magnetic field, IR absorption indicated a predominant *SiH* absorption line as opposed to microcrystalline films produced in rf reactors at substantially higher temperatures and powers. It has not escaped our attention that the appearance of the microcrystalline structure indicates that the system may be a most effective system for low temperature deposition of microcrystalline films for IC fabrication. Particularly now as the industry is expending considerable effort in new film deposition techniques and low temperature processing for VLSI, the microwave plasma system may present a viable alternative to some of the more traditional plasma processing systems. The present results indicate that it should be possible to fabricate microcrystalline films below 100°C. In addition to this, the microcrystalline to amorphous phase transition allows for a microcrystalline n-type layer to be deposited directly on an intrinsic *a-Si:H* layer in the same chamber by simply introducing a change in the magnetic field during deposition. This is obviously of practical importance for optoelectronic applications. The films did not display any oxygen incorporation and are considered 'clean'. These results are preliminary and as yet do not reflect optimal *a-Si:H* films (in the photovoltaic sense), but a wide range of film properties have been demonstrated. It is anticipated that with the ease of plasma controllability, the deposition conditions can be optimized to produce *a-Si:H* material of typical rf quality or better.

Also by exploiting the differences between conventional rf plasmas and microwave ECR plasmas problem instances may be encountered which are addressed more easily or directly by the microwave ECR system. One of the areas currently being investigated is the application of the microwave system to magnetic-confinement ion- and reactive-ion-etching. Presently Mitsubishi is working on a prototype etching system for 0.2 to 0.3  $\mu\text{m}$  VLSI design rules utilizing microwave ECR plasmas.

We have attempted to present a plasma system for excitation at microwave frequencies under conditions of electron cyclotron resonance. One of the main virtues of this system operating under ECR is reduction in microwave power over non-resonant systems. We have demonstrated the systems versatility for the deposition of thin films and indicated additional applications in dry etching.

### **3.3. Conclusions of Chapter 3**

The conclusions based upon the results of Chapter 3 are as follows:

1. Microwave plasma processing for the fabrication of  $a-Si:H$  thin films presents a viable alternative to conventional rf plasma deposition.
2. Absorbed microwave power is substantially reduced if ECR is exploited.
3. Variation of the magnetic field confinement manifests itself in a transition from a microcrystalline to amorphous structure for  $a-Si:H$  thin films prepared under the depositions described in this chapter.
4. The present microwave plasma system has applications in both thin film deposition and reactive ion etching.
5. Further studies are required to relate the effects of frequency as well as magnetic field confinement to the plasma chemistry.

### **Acknowledgements for Chapter 3**

We would like to thank the University of Manitoba Department of Chemistry for the use of their Nicolet FTIR spectrophotometer, and for their assistance in obtaining and analyzing the spectra.

### 3.4. References for Chapter 3

- [3.1] J.F. Currie, P. Depelsenaire, J.P. Huot, L. Paquin, M.R. Weitheimer, and A. Yelon, *Can. J. Phys.* 61, 582 (1983).
- [3.2] H.C. Card and K.C. Kao, *Thin Film Semiconductors for Photovoltaic Devices by Microwave Plasma Techniques*, Final Report for Contract Serial No. OSx81-00076 of the National Research Council of Canada, February 1983.
- [3.3] I. Kato, H.C. Card, K.C. Kao, S.R. Mejia and L. Chow, *Rev. Sci. Instru.*, 53 , 214 (1982).
- [3.4] F.K. Mctaggert, *Plasma Chemistry in Electrical Discharges* (Elsevier, Amsterdam, 1967).
- [3.5] G. Lucovsky, R.J. Nemanich, and J.C. Knights, *Phys. Rev. B.*, 19 , 2064 (1979).
- [3.6] S.R. Mejia, M.Sc. Thesis, University of Manitoba (1984)
- [3.7] M.A. Heald, C.B. Wharton, *Plasma diagnostics with microwaves*, (John Wiley & Sons Inc., New York, 1965).
- [3.8] J.F. Currie, P. Depelsenaire, J.P. Huot, L. Paquin, M.R. Weitheimer and A. Yelon, *Can. J. Phys.*, 61,582 (1983).
- [3.9] L.Pomathiod, R. Debrie, Y.Arnal and J. Pelletier, *Phys. Lett.*, 106A,301 (1984).
- [3.10] S.R. Mejia, R.D. McLeod, K.C. Kao and H.C. Card, *J. Non-Cryst. Solids* 59&60,727 (1983).
- [3.11] A. Matsuda, *J. Non-Cryst. Solids*, 59&60, 767 (1983).

## CHAPTER 4

### Activated Reactive Evaporation of $a-Si:H$ \*

The activated reactive evaporation system was developed to enable the achievement of uniform deposition and high deposition rates together with the ability to incorporate hydrogen into the growing film. The development of the current system was performed in collaboration with W. Pries, S.R. Meija and film characterization with W. Pries and T.V. Herak. Subsequent investigations by P. Shufflebotham have included studying the effect of  $N_2$  as an additional reactant gas. Specifically, Chapter 4 presents the electrical and optical properties of  $a-Si:H$  prepared by Activated Reactive Evaporation (ARE). Thin film properties were measured for various partial pressures of hydrogen. Incorporation of both atomic and molecular hydrogen is implied by the behavior of the dark conductivity, which decreased from approximately  $10^{-4}(\Omega cm)^{-1}$ , to less than  $10^{-8}(\Omega cm)^{-1}$ , with a corresponding increase in the optical gap from 1.4 to 1.7 eV. The incorporation of atomic hydrogen was facilitated by increasing the reaction probe voltage.

#### 4.1. Introductory Remarks

The present studies are motivated by the potential benefits of developing alternative methods for the fabrication of amorphous semiconductors. Electron-beam evaporation is inherently an attractive method of depositing amorphous silicon and silicon based compounds, but has several limitations including lack of control of unwanted impurities, and the difficulty of incorporating atomic hydrogen. Several groups have been studying e-beam systems which attempt to overcome these difficulties [4.1-4.3], and have met with limited success. This chapter discusses an alternative evaporation technique, activated reactive evaporation (ARE) [4.4], which is also designed to overcome the difficulties associated with e-beam evaporation of  $Si$ . Activated reactive evaporation has been used for incorporation of  $C$  in  $TiC$  [4.4],  $O$  in  $Al_2O_3$  [4.5], and  $N$  in  $TiN_x$  [4.6] deposits, but to the best of our knowledge ARE has not previously been employed for the deposition of  $a-Si:H$ . The techniques and results presented in this paper indicate that ARE reduces the

---

The contents of this chapter has been accepted for publication in Journal de Physique.

difficulties associated with conventional *Si* evaporation systems and demonstrates the capability of incorporating molecular or atomic hydrogen into the films.

## 4.2. Experimental Techniques

Activated reactive evaporation (ARE) was originally developed in order to obtain high deposition rates for compounds such as *TiC* [4.4]. In the present study high purity *Si* is evaporated from an electron-beam-heated source in a hydrogen partial pressure of  $10^{-4}$  to  $10^{-3}$  torr. To enhance atomic hydrogen incorporation, an electrode is placed in the reaction zone as shown in Fig.4.1. The probe is held at a positive potential (100-500V), which draws primary and secondary electrons into the reaction zone, and ionizes and activates the reactant gas. It is believed that a process similar to corona discharge also enhances the ionization.

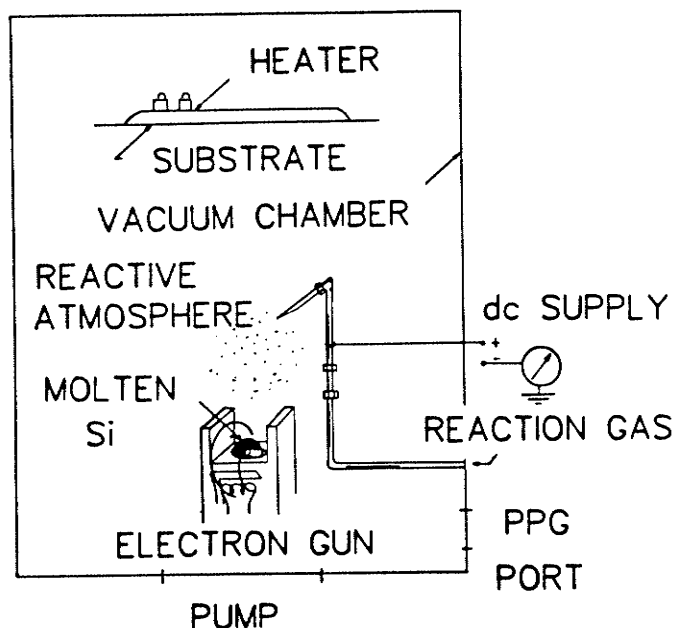


Figure 4.1: Schematic of the ARE deposition system.

For the results presented in this section, the following deposition conditions were employed: e-beam current 200 mA at 4000V potential, initial vacuum  $\approx 4 \times 10^{-7}$  torr, probe voltage 0 or 200V, hydrogen partial pressure varied in range  $10^{-4}$  to  $10^{-3}$  torr, and substrate temperature  $200^\circ$  C.

### 4.3. Film Characterization

Scanning electron microscopy with X-ray microanalysis, IR and visible spectrophotometry, ellipsometry, conductivity and photoconductivity were again the principal methods used to characterize the deposited films.

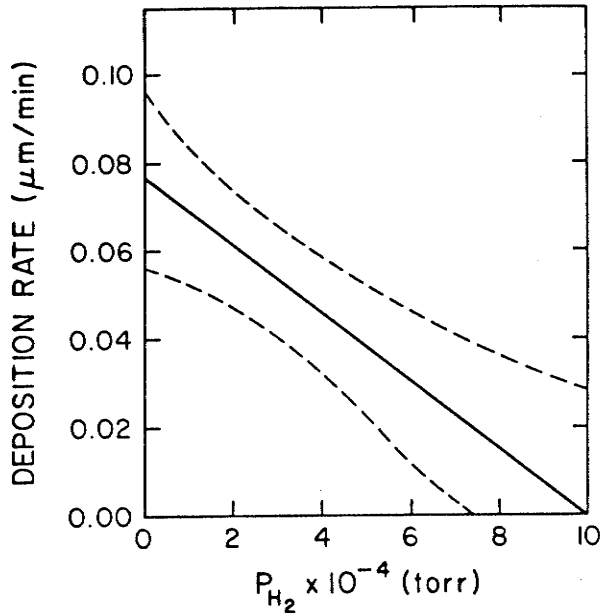


Figure 4.2: Deposition rate ( $\mu\text{m}/\text{min}$ ) vs. partial pressure of  $H_2$ . Dashed lines represents the 90% confidence limits.

Figure 4.2 illustrates the dependence of the deposition rate upon the partial pressure. The deposition rate was found to be invariant to the probe voltage. The variation in deposition rate at a given partial pressure of  $H_2$  has been attributed to the properties and size of the melt, and to variations in thermal conductivity at the interface between the melt and the crucible. Excellent film uniformity was obtained when a 10 inch separation was maintained between melt and substrate as evidenced by spectrophotometry results; this was corroborated by a well-defined extinction in ellipsometry measurements.

Figure 4.3 shows the typical dependence of the dark conductivity and its activation energy for the  $a\text{-Si:H}$  films upon partial pressure of  $H_2$ , for samples prepared at probe potentials of 0 and 200 V. Intermediate results are obtained at lower probe voltages. The dark conductivity and activation energy associated with the ARE fabrication technique at a partial pressure of  $H_2$  of  $\approx 6 \times 10^{-4}$  torr are comparable to r.f. glow discharge-produced films. This correspondence provides evidence of effective ionization and dissociation

of the reactant gas with the subsequent incorporation of atomic hydrogen in the growing film. A similar correspondence has been demonstrated by our group (unpublished results) between ARE-fabricated films and hydrogen ion implantation of e-beam evaporation films. Although we have not shown the results here, a significant reduction was observed in the photoconductivity as compared to rf glow-discharge films. Investigations of the absorption bands at  $640\text{cm}^{-1}$  and  $1050\text{cm}^{-1}$  by IR spectroscopy indicate that a significant amount of oxygen is incorporated into the films when the  $H_2$  partial pressure is high. The degree of O incorporation is observed to increase as the partial pressure of  $H_2$  increases. This may be a direct consequence of the reduced deposition rate which accompanies the increase in the partial pressure of  $H_2$ .

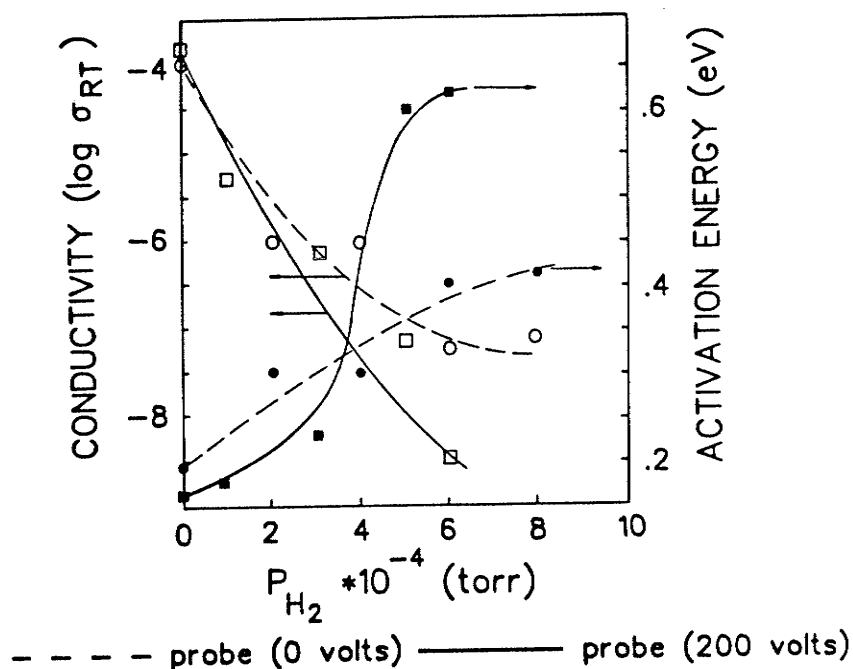


Figure 4.3: Conductivity and extended state activation energy vs. partial pressure of  $H_2$ , corresponding to probe voltages of 0 and 200 volts.

Figure 4.4 illustrates the dependence of the refractive index ( $n$ ) at long wavelengths upon the partial pressure, again for samples prepared with probe voltages of 0 and 200 V. The initial decrease in  $n$  is attributed to the saturation of dangling bonds with a corresponding decrease in the ESR signal [4.7]. Due to the exceptionally high defect density of e-beam evaporated  $a-Si$  [4.8], almost any element or compound incorporated into the growing films will reduce the long wavelength refractive index. For the films prepared with zero

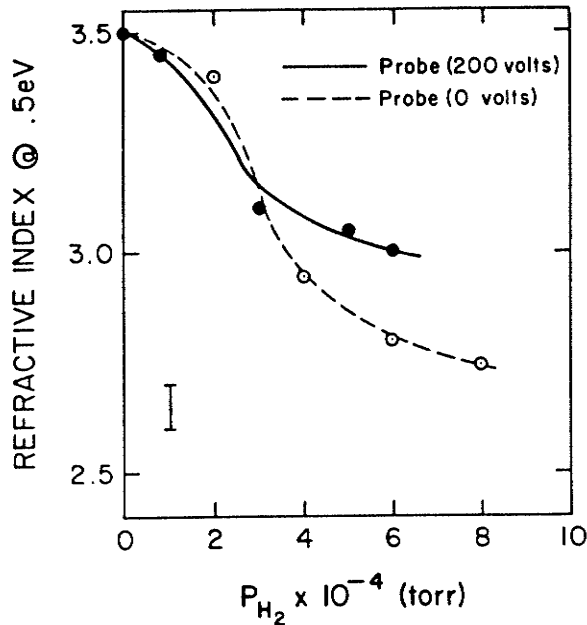


Figure 4.4: Refractive index at 0.5 eV (long wavelength) vs. partial pressure of  $H_2$ , corresponding to probe voltage of 0 and 200 volts.

probe voltage, there is a significant decrease in  $n$  below 3.0 for films evaporated in a partial pressure of  $H_2$  greater than  $4 \times 10^{-4}$  torr. This evidence supports arguments [4.9] that substantial oxygen is being incorporated into the growing film which plays a major role in determining the characteristics of the films. On the other hand, for films prepared at a 200 V probe potential, the refractive index tends towards a value of 3.0, comparable to r.f. glow-discharge films. These results offer evidence that the probe is effective in incorporating atomic hydrogen into the growing film. Thus it can be argued that, as expected atomic hydrogen is much more effective than molecular  $H_2$  in suppressing the effect of impurities such as oxygen.

From spectrally-resolved ellipsometry and spectrophotometry results, we have inferred the value of the optical energy gap  $E_{opt}$ , by assuming parabolic bands for the extended states. The dependence of  $E_{opt}$  upon hydrogen partial pressure and probe voltage is shown in Fig.4.5. The films prepared in the reactive atmosphere (probe voltage 200V) consistently demonstrated a larger optical gap than those prepared with zero probe voltage. The difference in  $E_{opt}$  in the two cases, at a given partial pressure of  $H_2$ , provides additional evidence that atomic hydrogen is being incorporated into the growing film. Qualitatively, the  $Si-H$  bonds are expected to be somewhat stronger than

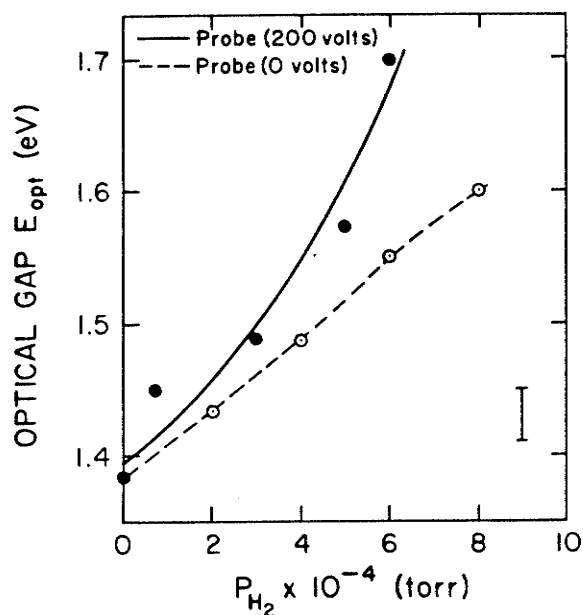


Figure 4.5: Optical gap  $E_{opt}$  vs. partial pressure of  $H_2$ , corresponding to probe voltages of 0 and 200 volts.

$Si-H_2-Si$  or  $Si-Si$  bonds and are responsible for the observed difference in  $E_{opt}$ . This line of reasoning is consistent with the quantum well model of  $a-Si:H$  presented by Brodsky [4.10]. Recently Talukder et.al. [4.11] have more convincingly demonstrated effective atomic hydrogen incorporation in a very similar system. Although they did not report the photoconductivity directly, it can be inferred from their results that it was significantly reduced due to oxygen incorporation. More recently, our laboratory has measured electrical and optical properties of films prepared by electron beam evaporation with simultaneous  $H$  ion implantation, in collaboration with S. Iselborn in Germany. Our results indicate that the oxygen incorporation problem can be overcome by this technique while still exploiting the advantages of electron beam evaporation. It should be mentioned at this time that subsequent studies by P. Shufflebotham indicate that, at least for a reactant gas including nitrogen, there is little evidence to support gas phase reactions. Instead, there appears strong evidence to support substrate surface reactions.

#### **4.4. Conclusions of Chapter 4**

On the basis of the present study of  $a-Si:H$  films prepared by the ARE technique, the following conclusions are drawn:

- 1) ARE provides an effective method for the incorporation of atomic hydrogen into the amorphous  $Si$  network, for films fabricated by electron-beam evaporation.
- 2) The degree of incorporation of atomic or molecular hydrogen can be controlled by the applied probe voltage.
- 3) Both a high deposition rate and excellent film thickness uniformity are associated with the ARE fabrication technology.

#### 4.5. References for Chapter 4

- [4.1] D. Kaplan, N. Sol and G. Valasco, Appl. Phys. Lett., 33, 440 (1978).
- [4.2] M. Shindo, S. Sato, I. Myokan, S. Mano and T. Shibata, J. of Non-Cryst. Solids, 59-60, 747 (1983).
- [4.3] V. Grasso, A.M. Mezzasalma and F. Neri, Solid State Comm., 41, 675 (1982).
- [4.4] A.C. Raghuram and R.F. Bunshah, J. Vac. Sci. Technol. 9, 1389 (1972).
- [4.5] A.C. Raghuram and R.F. Bunshah, J. Vac. Sci. Technol. 9, 1385 (1972).
- [4.6] P.J. Martin, R.P. Netterfield and W.G. Sainty, Vacuum 32, 359 (1982).
- [4.7] M.H. Brodsky, R.S. Title, K. Weiser and G.D. Pettit, Phys. Rev. B., 1, 2632 (1970).
- [4.8] F. Schwidofsky, Thin Solid Films 18, 45 (1973).
- [4.9] N.F. Mott and E.A. Davis, *Electronic Processes in Non-Crystalline Materials*, 2nd Ed. (Clarendon, Oxford, 1979).
- [4.10] M.H. Brodsky, Solid State Comm., 36, 55 (1980).
- [4.11] G. Talukder, J.A. Cowan, D.E. Brodie, and J.D. Leslie, Can. J. Phys., 62,848 (1984).

# CHAPTER 5

## *a-Si:H* for Archival Storage \*

### 5.1. Introductory Remarks

This work was an outgrowth of our investigations into novel applications for *a-Si:H*. Film deposition and laser processing were done in collaboration with W. Pries.

Specifically, Chapter 5 presents changes in the optical reflectivity of *a-Si:H* films, of up to 90%, induced by *Ar* laser processing. These findings are correlated with hydrogen evolution. Concomitant changes of more than 3 orders of magnitude in conductivity also provide a mechanism for interrogation of stored data by an electron beam. Potential archival storage densities as high as  $10^9 \text{bits/in}^2$  for optical recording and  $10^{11} \text{bits/in}^2$  for recording with electron beams are predicted on the basis of these results.

### 5.2. Archival Storage Media

The development of modern computer systems must contend with the seemingly insatiable need of these systems for increased densities of stored digital information. Much of the early work on optical storage media has focused on amorphous semiconductor materials such as tellurium and related compounds or on polymers. Recently amorphous silicon has also emerged as a candidate for an archival storage medium. Mechanisms for optical storage in amorphous silicon that depend upon optically-induced amorphous to polycrystalline transitions [5.1], or upon release of hydrogen from *a-Si:H* to produce either bubbling (local deformation) or ablative hole formation [5.2] have also been proposed.

In this chapter, we describe additional mechanisms by which *a-Si:H* thin-film materials can function as high-density archival storage media, both in optical and electron-beam addressed systems. The experiments we describe are concerned with the modifications to the bulk reflectivity and to the conductivity of *a-Si:H* that result from the release of hydrogen from the material, induced by either laser or electron-beam irradiation. These mechanisms do

The contents of this chapter have been published in Applied Physics Lett., 45, pp.628-30, 1984.

not appear to result in rupture or distortion of the material and are potentially reversible by rehydrogenation, although reversibility is not addressed here experimentally. Our primary concern is with read-only archival storage.

### 5.3. Experimental Details

The optically-induced evolution of hydrogen was accomplished using an Argon laser (514 nm) in a CW-scanning mode over a relatively large area (100  $\mu\text{m}$  x 2 cm. regions) for times of typically 5 mins. The laser power was varied over the range 100 mW to 1 W. This implies a power density more than an order of magnitude below that required by earlier methods; see Ref.5.2, for example. Another departure from the conditions of the earlier work was that we employed rf glow discharge *a-Si:H* films on quartz substrates rather than films reactively sputtered onto glass. These conditions may have contributed to the uniform changes in electrical and optical properties in our experiment which, coupled with the lower optical power densities, may prohibit structural deformations that accompany pulsed laser operation at small spot sizes as in the earlier papers [5.2].

The *a-Si:H* films were deposited in a conventional radio-frequency glow-discharge system at a power density of  $0.1\text{W cm}^{-2}$  and a pressure of 0.1 torr in a  $\text{SiH}_4/\text{H}_2$  atmosphere (1/1 ratio) on quartz substrates at a substrate temperature of  $200^\circ\text{C}$ . Typical film thicknesses were  $0.3\ \mu\text{m}$ .

### 5.4. Discussion

In Fig.5.1 we show the dependence of optical reflectivity and electrical conductivity upon the hydrogen content, of the *a-Si:H* films, remaining after either Ar laser irradiation or thermal annealing. The reflectivity was measured at a wavelength of 632.8 nm, and is presented in Fig.5.1 as  $\Delta R/R$  where  $\Delta R$  is the induced reflectivity change. The hydrogen content could be controlled either by the power of the Ar laser or by the duration of the irradiation. This hydrogen content was calibrated by comparison with identical films in which the H diffusion from the films was stimulated thermally at  $400^\circ\text{C}$ . In the thermal-evolution experiments the H/Si ratio in the films was established by comparison of our electrical and optical data with earlier work [5.3,5.4]. This was subsequently confirmed by infrared absorption measurements of the H content [5.5].

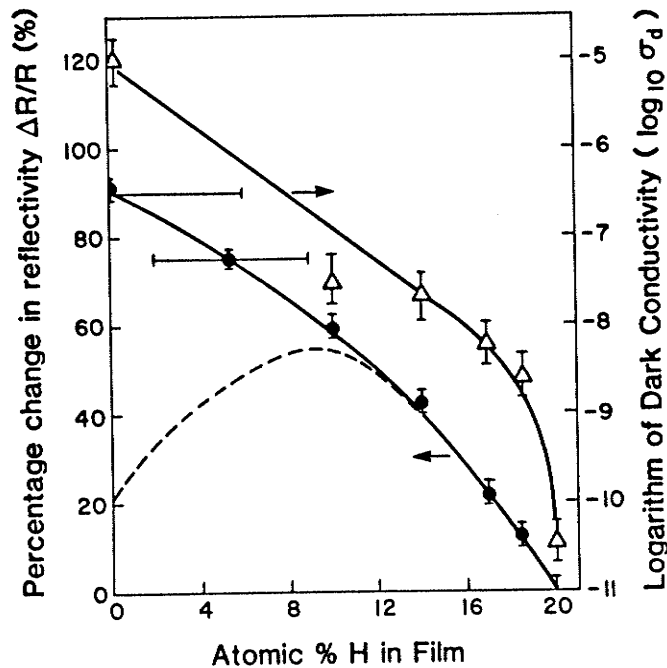


Figure 5.1: Ratio of change in optical reflectivity to original reflectivity, measured at  $\lambda = 632.8 \text{ nm}$ , and the electrical conductivity (in  $S \text{ cm}^{-1}$ ) of  $a\text{-Si:H}$  film (thickness  $0.3 \mu\text{m}$ ) vs. remaining H content following Ar laser irradiation ( $514 \text{ nm}$ ) or thermal annealing. Dashed line indicates theoretical calculations based upon a simple two layer film model [5.7].

We have also observed the hydrogen evolution directly by in situ measurements using mass spectrometry during electron-beam irradiation of the  $a\text{-Si:H}$  material under high vacuum, but these measurements are of a qualitative nature. It is interesting to note that for the films thickness in Fig.5.1 and the wavelength used in the reflectivity measurements, an amorphous to crystalline transition would cause the opposite trend to that of Fig.5.1 (reflectivity would increase, rather than decrease as in Fig.5.1) [5.5]. No evidence of structural change was observed by scanning electron microscopy although the resolution of our instrument was restricted to approximately  $1 \mu\text{m}$ .

It is also important to realize that the degree of change in the reflectivity as well as the direction of change induced by the hydrogen evolution is a damped periodic function of the optical path length through the film

(determined by  $\lambda$  and the film thickness). We have conducted independent measurements of the refractive index and extinction coefficient for the  $a-Si:H$  materials; results are shown in Fig.5.2. These results are in reasonable agreement with earlier studies of sputtered  $a-Si:H$  [5.6], and have been used to predict the reflectivity changes as a function of film thickness, wavelength, and  $H$  content [5.10]. We have found that the  $H$  content of  $a-Si:H$  films is the predominant factor in determining  $n$  and  $k$ . Alternative fabrication techniques and process parameters have a minimal effect on  $n$  and  $k$  except to the extent that they affect the  $H$  content [5.5]. An optical model of the film-substrate system [5.7] was employed which includes the absorption (also measured as a function of  $H$  content) in the  $a-Si:H$  film. These calculations are in excellent agreement with experiments in which the  $H$  evolution was induced thermally, over a range of film thickness, which suggest that the hydrogen content remaining in the film is uniformly distributed in that case.

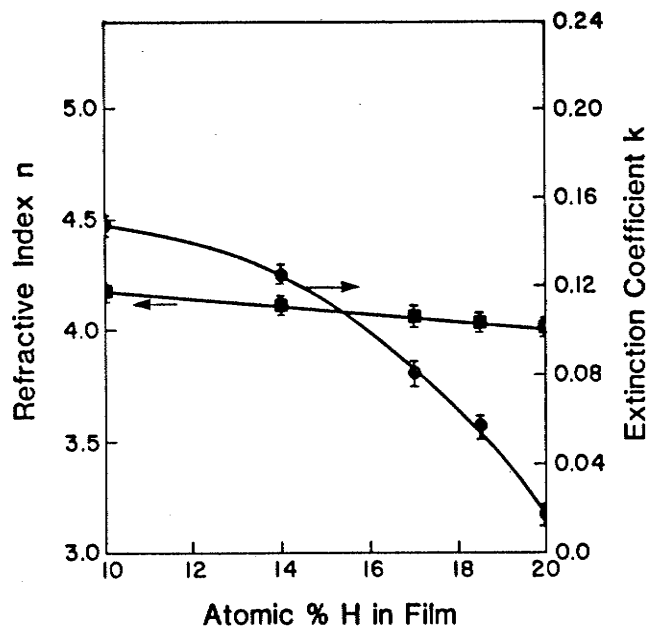


Figure 5.2: Refractive index  $n$  and the extinction coefficient  $k$  vs.  $H$  content in  $a-Si:H$  film ( $d = 0.3 \mu m$ ).

For the laser-induced changes in reflectivity of Fig.5.1, there is agreement with the optical model (same  $n$  and  $k$  values for a given  $H$  content) for the

larger  $H$  concentration ( $> 10\text{at}\%H$ ). The dashed line in Fig.5.1 shows the model predictions. Sustained laser irradiation which further reduces the  $H$  content results in non-uniform optical properties throughout the film. This is a fortunate development since it increases the desired effect on  $\Delta R$  as is evident in Fig.5.1.

The hydrogen effusion discussed above was also induced by electron-beam irradiation at an energy of 4 KeV, with a change in the monitored  $H_2$  partial pressure from  $2.5 \times 10^{-8}$  torr to  $4.5 \times 10^{-7}$  torr during  $H$  evolution. The conductivity changes of Fig.5.1 suggest a means by which the stored information may be interrogated using an electron beam. This would be similar to the method by which photoconductive regions are identified in a vidicon tube.

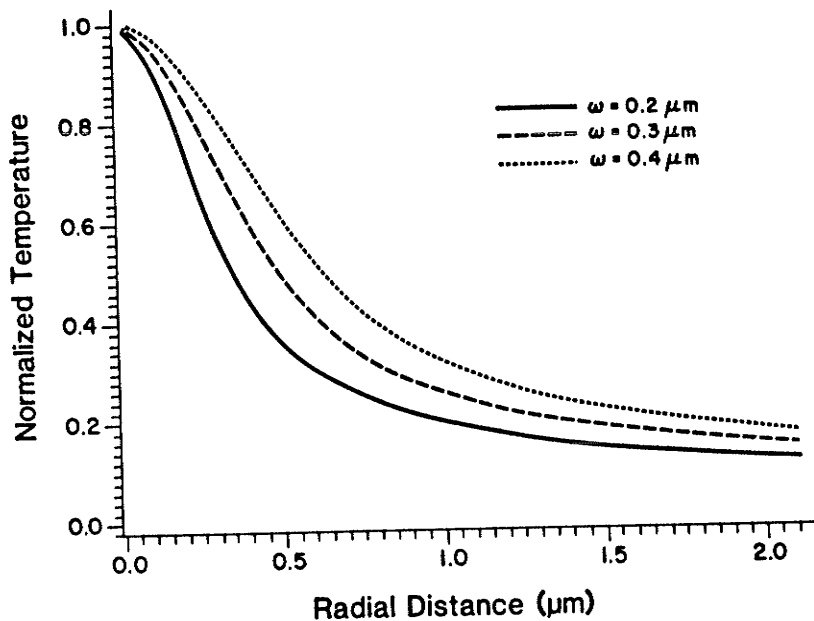


Figure 5.3: Normalized excess temperature profiles ( $T - T_{\text{ambient}}$ ) during steady-state argon laser irradiation for various Gaussian intensity distributions  $I = I_0 \exp(-r^2/\omega^2)$  with  $T_{\text{max}} = I_0 \pi^{1/2} \omega / 2k$  where  $\omega =$  beam waist and  $k =$  thermal conductivity.

## 5.5. Conclusions of Chapter 5

As an optical storage medium, a  $-Si:H$  which undergoes a process of laser or electron beam-induced hydrogen evolution is expected to have an ultimate storage density limited by the following considerations. As the medium is locally elevated in temperature by the deposited energy from the beam, the material surrounding the cylinder will also experience a temperature rise due to thermal conduction. This process has been modelled using the method of Lax [5.8] and assuming the worst-case conditions of steady-state irradiation, the resultant temperature profiles are as in Fig.5.3. Assuming that the rate of  $H$  evolution is negligible below  $400^{\circ} C$  [5.4], in view of the short times in the laser irradiation case, these results indicate that the maximum storage densities are in the range of  $10^9 \text{ bits/in}^2$  for laser irradiation (cell size  $1 \mu\text{m}$ , spot size  $0.6 \mu\text{m}$ ). Similar temperature distribution profiles were calculated for the electron-beam irradiation case, following a method outlined by Schiller et.al. [5.9]. As a result of the reduced electron-beam diameter, the maximum storage density is expected to be in the range of  $10^{11} \text{ bits/in}^2$  (cell size  $0.1 \mu\text{m}$ , spot size  $0.01 \mu\text{m}$ ). The above considerations suggest that the limitations are no worse than those which arise from diffraction effects. As a final note, it is expected that some fraction of the evolved hydrogen will be incorporated around the edges of the programmed area, leading to a self-enhancing contrast mechanism.

## 5.6. References for Chapter 5

- [5.1] M. Janai and F. Moser, J. Appl. Phys., 53, 1385 (1982).
- [5.2] M.A. Bosch, Appl. Phys. Lett., 40, 8 (1982).
- [5.3] N. Fukada, T. Imura, A. Hiraki, T. Itahashi, T. Fukuda, M. Tanaka, Japan. J. Appl. Phys. (Lett.), 21, 532 (1983).
- [5.4] W. Beyer and H. Wagner, J. Non-Cryst. Solids, 59-60, 151 (1983).
- [5.5] W. Pries and R.D. McLeod, unpublished results.
- [5.6] E.C. Freeman and W. Paul, Phys. Rev. B, 20, 716 (1979).
- [5.7] O.S. Heavens, Optical Properties of Thin Solid Films, Dover Press, pp. 74-78 (1965).
- [5.8] M. Lax, J. Appl. Phys., 48, 3919 (1977).
- [5.9] S. Schiller, U. Heisig, and S. Panzer, Electron Beam Technology, John Wiley & Sons, pp. 365-447 (1982).
- [5.10] W. Pries, R.D. McLeod, H.C. Card and K.C. Kao, Appl. Phys. Lett., 45, 734 (1984).

# CHAPTER 6

## Interpretation of Amorphous Silicon Behavior using Fractal Geometry

### 6.1. Introduction

Chapter 6 advances a discussion of fractal geometry which we consider as providing an alternative and useful perspective for the study of disordered semiconductors, in particular of hydrogenated amorphous silicon ( $a-Si:H$ ) systems. Fractal concepts have already proved very successful in the interpretation of many physical phenomena in disordered solids such as polymers and glasses. This is intended to be a theoretical chapter motivated by recent experimental results and anomalies, and their interpretation in light of the results from the currently active research area of fractal phenomena. Its intent is to stimulate a fresh perspective for the description of disordered systems. The chapter begins with a brief introduction of the concepts of fractal geometry. Although there are a number of non-integral dimensions associated with fractal geometry, only the Hausdorff-Besicovitch or *fractal* dimension and the spectral or *fracton* dimension will be reviewed. Following this brief digression experimental evidence relating amorphous silicon to fractal concepts will be presented. The final section is intended to correlate the experimental observations with consistent explanations based upon the notion of fractals.

### 6.2. Background: Fractal Geometry

The renaissance of the mathematical concept of fractals and their description of natural physical systems has largely been due to a collection of essays by B. Mandelbrot [6.1]. This somewhat unreadable book has sparked the imagination of many researchers in a wide variety of disciplines [6.2-6.5]. The most familiar systems studied are usually those best described by their Euclidean dimension; in actuality these systems can be considered to be geometrically degenerate, in that the fractal dimension corresponds to the normal Euclidean dimension. These familiar systems can be considered to be a subset of a larger class of systems where the fractal dimension is not necessarily integral; in fact, in most cases, the fractal dimension is non-integral and somewhat less than the embedding Euclidean dimension. Underlying the basic concept of fractal geometry is the notion of dilation invariance. Dilation invariance implies that, independent of the scale that is used to view the

object, the structure is always the same or self-similar. This may, in certain cases, only apply for special values of the scaling ratio.

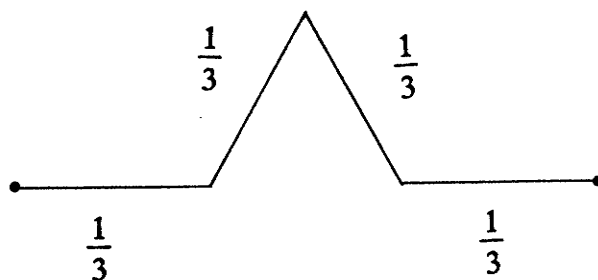


Figure 6.1: Generator used in the construction of a fractal curve.

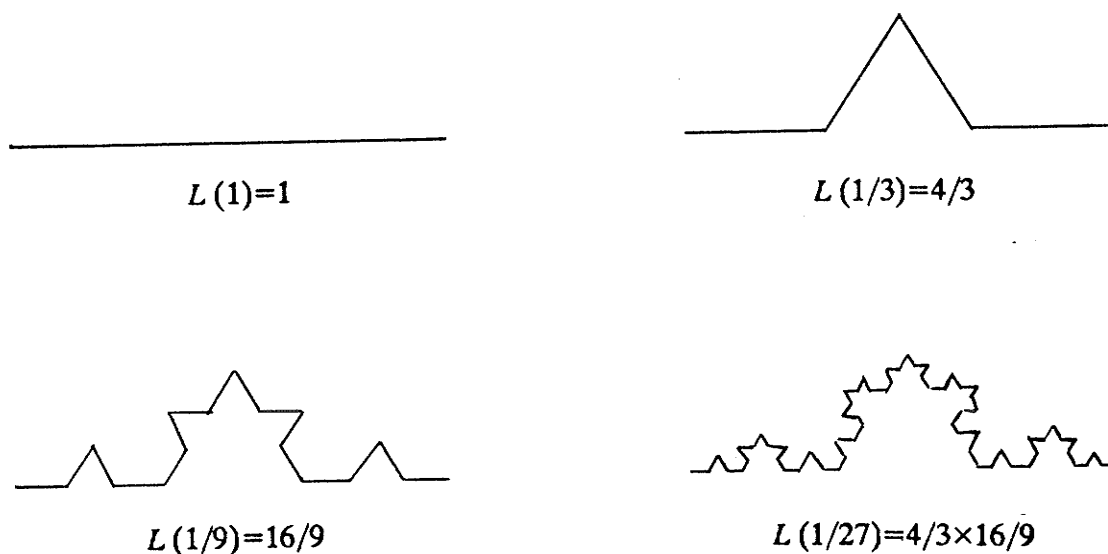


Figure 6.2: Generation of the fractal curve by iteratively applying the generator of Fig.6.1.

To illustrate this concept, the following section will contain two examples of deterministic fractals. The first example is a curve and the second a planar pattern; both represent fractal structures in a 2-dimensional embedding Euclidean space.

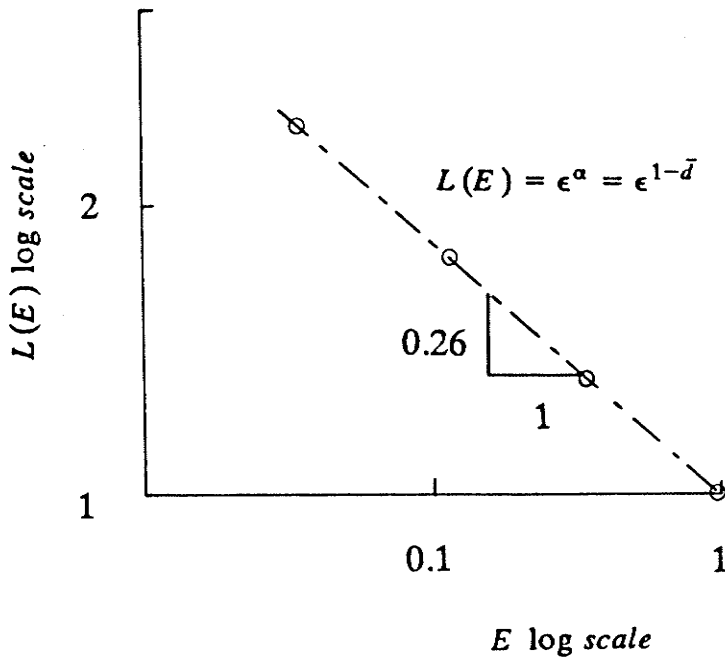


Figure 6.3: Measured length of the fractal curve as a function of the measuring rod.

In both cases we will start with a generator or rule which may be used to construct the fractal pattern [6.1]. In the case of the curve we begin with a straight line segment whose length is unity. We select the trivial generator shown in Fig.6.1, whose length is  $4/3$  units. By recursively applying the generator to all straight line segments a curve will evolve as shown in Fig.6.2. Figure 6.3 illustrates  $\log L(\epsilon)$  where  $L(\epsilon)$  is the total length of the curve as a function of the measuring unit  $\epsilon$ . This measuring unit  $\epsilon$  disregards structure on any scale finer than  $\epsilon$  [6.1]. Since the functional dependence on a log-log plot is a straight line the curves can be represented by the expression

$$L(\epsilon) \approx \epsilon^\alpha \tag{6.1}$$

where  $\approx$  is to be interpreted as 'proportional to'. If the object were merely a straight line the length would be independent of the scale which would imply  $\alpha=0$ , or equivalently  $\alpha=1-\bar{d}$  where  $\bar{d}$  is the fractal dimension, which in the uniform structure would be equivalent to the topological dimension of unity for the curve. In Fig.6.3,  $\alpha$  represents the slope which is equal to  $-0.2618$  from which  $\bar{d}=1.2618$ . As this is a deterministic fractal  $\bar{d}$  can be analytically determined to be  $\log 4/\log 3$ . This dimension  $\bar{d}$  is denoted the fractal, Hausdorff-Besicovitch or simply Hausdorff dimension. The previous discussion is an example of a

curve whose fractal dimension exceeds the topological dimension of the curve but is less than the Euclidean dimension of the embedding space. The Hausdorff dimension is the clearest manifestation of all fractal dimensions, although not necessarily the most important for all purposes. Figure 6.2 is often referred to as a Koch curve.

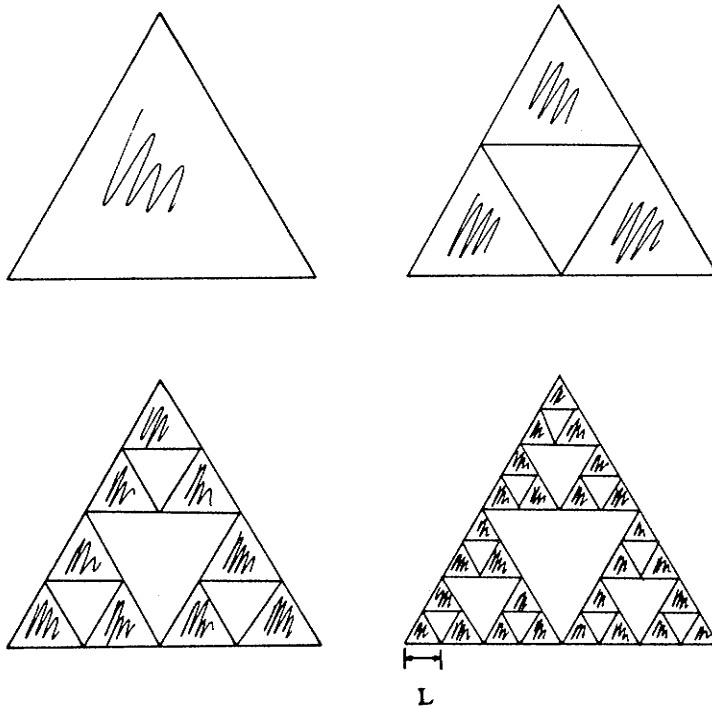


Figure 6.4: Generation of a fractal by iteratively removing the inner triangular regions.

The second example is extracted from [6.5] and is a particularly clear illustration of a fractal pattern whose encompassing Euclidean dimension is 2. Again one starts with a generator, in this case an equilateral triangle. The rule to follow in constructing this fractal pattern is to remove the centre of each triangle to exhaustion, as illustrated in Fig.6.4.

To facilitate the discussion we will now concern ourselves with *density* on various length scales. Considering the smallest triangle of Fig.6.4, the density is the "mass" divided by the area. Letting  $L$  represent the length of the an edge of one of the smallest triangles, the density  $\rho$  can be expressed as  $\rho(L) \approx M/L^2$  where  $M$  is the mass of the smallest triangle. Considering now the next smallest triangle, it is clear that the mass has increased by a factor of 3 but that the area has increased by a factor of 4, that is  $\rho(2L) = 3/4\rho(L)$ .

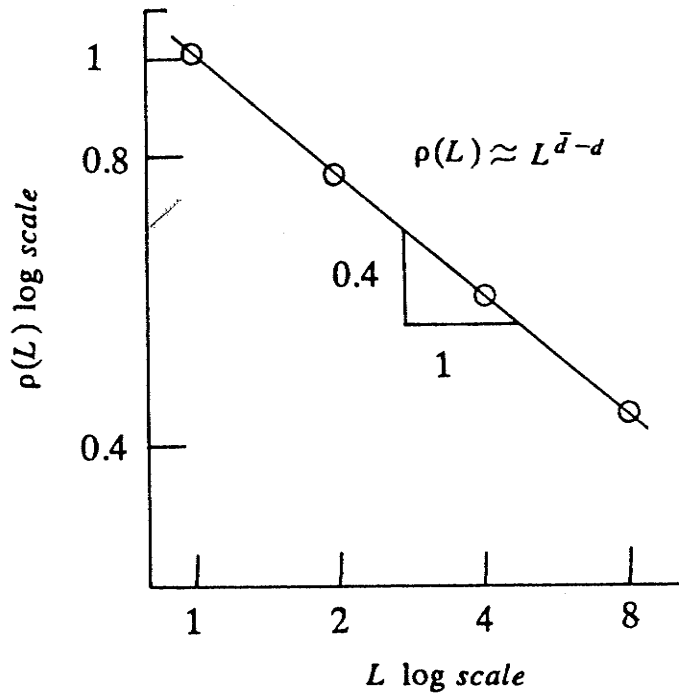


Figure 6.5: Density of the fractal pattern as a function of the measuring unit

Similarly, one can define the density for various length scales; the results are plotted in Fig.6.5. Here again a log-log plot results in a straight line, which implies

$$\rho(L) \approx L^{\bar{d}-d} \quad (6.2)$$

Recall that we are now concerned with density, such that the exponent is expressed as  $\bar{d}-d$ , as opposed to the length in the fractal curve case where the exponent was expressed as  $d-\bar{d}$ . In the case of this example,  $d=2$ , the dimension of the embedding Euclidian space. From Fig.6.5,  $\bar{d}$  can be readily deduced to be 1.6 or expressed analytically as  $\ln 3/\ln 2$ . Figure 6.4 illustrates a manifestation of a fractal pattern whose Hausdorff dimension is again less than the embedding Euclidean dimension. The structure of Fig.6.4 is often referred to as a Sierpinski gasket.

Some general observations are in order at this time: i) Both the Koch curve and the Sierpinski gasket readily demonstrate dilation symmetry (provided the proper scaling ratio is employed). That is, independent of the length scale the basic structure remains invariant; ii) Both fractal structures are deterministic structures generated by a simple non-random rule; and iii) Both the

Koch curve and the Sierpinski gasket represent fractal structures whose Hausdorff dimension is less than the embedding Euclidean dimension, a direct consequence of not being able to fill more space than that offered by the Euclidean dimension.

Another important fractal dimension to be considered is the fracton or spectral dimension  $\bar{d}$ . The spectral dimension is associated with the low frequency density of states for lattice vibrations, that is,

$$\rho(\omega) \approx \omega^{\bar{d}-1} \quad (6.3)$$

The spectral dimension is less tangible than either the embedding Euclidean dimension or the Hausdorff dimension, but is no less important. Based upon results of extensive simulation Alexander and Orbach [6.7] have conjectured that the fracton dimension is equal to 4/3, independent of  $d$  or  $\bar{d}$ ; this has since been coined the Alexander-Orbach conjecture. This conjecture appeared to postulate a superuniversality based upon the invariance of  $\bar{d}$ . Recently, Stanley et.al. [6.20] have considered the range of the AO conjecture and subsequently postulated that this conjecture only applies to certain classes of fractals, although by no means to a small class.

### 6.3. Experimentally Observed Properties of $a-Si:H$

There are several reasons for anticipation of fractal behavior in amorphous semiconductors such as  $a-Si:H$ , quite apart from successful application of fractal geometry to other disordered systems. Firstly amorphous materials cannot be characterized by a translationally invariant lattice. As previously stated this is a necessary although not sufficient condition for the manifestation of fractal behavior. Amorphous materials such as  $a-Si:H$  are also known to contain voids of various sizes. If there are enough voids of various sizes there may be reason to suspect self-similarity or geometrical features over a range of length scales and hence to expect certain fractal characteristics. In the case of  $a-Si:H$  where in most cases the incorporation of atomic hydrogen ( $\geq 10$  at.%) can be considered as alloying, there may be reason to suspect nucleation at the location where the hydrogen is likely to bond. This is so particularly if the hydrogen is concentrated in clusters around the void distribution, as opposed to a purely random model of homogeneous hydrogen incorporation. Most  $a-Si:H$  films are grown under relatively low temperature fabrication processes, and as such minimum energy configurations

are not to be expected for the solid. Many growth models of physical growth processes are currently being simulated by fractal aggregation; these include the growth of polymer chains and dendritic growth [6.8]. Electron transport in  $a-Si:H$  may be viewed as a percolation process, again presenting a basis for fractal structure. It can be argued that the  $Si-H$  bonds act as percolation impedances similar to the termites walk on percolating clusters. It is for these reasons, and in view of the difficulties of treating disordered systems by techniques originally developed for conventional solids, that the hypothesis of this chapter is put forward. In this section experimental consequences of the assumed fractal structure will be presented.

### 6.3.1. Experimental DOS

Recently X-ray inverse photoemission techniques [6.9] were used to determine the conduction-band density of states in  $a-Si:H$ . This work was motivated by the desire to determine the effect of long-range disorder and hydrogen incorporation on the electronic and optical properties of solids. For example, the nature of the conduction band density of states (DOS) determines the electron transport and the location of the mobility edge. Also analysis of optical measurements often depends upon the convolution of the valence- and conduction-band densities of states. In fact, a result which has been utilized extensively earlier in this thesis and ubiquitously throughout the literature in determining the optical gap is based upon assuming a density of states with a square-root dependence on energy near the band edges. The valence band DOS has been measured quite accurately by means of photoemission spectroscopy [6.10] but no comparable measurements were available for determination of the conduction-band DOS until recently [6.9]. Initial speculation of a non-parabolic DOS arose from the determination of  $E_{opt}$  for  $a-Si:H$  films [6.11]. Plots of  $(\alpha h\nu)^{1/3}$  when plotted against  $h\nu$  resulted in a better fit than when  $(\alpha h\nu)^{1/2}$  was plotted. No detailed explanation was given at that time to indicate the shape of the conduction-band DOS, although this curve fitting suggested a linear energy dependence of the DOS. The X-ray inverse photoemission corroborated this postulate. In the future the literature should presumably contain  $E_{opt}$  derived from  $(\alpha h\nu)^{1/3}$ , based upon assumptions of a linear DOS in order to be consistent with experimental observations. Without regard for details it is quite easy to see how the 1/3 power would arise from a linear DOS. The absorption can be expressed as a convolution

integral involving the conduction- and valence-band (DOS) as follows

$$\alpha = \int D_v(E) D_c(h\nu - E) dE \quad (6.4)$$

where  $D_v(E)$  and  $D_c(E)$  represent the valence- and conduction- band DOS. If  $D_v(E)$  and  $D_c(E)$  are approximated as linear functions of energy, the product will contain an  $E^2$  dependence, and upon integration an  $E^3$  dependence, which in turn justifies the  $1/3$  power of  $\alpha$ . The details which were ignored in the above discussion are related to arguments of constant matrix elements connecting states in the valence- and conduction-bands. One additional feature to add to these observations is based upon the experimentally determined absorption coefficient  $\alpha$ . The absorption coefficient  $\alpha$  for interband absorption (where the photon energy  $h\nu > E_{opt}$ ) for  $a-Si:H$  is characteristically greater than  $\alpha$  for crystalline  $Si$ . This phenomena has often been attributed to a relaxation of the momentum conservation requirement for photon absorption. The final section of this chapter will attempt to illustrate how similar functional dependences can be obtained from an underlying fractal geometrical structure.

### 6.3.2. Dispersive Transport and $a-Si:H$

Additional experimental evidence for fractal behavior also arises in the area of transport phenomena. Specifically, we note that several recent investigations of transient photocurrents in  $a-Si:H$  have provided evidence for dispersive transport [6.12]. The long tail of the transient photocurrent  $I(t)$  indicates a dispersion of the carrier transit times. Scher and Montroll [6.13] developed a stochastic transport model based upon a time-dependent random walk, where the time dependence of the random walk is governed by a waiting time distribution  $\psi(t)$  for carriers hopping between sites. The model Scher and Montroll advanced in explanation of their results was based upon dividing the material into a lattice of regular cells, each cell containing many randomly distributed localized sites available for hopping carriers. The disorder of the amorphous material is therefore incorporated in their case completely in the hopping time distribution  $\psi(t)$ . Transient photo-conductivity was effectively characterized by a group of carriers undergoing a time dependent random walk biased by an electric field. The slowly-varying time dependence of  $\psi(t)$  corresponds to a large dispersion in the hopping times. For certain  $\psi(t)$ 's the decaying photocurrent could be physically understood. At early times in the

transport process most carriers would move with the relatively-more-probable short hopping times. With increasing  $t$  all carriers would eventually encounter at least one long hopping time, where long times are analogous to deep traps, in which the carrier is immobilized temporarily. Hence as  $t \rightarrow \infty$  most carriers become immobilized and the current tends to zero. These results are at variance with those obtained considering traditional macroscopic descriptions of carrier transport, where the time interval between displacements has associated with it a narrow, or  $\delta$ -function, distribution.

The final section in this chapter will present an alternative way to view this process within the realm of a random walker on a fractal lattice.

### 6.3.3. Experimental Dark Conductivity

A third experimental area of evidence which we believe lends further support to fractal behavior is that of the dc conductivity as a function of the hydrogen content, in particular the resistive exponent  $\zeta$  or the conductivity  $\sigma$ . It is well established that with the incorporation of atomic hydrogen the dc conductivity can be reduced by several orders of magnitude, a property we have attempted to exploit in Chapter 5 for e-beam interrogated  $a-Si:H$  for archival storage. This appears to be a universal property independent of the method of preparation. Figure 6.6 illustrates this functional dependence for films prepared at 13 different laboratories and by different preparation methods [6.14]. The variance can be attributed to the method of preparation as well as to the variety of methods used for the determination of the hydrogen content. This phenomenon will be related to the quantum well model briefly discussed in Chapter 1 and to the concept of electrical transport on fractal percolating clusters.

### 6.4. Fractals and $a-Si:H$

The previous section illustrated several experimental aspects of  $a-Si:H$  which are not well explained by conventional solid state physics and in fact may best be described utilizing the concept of fractals. The first of these areas was related to the observed linear dependence of the density of states, the second to dispersive transport, and the third to the dark conductivity and its dependence on hydrogen incorporation. In this section we will attempt to present consistent arguments for the observed functional dependences from a fractal perspective.

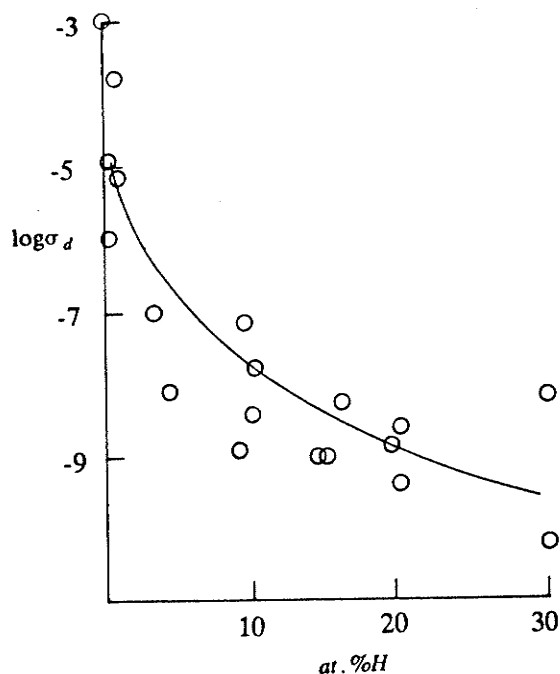


Figure 6.6: Dependence of the dc conductivity upon the incorporated  $H$  in  $a-Si:H$  alloys [6.14]

#### 6.4.1. Fractals and the DOS

It is instructive at this time to ask what type of fractal structure we are anticipating. It is quite clear we are considering non-deterministic fractals, that is ones which are generated by a stochastic rule. It should also be apparent that we are considering a network of these random fractals which, for excitations above a characteristic length  $\xi$ , the network appears homogeneous. This would be consistent with recent scattering experiments on  $NbGe_2$  thin films [6.15]. The notion of a characteristic length  $\xi$  corresponding to a Euclidean-fractal crossover is not only physically satisfying but will prove to be necessary in our discussion regarding the density of states.

At this point it is illustrative to consider why a parabolic DOS is quite often assumed when evaluating optical absorption data. Although the wave vector  $k$  is in not a good quantum number for amorphous solids due to the lack of translational invariance, it is often used as a first approximation when considering phenomena associated with extended states. This is widely accepted as the extended states in amorphous solids are considered to be derived from the extended states in crystalline solids after modifications due to

disorder. In this case, the following energy-momentum relation is often considered valid, at least for states near the bottom of the band

$$E \approx k^2 \quad (6.5)$$

It should be pointed out, however, that for states near the band edge, the deBroglie wavelength for extended states in the crystal is very long (many atomic spacings), and these states should suffer most from the loss of long-range order. If in addition to this, the density of states in reciprocal space were homogeneous in  $k$ , the integrated density of states would have the following functional dependence

$$N \approx k^3 \quad (6.6)$$

From these two relationships the number of states as a function of energy with energy between  $E$  and  $E + dE$  can be determined in the conventional picture as follows

$$D(E) = \frac{dN}{dE} = \frac{dNdk}{dkdE} \approx k \approx E^{1/2} \quad (6.7)$$

Recalling that the optical absorption coefficient ( $\alpha$ ) is determined from a convolution of the valence- and conduction-band density of states, (Eqn.6.4)

$$\alpha^{1/2} \approx E - E_{opt} \quad (6.8)$$

from which  $E_{opt}$  is extracted. It should be borne in mind that the optical gap in an amorphous solid does not represent a zero in the density of states, but rather a region of localized states. As such, these techniques are valid at best for only a limited range or window of  $\alpha$ .

#### 6.4.1.1. Accounting for the linear DOS; a $k$ -space approach

In order to account for the experimentally-observed linear density of states and linear fit to  $(\alpha h\nu)^{1/3}$  versus  $h\nu$  data, two considerations from the above analysis are suggested. (The above analysis neglected any dimensional dependences of the coefficients.) Firstly, the energy-momentum relation may not be valid, and secondly, the density of states in reciprocal space may not be uniform in our assumed amorphous fractal solid. Attention will now focus on an explanation based upon a non-uniform density of states in reciprocal space, as well as a possible non-parabolic dispersion relation. The following discussion is intended to present a perspective based on the dimensional

requirements of both  $N$  and  $E$  upon  $k$ .

If one were to assign a disturbance to the conventional dispersion relation, to a first approximation this could be represented as follows

$$E \approx k^\delta \quad (6.9)$$

where the disorder is introduced as a deviation of  $\delta$  from the parabolic case ( $\delta=2$ ). The parabolic energy-momentum relation is carried over from the free-electron model in a uniform potential. In the case of the crystal, the periodic potential perturbs the energy-momentum dispersion relation near the edges of the Brillouin zone. The perturbation creates energy gaps at the band edges, but the dispersion relation near the bottom of the band is left practically unaltered. As a first approximation to the amorphous material we will assume that disorder perturbations are on the order of interatomic distances and as such their effect will also be predominant near the band edges in  $k$  space. As the minimum of the conduction band can be located at a large value of  $k$ , one may still argue that the energy-momentum dispersion relation at least for electrons in  $a-Si:H$  may be severely altered.

Also assume that the density of states could be evaluated as before

$$D(E) = \frac{dNdk}{dkdE} \quad (6.10)$$

In keeping with a general discussion and adjustable parameters assume also that the integrated density of states  $N$  varies as  $k^\beta$ . In order to derive a linear variation in the density of states  $D(E)$  we would require

$$\frac{\beta}{\delta} - 1 = 1. \quad (6.11)$$

The solutions to this equation yield a straight line  $\beta = 2\delta$ .

Two solutions will be discussed at this point which illustrate the effect of parameters  $\delta$  and  $\beta$ . The first assumes the parabolic energy-momentum relation is still approximately valid, and the second assumes a major perturbation to the parabolic energy-momentum relation.

The first approach with  $\delta = 2$  yields a phenomena which clearly does not fall into the realm of fractal geometry, in that it requires the dimension governing  $N$  to be  $\beta = 4$ . This implies that the integrated density of states would yield a fractal dimension somewhat greater than the embedding 3-dimensional Euclidean momentum space. This difficulty may be overcome when we recall

that we are considering the dependence of  $N$  upon  $k$ ; i.e. we are in reciprocal space. One of the properties of the proposed reciprocal space is that dense regions of the original space map into sparse regions in reciprocal space. As such, if one were to consider the reciprocal space associated with a fractal cluster one could conceivably imagine being mapped into a reciprocal space with the properties required to yield a linear density of states. As an illustration of this concept, one would be required to construct a fractal cluster, in which the density decreased as the radius of gyration increased, and consider its representation in a reciprocal lattice space. A first approximation to this mathematical animal is one whose density increases as the corresponding radius of gyration increases. This immediately leads us to the recognition of the Bethe lattice [6.16] as being a representative candidate for our lattice in reciprocal space. Macroscopic homogeneity is dispensed with in this lattice; in fact, the surface density of a Bethe lattice grows without limit. This crowding problem can be alleviated, but it cannot be eliminated by setting the Bethe lattice in a space of higher dimension. Eventually the crowding problem overwhelms all available space since the number of branches grows exponentially with the radius while the available space only grows as  $r^d$ . Mathematically the Bethe lattice cannot be embedded in any finite dimensional space. This difficulty is overcome in our particular problem because the lattice is of finite extent, bounded to some degree by the reciprocal of the interatomic spacing or the reciprocal of the cluster size itself. As such, we may consider the Bethe lattice as a possible candidate for describing our non-uniform distribution of states in energy-momentum space. If we assume a Bethe lattice-like momentum space it becomes easy to derive the required linear density of states; i.e. we have some justification for expressing the integrated density of states as

$$N \approx k^4 \tag{6.12}$$

where the dimension 4 would be obtained by integrating the density of states on the Bethe lattice. This explanation would indeed yield a linear density of states as a function of energy and predict linear plots of  $\alpha^{1/3}$  versus energy in determining the optical gap. Furthermore, this Bethe reciprocal lattice space explanation may also account for, or at least be consistent, with additional experimental evidence. For example, the optical absorption coefficient is larger in the amorphous material than the crystalline material. This

phenomena has often been referred to as relaxation of the  $k$  conservation rule. The Bethe reciprocal lattice space provides an alternative perspective, namely that the arguments for crowding of electron states in  $k$  space also apply to phonon modes. The increased number of phonon modes, relative to the crystalline case with large  $k$  vectors are available to assist in the indirect optical transitions, thereby increasing the optical absorption coefficient. Physical justification for assuming that the Bethe lattice approach may be valid is therefore based upon the following two ideas: i) the amorphous material has underlying fractal structure, such that a Bethe lattice-like reciprocal lattice space is to be expected and ii) the less dense regions of reciprocal lattice space correspond to long wave-length phenomena, while the crowding at large  $k$  are associated with the existence of short range behavior or order. The Bethe lattice explanation is not intended to be rigorous, in that it is readily conceded that  $k$  is not a valid quantum number, but rather as a crude model which may provide an alternative perspective on the amorphous state. There is a host of phenomena which this simple model does not explicitly describe, in particular van Hove singularities or rather the lack of them and the isotropic behavior of the density of states. Further complications are encountered when attempting to describe the Bethe lattice for an indirect-gap amorphous semiconductor such as silicon. Recall that this discussion was an attempt to justify an apparent dimensional requirement of 4 for the reciprocal lattice space.

A second example solution still based upon our  $k$  space arguments would be to assume that the variation in  $k$  space of  $N$  is roughly that of the embedding Euclidean dimension. This assumption yields an energy-momentum relation in view of Equ.6.11 and 6.9, given by

$$E \approx k^{1.5} \tag{6.13}$$

Therefore the problem in this case becomes one of justifying a sub-parabolic energy-momentum relation. As we have discussed, the parabolic approximation is carried over from the free-electron model of an electron confined to a periodic potential. In these terms it is difficult to associate a physical rationale for a sub-parabolic dispersion relation. This point will become more evident as this section progresses.

These two example solutions underline the anticipated difficulty associated with attempting to relate fractal manifestations to concepts which presuppose translational invariance. In one case we were forced to justify a dimensional

dependence of  $N$  in reciprocal space of 4, while the other case forced us to justify a sub-parabolic dispersion relation. We have also not taken advantage of the information regarding the type of fractal we are looking for, namely a network which undergoes a Euclidean-fractal crossover. If this concept had been introduced in our  $k$  space discussion we should more appropriately have considered our Brillouin zone to be bounded by the reciprocal of our cluster size. In any event, if we stubbornly cling to the concept of a  $k$ -space with its roots in translational invariance, there appear to be several difficulties associated with applying the notion of fractals directly to the density of states in  $a-Si:H$ .

#### **6.4.12. Accounting for the linear DOS; a real space approach**

There is however an alternative path which may eliminate these difficulties. Firstly we must dispense with the notion of  $k$  space almost entirely; as we have already mentioned  $k$  is not a particularly good quantum number anyway. Secondly we borrow a second conjecture from R. Orbach based upon a phonon-fracton crossover [6.17]. Finally, we must employ some recent experimental results on the phonon density of states for  $a-Si$  [6.18]. Our approach is outlined as follows. Consider a medium which can be considered fractal below some measurement  $\xi$ .  $\xi$  is reminiscent of the correlation length in a dynamical system near a critical point. That is, for excitations whose length scale is greater than  $\xi$  the network appears uniform and can best be described in terms of the embedding Euclidean geometry. For excitations whose length scale is less than  $\xi$  the network appears fractal. This should be a more reasonable model as a starting point for correlating experimentally-observed phenomena with fractal behavior. This is because the network in this perspective is properly regarded as an interconnection of fractals whose characteristic length  $\xi$  now depends upon the amount of hydrogen incorporated into the network. This concept will also play a predominant role in the dependence of the dc conductivity and its dependence upon  $\xi$  or  $H$ . The emphasis now is not only on determining the effect of a fractal lattice but also on determining the ramifications of a fractal to homogeneous crossover. This premise led Orbach et.al. to predict an increase in the vibrational density of states due to the phonon-fracton transition. This conjecture is retained in the present work to imply an expected increase in the electronic density of states.

The discussion begins with a brief digression to the problem of a random walker confined to a fractal cluster. Gefan et.al. [6.19] have shown that for diffusion on a single cluster the mean distance traveled at time  $t$  is approximated by

$$\langle r^2(t) \rangle_s \approx t^{2/(2+\theta)} \quad (6.15)$$

where the cluster contains  $s$  sites within a linear range  $r_s \approx s^{1/\bar{d}}$ .  $\theta$  is the appropriate exponent governing the range dependence of the diffusion constant. The number of distinct sites visited is then

$$N_s(t) \approx t^{\bar{d}/(2+\theta)} \quad (6.16)$$

When the spectral dimension is  $\leq 2$  the walker is confined such that it is probable for the walker to return to the origin. The probability of remaining at the origin at time  $t$  is

$$\langle P_0(t) \rangle \approx [N_s(t)]^{-1} \approx t^{-\bar{d}/(2+\theta)} \quad (6.17)$$

When the cluster is part of an infinite network the spectral density of states is given as the Laplace transform of Equ. 6.17 and is of the form

$$N(E) \approx E^{[\bar{d}/(2+\theta)]-1} \quad (6.18)$$

which defaults to the parabolic relation when  $\bar{d}=3$  and  $\theta=0$  (the Euclidean case). Upon conversion to the vibrational density of states the spectral dimension is defined as

$$\bar{d} = 2 \frac{\bar{d}}{2+\theta} \quad (6.19)$$

The coefficient 2 was derived from the vibrational density of states where  $E$  was replaced by  $-\omega^2$  in Equ.6.18 and pre-multiplied by  $\omega$  [6.17].

Now the vibrational density of states may be expressed as

$$\rho(\omega) \approx \omega^{\bar{d}-1} \quad (6.20)$$

where for the Alexander-Orbach conjecture  $\bar{d} \approx 4/3$ . Therefore,  $\rho(\omega)$  is expected to vary as

$$\rho(\omega) \approx \omega^{1/3} \quad (6.21)$$

This relation is shown in Fig.6.7, with the normal Euclidean case shown for

reference. Upon comparison of the AO conjecture with the experimentally determined phonon density of states (PDOS) for *a-Si* [6.18], as shown in Fig.6.8, one is encouraged to suspect fractal behavior in pure *a-Si*. That is, at least for *a-Si* in the absence of hydrogen the phonon density of states does not appear to vary as  $\omega^2$ , as in the translationally-invariant crystalline case, but rather  $\rho(\omega)$  varies in an approximately linear, or even sublinear, manner. It should be mentioned that the primary region of interest to us in Fig.6.8 is the vibrational spectra below 10 meV. This presents some difficulty as there is little data available at this time for the vibrational properties of *a-Si:H* in this region.

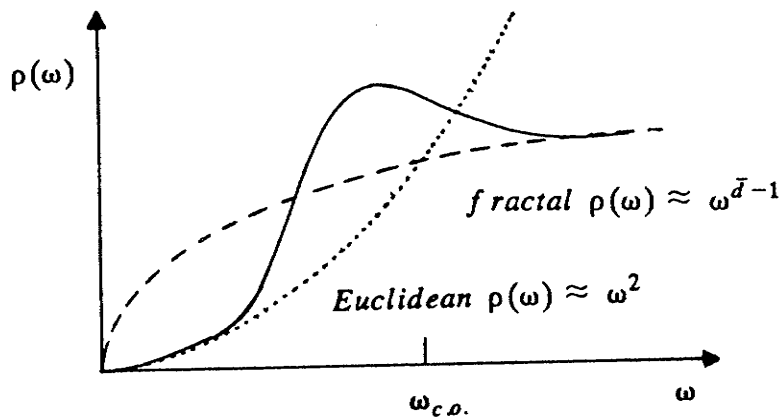


Figure 6.7: Density of vibrational states. The solid curve represents the crossover from the phonon to fracton regimes [6.17].

Orbach also considered the phonon-fracton crossover frequency and argued it to behave as  $\omega_{co} \approx \xi^{-(1-\theta/2)}$ . Near this crossover an increase in  $\rho(\omega)$  is expected to result from the normalization condition for integration over  $\omega$  which must be unity regardless of whether fractal or Euclidean. The consequences of this conjectured increase in the DOS is shown as the solid curve in Fig.6.7. Based upon Fig.6.7 and Fig.6.8 one is led to conclude that for pure *a-Si* the correlation length  $\xi$  is seen to be *quite large*, where the term quite large will be quantified presently. That is, there does not appear to be sufficient evidence of a phonon-fracton crossover in pure *a-Si:H* or it is restricted to a very small value of  $\omega$ . From Fig.6.8 if there were a phonon-fracton crossover it would have to be restricted to a value of energy  $\leq 4$  meV, where  $\xi$  would be on the order of  $\geq 40 \text{ \AA}$  [6.17]. As this does not appear to be the

case in view of the limited data available, we assume that  $\xi$  is at least  $40 \text{ \AA}$  for  $a\text{-Si}$  and probably larger, on the order of  $100 \text{ \AA}$ .

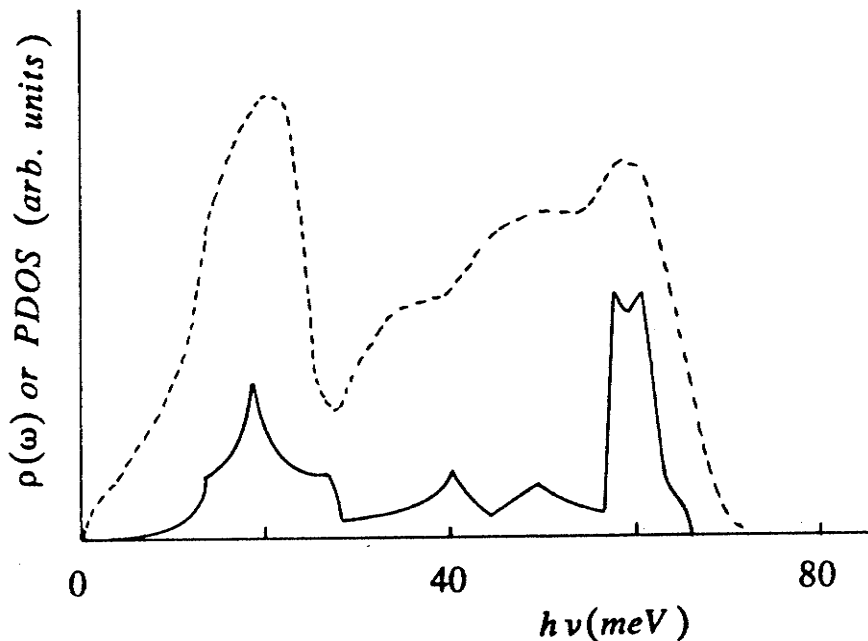


Figure 6.8: Vibrational density of states for pure  $a\text{-Si}$  [6.18].

There is one further point which should be noted at this time. If the AO conjecture ( $\bar{d} \approx 4/3$ ) is to be applied to the class of fractals corresponding to  $a\text{-Si:H}$ , the electronic density of states is expected to diverge at the origin. This is evident from Equ.6.18 and Equ.6.19, where

$$N(E) \approx E^{\frac{\bar{d}}{2}-1} \approx E^{-1/3} \quad (6.22)$$

This does not appear to be the case for pure  $a\text{-Si}$  with  $\xi \approx (100 \text{ \AA})$ . We now turn our attention to fractals for which the AO conjecture does not apply.

#### 6.4.13. Nonhomogeneous Fractals as Appropriate Representations of $a\text{-Si:H}$

Recently Leyvraz and Stanley [6.20] considered the definition of the class of fractals for which the AO conjecture applies. Their results indicate that the AO conjecture does not generally apply to non-homogeneous fractals, where the term non-homogeneous fractals refers to structures such as Sierpinski

gaskets and percolation backbones. As we are thus far uncommitted to the type of fractal structure  $a-Si$  may represent, we will present a further discussion unconstrained by the AO conjecture and attempt to present consistent arguments which as a consequence show  $a-Si:H$  to be best considered as non-homogeneous. Remember that pure  $a-Si$  has been argued to possess a correlation length  $\xi$  of approximately (100 Å). and that from Fig.6.8 and Equ.6.20  $\bar{d}$  can be deduced to be approximately 2. This leads to a constant electronic DOS

$$N(E) \approx E^{\frac{\bar{d}}{2}-1} \approx \text{constant} \quad (6.23)$$

or even a slightly divergent DOS in the fractal regime. Recall that at energies less than that corresponding to the phonon-fracton crossover one expects  $N(E)$  to vary as  $E^{1/2}$ .

Assuming now that  $\bar{d} \approx 2$ , one is led to consider consequences of relating  $\bar{d}$  to  $\bar{d}$  and  $\theta$ , where

$$\bar{d} = 2 \frac{\bar{d}}{2+\theta} \quad (6.24)$$

Now  $\bar{d} = 2+\theta$ , and as  $\bar{d}$  is to be greater than  $\bar{d}$ ,  $\theta$  is seen to be positive. We also know that if  $\bar{d}$  is to be a legitimate fractal dimension it must be less than  $d$ , where  $d$  was the dimension of the embedding Euclidean space. Now we have an indication of the fractal dimension associated with  $a-Si:H$ , namely  $2 \leq \bar{d} \leq 3$ . If one were to argue that the case where  $\bar{d} = 3$  simply corresponds to defaulting to 3-d Euclidean space, one would be forced to explain an energy-momentum dispersion relation  $E \approx k^{2+\theta}$ , where  $\theta$  would be 1 from Equ.6.24. The other extreme is bounded at  $\bar{d} = 2$  by our dimension inequality relation and our experimentally deduced value of  $\bar{d} \approx 2$  for unhydrogenated  $a-Si$ . In any event the DOS is approximately constant for energies beyond that corresponding to the crossover frequency.

Now the situation is as depicted in Fig.6.9, where the Euclidean and fractal DOS are sketched. At this time we recall the second conjecture of Orbach [6.17], which predicts an increase in the density of states at the phonon fracton crossover. This increase or bump in the DOS is expected to be near the energy corresponding to the correlation length  $\xi$  as sketched in Fig.6.10.

Theoretically this conjecture has been demonstrated by calculations based upon the effective medium approximation [6.21]. Experimentally,

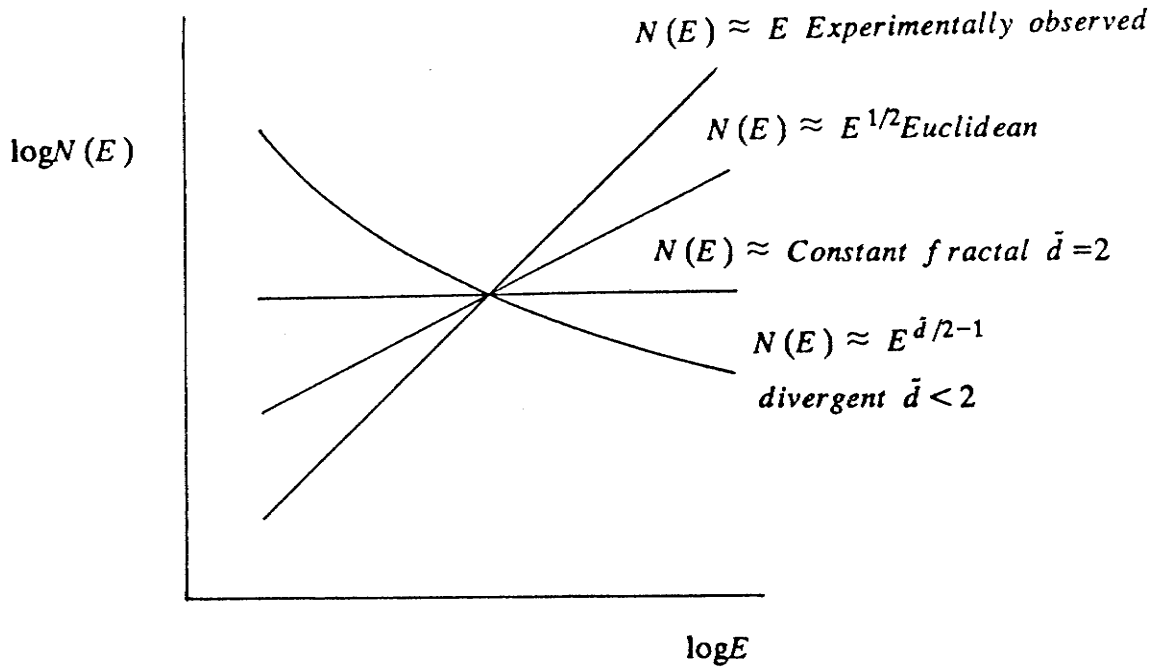


Figure 6.9:  $N(E)$  vs.  $E$  illustrating the consequences of fractal geometry.

evidence has been derived supporting this conjecture from the vibrational DOS for fused silica [6.22], this figure is reproduced in Fig.6.11. For fused silica  $\xi$  has been estimated to be approximately  $40 \text{ \AA}$ , at a crossover frequency corresponding to  $\approx 1 \text{ THz}$  or  $\approx 4 \text{ meV}$ . We believe this should also correspond at least to within an order of magnitude of where the electronic excitations should undergo an Euclidean to fractal crossover. The following discussion illustrates this point. The optical measurements as well as the inverse photo-emission experiments reveal a linear DOS for excitation energies approximately 200-400 meV above the mobility edge. Assuming that the energy of the electron is 200 meV above the bottom of the conduction-band edge, we can approximate its velocity from the crystalline case, (i.e.  $E = 1/2 m^* v^2$ ). Assuming a similar effective mass the group velocity is approximately  $5 \times 10^5 \text{ m/s}$ . Knowing the group velocity as well as the electron energy, the effective wavelength is immediate ( $\lambda \approx 100 \text{ \AA}$ ), within an order of magnitude of the experimentally-determined value for fused silica. Recall that we are attempting to explain a linear variation in the electronic DOS, and that our initial attempt utilizing fractals directly led to variations in opposition to the variations we required to explain the experimentally-observed phenomena.

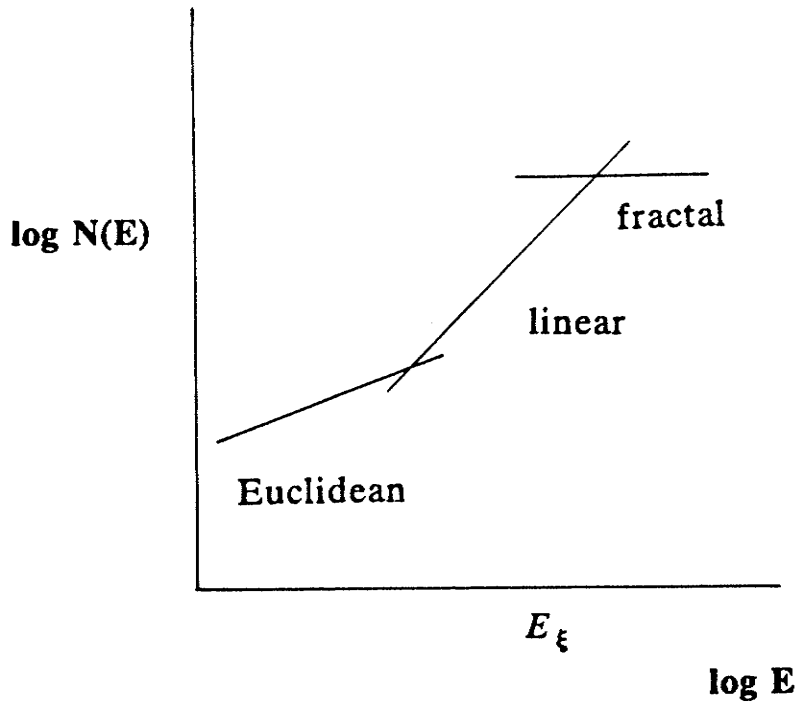


Figure 6.10: Crossover of the electronic density of states at the energy corresponding to the correlation length  $\xi$ .

From the above discussion the linear variation of electronic DOS may be seen to be a consequence of the phonon-fracton crossover, which in the case of the electronic DOS is more appropriately called an Euclidean-fractal crossover.

A question which must also be addressed is the role of hydrogen in an amorphous network from a fractal perspective. In view of the limited experimental data available at this time the following discussion is speculative, but illustrates, the direction for future research which may unravel this important question. At least two parameters can be argued to vary as with the  $H$  content,  $\xi$  and  $\bar{d}$ .

The dependence of the spectral dimension  $\bar{d}$  will also effect both  $\bar{d}$  and  $\theta$  in a similar manner to that previously discussed. The major consequence would arise from the electronic DOS ( $N(E)$ ) at large values of  $E$ , that is, for values of  $E$  corresponding to the fractal regime. In the fractal regime  $N(E)$  varies as  $\bar{d}/2-1$ , as such,  $N(E)$  in the fractal regime should yield information about  $\bar{d}$ . Figure 6.12 illustrates  $N(E)$  of  $a-Si:H$  after different annealing periods [6.9]. As it is well established that the annealing reduces the  $H$

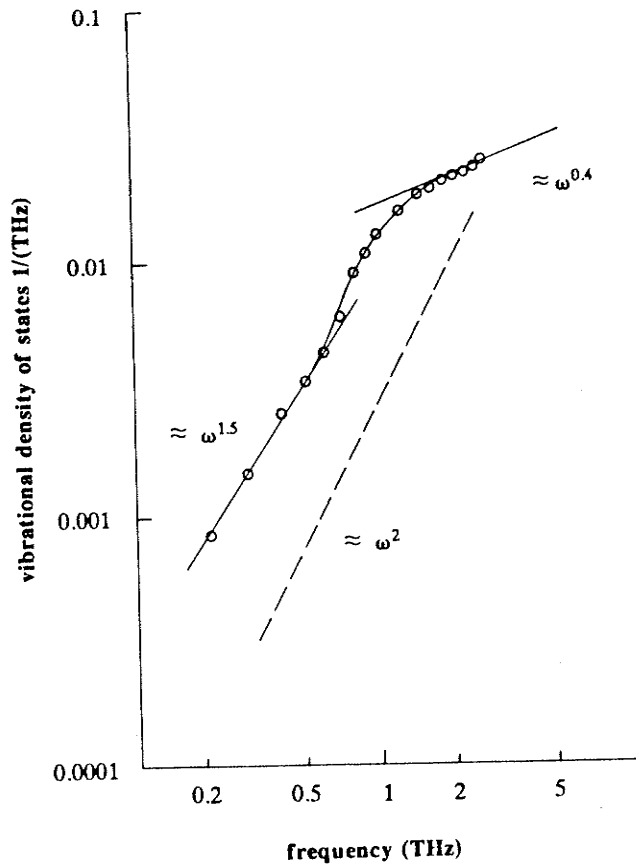


Figure 6.11: Experimentally determined vibrational density of states for fused silica [6.22].

content of the films, and from Fig.6.12 we can speculate that  $\bar{d}$  decreases with increasing  $H$  content. Therefore, from the available data (Fig.6.8 and 6.12) we are led to associate  $\bar{d} \approx 2$  for pure  $a-Si$  and a decreasing  $\bar{d}$  as  $H$  is incorporated into the network.

The correlation length  $\xi$  is also most likely  $H$  dependent, although there is limited data available at the present time to determine this dependence. As  $\xi$  is associated with a cross-over from Euclidean to fractal geometry, information regarding its dependence upon the  $H$  content can be extracted from detailed phonon DOS where the  $H$  content would be a parameter. The region of interest would be in the  $THz$  range. Although there is no experimental data for the phonon DOS available for  $a-Si:H$ , there are recent results on the partial phonon DOS for  $a-Si:H$ . These results are reproduced in Fig.6.13. As can be seen from the figure the partial phonon DOS for the  $H$  modes are between the phonon DOS for pure  $a-Si$  and the phonon DOS for  $c-Si$ . In

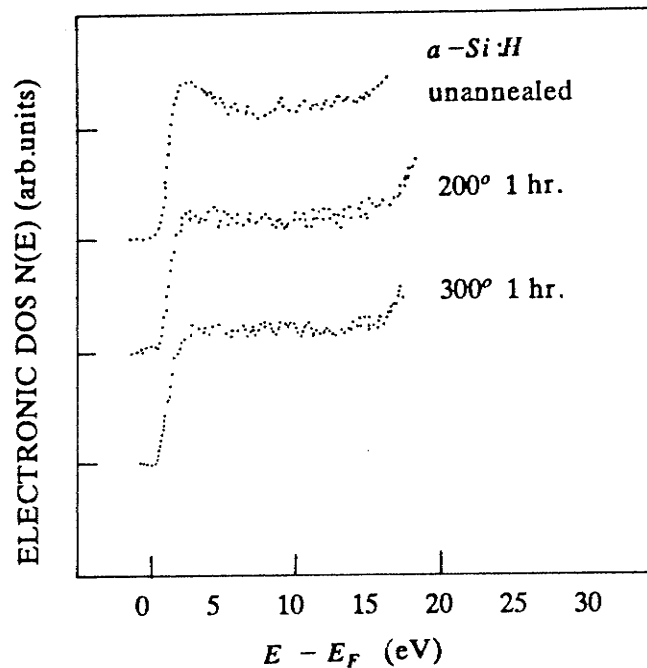


Figure 6.12: Effect of hydrogen on the electronic DOS and hence  $\bar{d}$  [6.9].

any event, the contribution to the full phonon DOS for  $a-Si:H$  can be argued to increase the dependence of the phonon DOS upon  $\omega$ , although little can be said concerning the dependence of  $\xi$  at this time.

The above discussion suggests several experimental tests for the notion of a decreasing  $\bar{d}$  with increasing  $H$  incorporation, as well as the dependence of  $\xi$  upon  $H$  incorporation, specifically determination of  $N(E)$  and  $\rho(\omega)$  as functions of hydrogen content. Combined, these experiments will also provide experimental values for  $\bar{d}$ ,  $\bar{d}$ , and  $\theta$  in the amorphous silicon network, and determine the effect of  $H$  on  $\xi$ . Difficulties associated with more detailed measurements are primarily a result of data corruption due to localized states.

In summary, we have shown in this section that the experimental data for the electron and phonon DOS in  $a-Si:H$  are consistent with an underlying fractal structure for  $a-Si:H$ . Furthermore we have shown that the increase in the DOS required to explain the experimental data can arise only as a consequence of a Euclidean-fractal crossover. In the fractal regime for pure  $a-Si$  the fracton dimension appears to be approximately 2, with the fractal dimension lying between 2 and 3. The fracton dimension is further found to

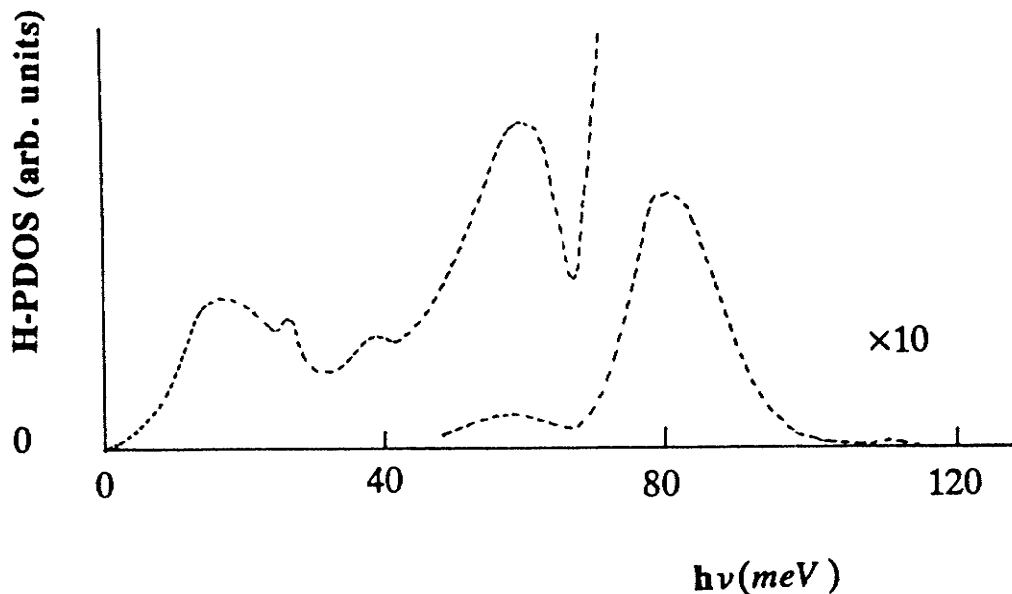


Figure 6.13: Hydrogen partial vibrational density of states for  $a-Si:H$  [6.18].

decrease as hydrogen is incorporated into the amorphous silicon network. Both the electronic and vibrational DOS is consistent with a characteristic length ( $\xi$ ) associated with the Euclidean-fractal crossover on the order of 100 Å for  $a-Si:H$ . At the present time, based upon the experimental data it is difficult to determine the dependence of  $\xi$  upon the  $H$  content.

#### 6.4.2. Fractals and Dispersive Transport

At this time another brief digression is required for the discussion of dispersive transport. The following is adapted from Mott and Davis [6.23], Scher and Montroll [6.13], Scher and Pfister [6.24], and particularly the insightful book by Zallen [6.25]. In the context of amorphous semiconductors the term dispersive transport is generally regarded as the anomalous behavior observed in transient photoconductivity or time of flight experiments. In the case of  $c-Si$  transient photoconductivity is utilized to determine the transit time and hence the drift mobility. Typically a 'sandwich' arrangement is employed in the experiments, with one electrode being semi-transparent. When arranged as shown in Fig.6.14 a), the semi-transparent electrode allows for a short pulse of strongly absorbed photons to inject carriers into the

sample in the vicinity of the electrode. Immediately after the creation of the electron hole pairs, they are pulled apart by the high field. Under conditions where the injected charge is small compared to  $C_s V$  where  $C_s$  is the sample capacitance, the internal field will remain essentially constant and the sheet of charge created will drift to the opposite electrode.

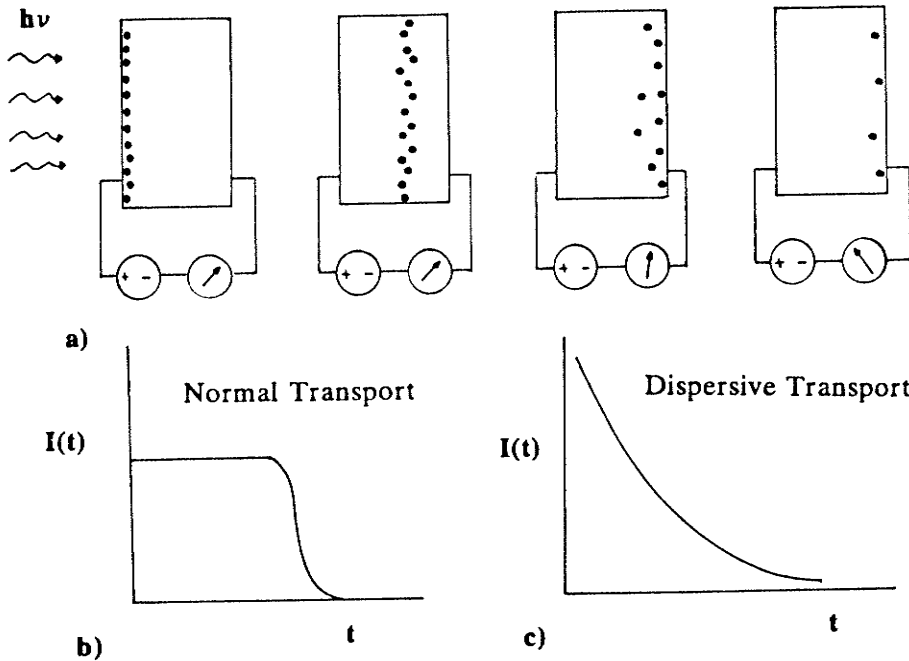


Figure 6.14: Transient photo-conductivity [6.25]. a) Experimental set-up. b) Normal transport. c) Dispersive transport.

The normally observed current transient is shown in Fig.6.14 b), the flat region corresponding to the sheet of charge moving at a constant speed across the sample yielding a constant current. Upon reaching the back electrode the current ceases. The time required to reach the back electrode is the transit time  $t_t$ , from which the mobility may be determined as

$$\mu_D = \frac{d}{F t_t} \quad (6.25)$$

where  $d$  is the sample thickness and  $F$  is the electric field. The sheet of charge is dispersed by Gaussian statistics and as such the current transient is rounded off near  $t_t$ . In many amorphous materials including  $a-Si:H$  a different shape to the current transient is observed. The current decreases

continuously and extends to very long times; that is, there is not a clear transit time  $t_t$ , as shown in Fig.6.14 c). Scher and Montroll [6.13] formulated a theory based upon transport governed by hopping between localized states, where hopping refers to phonon assisted quantum mechanical tunneling and the localized states refer to solutions to the wave equation localized to a region of space. In this case, the transit time is ill-defined and cannot be extracted from the current transient.

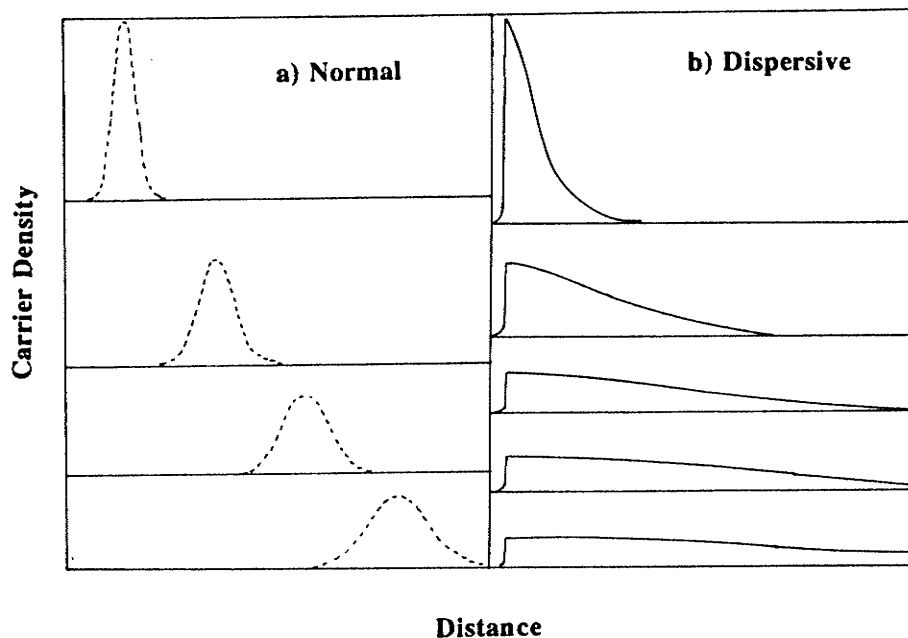


Figure 6.15: Time evolution of the charge packet or carrier density profile [6.25]. a) Normal transport. b) Dispersive transport.

In the case of normal transport as depicted in Fig.6.15 a) the sheet of charge has associated with it a Gaussian dispersion. For normal transport the mean position is denoted  $x(t)$  and varies as  $t$ , and  $\Delta x(t)$  is used to denote the spread and varies as  $t^{1/2}$ . That is,

$$x(t) \approx t \text{ and } \Delta x(t) \approx t^{1/2} \quad (6.26)$$

The linear variation of  $x(t)$  corresponds to constant drift mobility. Figure 6.15 b) corresponds to the carrier density profile for dispersive transport. According to the Scher and Montroll theory, subsequent to the strongly absorbed short light flash and charge separation, the carriers are distributed at sites with

various environments. Transport is then allowed to proceed via hopping on a random array of sites. Some of the local environments permit the immediate motion of the carriers biased by the electric field which correspond to short hops. A substantial number of the carriers however remain near the region of formation, awaiting a long hop. It is also argued that at a later time a number of the short hoppers will encounter a long hop and be delayed. If the cumulative delay time associated with these statistically fewer long hops is on the order of time required for fast carriers to traverse the sample, the anomalous properties of carrier transport are to be expected. To mathematically account for the dispersive transport, the fluctuation in hopping time was modeled as a probability function  $\psi(t)$ . Essentially we are left with a biased random walker with weighted hopping times. This was a most remarkable result, in that variations of  $\psi(t)$  mapped into physically different transport process which could all be treated within the realm of random walkers. With  $\psi(t) \approx We^{-Wt}$ , the case corresponding to an ordered system with a unique transition rate  $W$ , the spatial distribution of the carrier packet is as shown in Fig 6.15 a), corresponding to an ordered system with one unique transition. In order to model a spectrum of transition rates in a disordered system  $\psi(t)$  must be slowly varying in  $t$ . A reasonable  $\psi(t)$  was then postulated to be a normalized function with an algebraic tail

$$\psi(t) \approx t^{-(1+\alpha)}, 0 < \alpha < 1 \quad (6.27)$$

indicating an extremely long hopping-time distribution. When the inverse-power tail  $\psi(t)$  exists, a considerable number of the carriers remain at the point of formation for a long period of time. The carriers which immediately undergo fast hops will eventually become immobilized at a site awaiting a long hop, reducing their contribution to the current until they escape. The propagating packet will have the form shown in Fig.6.15 b). The peak of the Gaussian packet and the mean of the carrier distribution are located at the same position and move with the same velocity, whereas for the dispersive transport the mean carrier distribution propagates with a velocity which decreases with time as it separates from the peak which remains nearly fixed at the point of origin of the carriers. Given also that the packet spreads with the advancing mean in an identical fashion, the relations which replace Equ.6.26 are as follows for dispersive transport:

$$x(t) \approx t^\alpha \text{ and } \Delta x(t) \approx t^\alpha \quad (6.28)$$

where

$$0 < \alpha < 1 \quad (6.29)$$

In this case the current may be expressed as  $I \approx \frac{dx}{dt} \approx t^{\alpha-1}$ . As  $\alpha < 1$  the current and drift mobility are seen to decrease with time, even in the absence of an absorbing boundary. The current starts to decay prior to any carriers reaching the back contact. Asymptotically for  $x(t) \gg L$  when few carriers are left uncollected, the current has been derived by Scher and Montroll for a non-Gaussian, non-Markoffian transport process and has been shown to have the form  $I(t) \approx t^{-(1+\alpha)}$ .

One of the primary tests of this model was derived directly from the experimental data; namely, when the transient photocurrent was plotted as  $\log I - \log t$ , the slopes corresponding to the two time regimes add to -2. This has now become standard experimental practice when analysing time of flight experiments on amorphous semiconductors. The demarcation between the extrapolated linear regimes is denoted  $t_{transit}$ . For  $t < t_{transit}$  the current decays steadily as the carriers slow down due to the large spread of  $\psi(t)$ ; this implies a decreasing velocity and obviously an ill-defined mobility. For  $t > t_{transit}$ , such that a significant number of carriers have been collected at the back contact, two parallel processes cause the current to decrease: the continued reduction in the carriers' velocity, and their number decreasing with time as they are collected.

Mechanisms argued to be responsible for anomalous transport are i) extended state transport interrupted by a continuous distribution of trapping events and ii) hopping within a manifold of localized sites. These two mechanisms are completely different in that hopping enables transport whereas trapping impedes transport. In any event, both can be argued to yield a long tail to the waiting time distribution  $\psi(t)$ . As such dispersive transport does not appear to be the arena for making this distinction.

The method of analysis employed by Scher and Montroll to describe dispersive transport is called the continuous time random walk (CTRW). In effect the transport process was modeled by observations of a random walker on a regular lattice, and the disorder was emulated through the waiting time distribution  $\psi(t)$ , which for dispersive transport displayed a long-time tail. Recently Blumen et.al. [6.26] presented an alternative perspective, based upon

the realization of self-similarity and hence the use of fractal concepts.

Their procedure is to consider the walker on a deterministic fractal with fixed stepping frequencies. This methodology is dual to the CTRW, the primary difference being that on a fractal the disorder is spatially induced, whereas in the CTRW model the disorder is temporally induced. The most likely manifestation of disorder-induced phenomena involves both spatial and temporal disorder, and this is in effect what Blumen et.al.[6.26] proposed. Their work was an attempt to qualitatively identify behavior in which either temporal or spatial disorder could dominate.

The following discussion explains how the spatial and temporal disorder combine when considering transport on a deterministic fractal when a waiting time distribution is taken into account. The mean distance traveled by the walker in time  $t$  is  $\langle r^2(t) \rangle$  where

$$\langle r^2(t) \rangle = \sum_{n=0}^{\infty} \langle r_n^2 \rangle \chi_n(t) \quad (6.30)$$

where  $\langle r_n^2 \rangle$  is the average distance traveled in  $n$  steps and  $\chi(t)$  is the probability of having performed exactly  $n$  steps in time  $t$ . For fractals  $\langle r_n^2 \rangle$  is averaged over all starting points and over all directions of the individual steps. It is well established that  $\langle r_n^2 \rangle \approx n^{\tilde{d}/\bar{d}}$  where  $\bar{d}$  is the fractal (Hausdorff) and  $\tilde{d}$  is the spectral (fracton) dimension. The probability  $\chi_n(t)$  and  $\psi(t)$  (the waiting time distribution) are related via their Laplace transforms [6.27]

$$L[\chi_n(t)] = \chi_n(u) = [\psi(u)]^n \frac{[1-\psi(u)]}{u} \quad (6.31)$$

therefore

$$L[\langle r^2(t) \rangle] = \langle r^2(u) \rangle = [1-\psi(u)]u^{-1} \sum_{n=0}^{\infty} n^\gamma [\psi(u)]^n \quad (6.32)$$

where  $\gamma = \tilde{d}/\bar{d}$ . The deterministic fractal called the Sierpinski gasket has an analytical form for both  $\bar{d}$  and  $\tilde{d}$ . The fractal dimension as we have seen has  $\bar{d} = \ln(d+1)/\ln 2$  whereas the spectral dimension  $\tilde{d} = 2\ln(d+1)/\ln(d+3)$ , where  $d$  is the dimension of the embedding Euclidean space. Since  $\tilde{d} \leq \bar{d}$ ,  $\gamma \leq 1$ , recalling that for regular lattices  $d = \bar{d} = \tilde{d}$  and  $\gamma = 1$ . Blumen et.al. derived the long time behavior of  $\langle r^2(t) \rangle$  by evaluating the Laplace transform as  $u \rightarrow 0$ . If the first moment  $\tau_1$  of  $\psi(t)$  is finite

$$\tau_1 = \int_0^{\infty} \psi(t) t dt \quad (6.33)$$

then  $\psi(u) \approx 1 - \tau_1 \mu$  for small  $u$ , from which

$$\begin{aligned} L[\langle r^2(t) \rangle] &= \tau_1 \sum_{n=0}^{\infty} n^\gamma [\psi(u)]^n \approx \tau_1 \int_0^{\infty} x^\gamma e^{x \ln \psi(u)} dx \\ &\approx \tau_1 \Gamma(\gamma+1) (-\ln \psi(u))^{-\gamma-1} \end{aligned} \quad (6.34)$$

Examples where the first moment of  $\psi(t)$  are valid are waiting time distributions associated with a single trap level, such that,  $\psi(t) = \tau_1^{-1} \exp(-t/\tau_1)$ . Utilizing the following Tauberian theorem [6.13]

**Theorem 6.1:** If  $f(u) \approx Au^{-k}$  as  $u \rightarrow 0$  with  $k > 0$ , then  $g(t) \approx At^{k-1}/\Gamma(k)$  as  $t \rightarrow \infty$ , when  $L[g(t)] = f(u)$ ,  $A$  being a constant.

the variation in the mean distance traveled is obtained as

$$\langle r^2(t) \rangle \approx \left(\frac{t}{\tau_1}\right)^\gamma \quad (6.35)$$

where  $\gamma = \bar{d}/\bar{d}$ . The corresponding current is derived immediately as

$$I \approx \left(\frac{t}{\tau_1}\right)^{-(1-\gamma)} \quad (6.36)$$

identical to that derived by Scher and Montrol for a long tail waiting time distribution on a regular lattice.

When a waiting time distribution with a long tail such as

$$\psi(t) \approx t^{-1-\alpha}, \quad 0 < \alpha < 1 \quad (6.37)$$

is incorporated into the discussion of the fractal lattice, the first moment  $\tau_1$  no longer exists and for small  $u$

$$\psi(u) \approx 1 - \Gamma(1-\alpha) u^\alpha / \alpha \quad (6.38)$$

such that

$$\langle r^2(t) \rangle \approx t^{\alpha\gamma} \quad (6.39)$$

from which the results for current are again immediate and again consistent

with experimental observations.

Equation 6.39 indicates that  $\alpha$  and  $\gamma$  combine multiplicatively, and since both are less than unity so is the product. It is also evident that many combinations of temporal and spatial coefficients yield degenerate products. As such the diffusion coefficient  $D(t) \approx t^{\alpha\gamma-1}$  is not an accurate criterion for the determination of disorder. In any event, this section has indicated that an explanation based upon fractals is consistent with experimentally observed anomalous transport in  $a-Si:H$ . Blumen et.al. [6.26] have also indicated that an occupation function may well be a better criterion for assessing the contribution of either spatial or temporal disorder.

This section has demonstrated how experimentally observed dispersive transport in  $a-Si:H$  can be qualitatively understood in terms of fractal phenomena. Several additional points are in order at this time: i) in general hole transport in  $a-Si:H$  is dispersive while electron transport is usually dispersive only below room temperature; ii) the dispersive nature of the electron transport appears to be dependent upon the fabrication process; iii) the data available from the literature has associated with it considerable scatter and; iv) the dispersion parameter is in general unequal in the two conduction regimes and is temperature dependent. These inconsistencies with simple theory have been attributed to: i) poor uniformity of the electric field in the samples caused by a non-uniform density of states in the gap; ii) neglect of energy and field dependences associated with trap capture cross-sections, and iii) oversimplified assumptions for the trap distribution. Clearly the experimental results reflect the insufficiency of the simplified theories at least for  $a-Si:H$ . The difficulties encountered with a simplified theory based solely upon temporal disorder lend support to the argument for incorporating a fractal perspective based upon spatial disorder. In conclusion we have shown in this section that not only is the temporal parameter  $\alpha$  important for describing dispersive transport, but that attention to the spatial disorder parameter  $\gamma$  is also required for a more complete understanding of transport in  $a-Si:H$ . To the best of our knowledge this is the first time the spatial disorder parameter has been discussed in connection with  $a-Si:H$ .

### 6.4.3. Fractals and the dc conductivity

This section considers the explanation of the dc conductivity within the realm of fractals and in particular of percolation phenomena. A brief digression will again precede the more specific discussion regarding  $a-Si:H$ .

The virtue of the percolation model lies in being able to analyze severely disordered systems in a very simple manner. The percolation model has been applied to a wide variety of problems; these include electronic conduction and magnetism where at the *percolation threshold* the system undergoes either a first or second order phase transition. Underlying the concept of percolation theory is the ability to vary the degree of the interconnections present in either an ordered or disordered system. Classically, percolation theory provides one with a sharp transition at which the long-range connectivity either appears or disappears depending upon how one approaches the percolation threshold.

One of the best illustrative examples of percolation theory is the example of the *vandalized grid* [6.25]. In this classic example a crazed saboteur armed with wire-cutters randomly cuts the links of a communication graph as sketched in Fig.6.16. The percolation model predicts a threshold at which the long-range connectivity disappears. Intuitively one would expect this threshold to be when the saboteur has cut approximately 50% of the links. At this time we would question the virtue of utilizing percolation theory when our guess was quite accurate. This also happens to be the only example where our intuition would yield the correct answer, and the virtue of the percolation model remains unscathed. If the saboteur were to remove the nodes associated with the bonds he would only be required to remove 41% of them before the communication network would fall apart.

A more appropriate illustration for our purposes is to interpret the communication graph as an electrical network where the intact bonds are conductors and present a low impedance path for conduction, while the broken bonds are, conversely, high impedance paths as seen by the carriers. As the bonds are cut in a random fashion the current decreases as shown in Fig.6.17. Denoting the fraction of uncut bonds as  $p$  and the corresponding current as  $I(p)$ ,  $I(p)$  is seen to decrease with decreasing  $p$ .  $I(p)$  continues to decrease until a critical bond concentration is reached, denoted  $p_c$ , at which point  $I(p) = 0$ . For  $p < p_c$  there is no current path and  $I(p)$  remains identically zero. This model for electrical conduction is useful for the analysis of transport in amorphous semiconductors, and looks particularly promising for

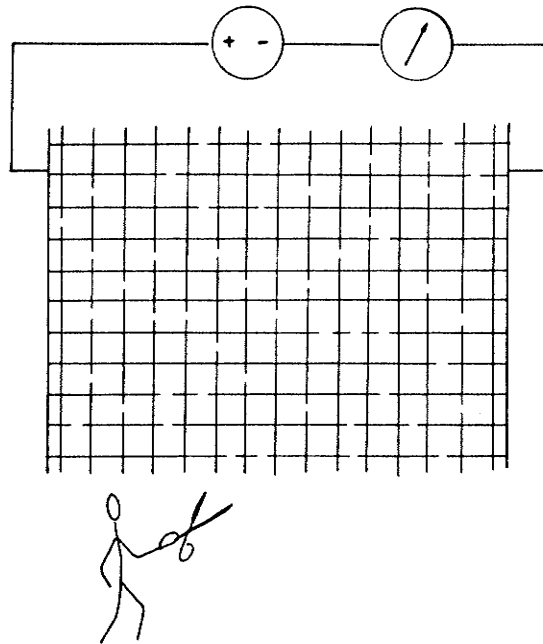


Figure 6.16: The Vandalized Grid [6.25].

describing transport in a  $-Si:H$ , where decreasing  $p$  above  $p_c$  is analogous to increasing the hydrogen concentration. Physically, the Si-H bonds are stronger than the Si-Si bonds; therefore, associated with the Si-H bonds are large potential fluctuations in both the valence- and conduction-bands. For the case of electron transport the potential fluctuations represent a large barrier or impedance effectively reducing the conductivity. As more hydrogen is introduced into the network the electron sees more potential barriers and as a consequence the conductivity decreases.

There are several other very interesting phenomena associated with the percolation model; these are particularly well presented by Zallen [6.25]. The following discussion will briefly outline the four most fundamental, of which two are directly relevant to our discussion regarding a  $-Si:H$ .

#### 6.4.3.1. $P(p)$ ; The percolation probability

Above the percolation threshold there exists an infinite cluster of connected sites or bonds. The percolation probability  $P(p)$  is the probability associated with randomly choosing a site or bond which belongs to the infinite cluster.  $P(p)$  is identically zero for  $p < p_c$  and remains identically zero until

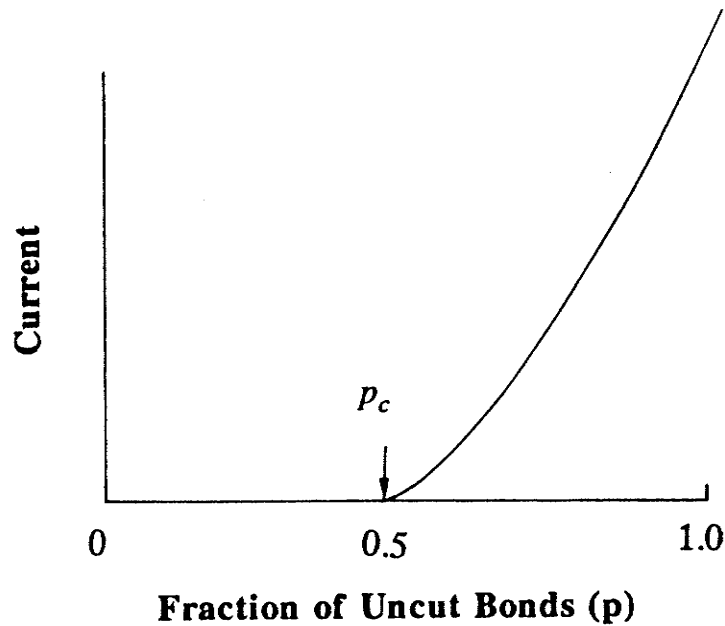


Figure 6.17: The conductance parameter in the percolation model.

the concentration of connections reaches  $p_c$ . At  $p_c$ ,  $dP(p)/dp$  becomes infinite; eventually as  $p \rightarrow 1$ ,  $P(p)$  approaches  $p$ . This is a consequence of the infinite cluster swallowing up the finite clusters. The explosive growth of  $P(p)$  illustrates the way finite clusters link up to the infinite cluster of the percolation path. Since the newly acquired finite cluster is now part of the infinite cluster it also contributes to  $P(p)$ . The behavior of  $P(p)$  as a function of  $p$  is sketched in Fig.6.18.  $P(p)$  is analogous to spontaneous magnetization observed when the temperature falls below a critical value. At criticality  $P(p)$  scales with a lattice independent critical exponent.

#### 6.4.3.2. $\sigma(p)$ ; The conductivity

$\sigma(p)$  reflects the macroscopic conductivity of our random resistor network. Below  $p_c$ ,  $\sigma(p)$  is identically zero. As  $p$  passes through  $p_c$ ,  $\sigma(p)$  gradually increases, unlike the behavior of  $P(p)$ . That is to say,  $d\sigma(p)/dp = 0$  at  $p = p_c$ . Physically this is easy to understand; the new clusters which are linked to the infinite cluster just above  $p_c$  contribute directly to  $P(p)$ , i.e. all the bonds or sites from the finite cluster now are part of the infinite cluster. Not all of these bonds or sites will be capable of carrying current; as such they do not

contribute to  $\sigma(p)$ . As  $p$  increases beyond  $p_c$  so does the portion of the percolation path capable of carrying current, and as  $p \rightarrow 1$  all portions of the percolation path contribute. The conductivity  $\sigma(p)$  is shown in Fig.6.18. An analog of the conductivity is the elastic constant for a mechanical grid. The percolation path capable of carrying current at  $p = p_c$  is called the *backbone*. This backbone is extremely torturous, and as a result of this tenuous nature the backbone at  $p_c$  has associated with it a fractal dimension. This fractal dimension is somewhat less than the dimension of the percolation lattice. One additional feature to mention about  $\sigma(p)$  is that it is also controlled by a critical exponent near threshold.

#### 6.4.3.3. $s_{av}$ ; The mean cluster size

The cluster size distribution, usually expressed as a discrete function, is defined as the number of clusters of size  $s$ . The mean cluster size is denoted  $s_{av}$  and grows as  $p$  is increased from 0 to  $p_c$ .  $s_{av}$  is initially unity as singlets account for the majority of the finite clusters. As  $p$  increases larger finite clusters are formed and  $s_{av}$  increases. At criticality  $s_{av}$  diverges as a consequence of the presence of the infinite cluster as shown in Fig.6.18. An analog of the mean cluster size is the magnetic susceptibility. Of additional interest is that at the percolation threshold  $s_{av}$  also scales with a critical exponent.

#### 6.4.3.4. $l_{av}$ ; The characteristic length

The characteristic length  $l_{av}$  is the average spanning length of the finite clusters, and is usually defined below  $p_c$ . The quantity  $l_{av}$  is analogous to the correlation length in phase transitions.  $l_{av}$  describes the geometric growth of the clusters below threshold. Above threshold, strictly speaking  $l_{av} = \infty$ , although above  $p_c$ ,  $l_{av}$  is sometimes used to characterize the clusters that do not belong to the infinite cluster. As the large finite clusters are more readily consumed by the infinite cluster,  $l_{av}$  above the percolation threshold mirrors  $l_{av}$  below threshold. One of the most important and striking aspects considering the number of sites or bonds as a function of the clusters length is that these two parameters do not scale as the dimension of the percolation problem, i.e. they are fractals! Again we see that  $l_{av}$  scales with a critical exponent near threshold. At criticality  $l_{av}$  diverges as a consequence of the formation of the infinite cluster as shown in Fig.6.18.

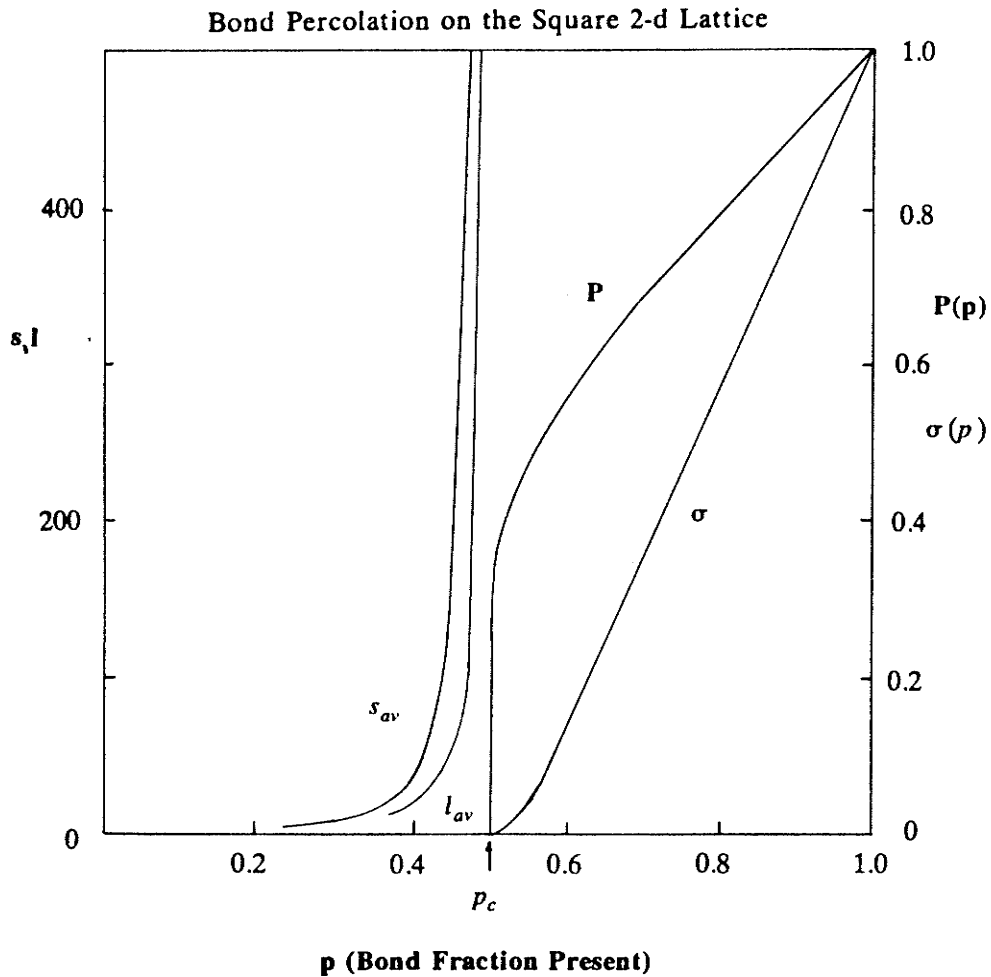


Figure 6.18: Behavior of the characteristic parameters associated with the percolation model;  $s_{av}$ ,  $l_{av}$ ,  $\sigma(p)$ ,  $P(p)$  [6.25].

#### 6.4.3.5. Percolation and a-Si:H

The percolation model appears well suited to *a-Si:H* semiconductors, in that the hydrogen can be viewed as inducing the removal of available conduction paths. Since we are also attempting to classify *a-Si:H* as a network which undergoes a Euclidean-fractal crossover, the percolation model with its fractal dimension finite clusters supports this notion. The support for this lies in experimental results, which for the most part are computer simulation studies. These studies relate the number of sites to the length of finite clusters through a fractal dimension below threshold, while just above threshold this

disparity vanishes as the fractal dimension collapses to the underlying Euclidean dimension. Of the 4 quantities which are most often associated with percolation theory,  $\sigma$  has the most significance when considering transport in  $a-Si:H$ . Recall that based upon experimental results and our discussion regarding the electronic density of states, it was difficult to determine the  $H$  dependence of the correlation length ( $\xi$ ). Directly applying the percolation model we are led to associate increasing hydrogen with decreasing  $p$ . This is based upon relating  $\sigma$  to both  $p$  and hydrogen content. With this correspondence made, we now consider the effect of hydrogen content upon the correlation length  $\xi$ , or equivalently upon the crossover frequency  $\omega_{co}$ . As there is a non-zero conductivity, we are in the regime  $p > p_c$ . Under these conditions  $I_{av}$ , the average size cluster i.e. those not already consumed by the infinite cluster, decreases with increasing hydrogen content. In this case the crossover frequency  $\omega_{co}$  is proportional to  $p - p_c$  [6.21], or inversely to the hydrogen content. As the crossover frequency is also inversely proportional to the correlation length, it follows that the correlation length is proportional to the hydrogen content. Therefore, we conclude that the correlation length  $\xi$  scales with the hydrogen content. If in the future the experimental evidence indicates that the correlation length varies in an inverse manner with the hydrogen content, the basic percolation model would have to be modified. A suggested modification would be as follows.

The alternative explanation is based upon the following: i)  $p_c$  is not well defined for  $\sigma$ , in that the presence or absence of the bonds do not reflect impedances of 0 and  $R_2$ , but rather impedances  $R_1$  and  $R_2$ ; ii)  $p_c$  is not well defined for  $I_{av}$ , in that the finite clusters are highly ramified, and as such those that are loosely coupled to the infinite cluster should in fact also contribute to  $I_{av}$ ; and iii) the percolation threshold  $p_c$  has a distinct value for both the onset of conduction as well as the divergence of the average cluster size. Based upon these ideas we argue that: i)  $p_c$  is decreased for  $\sigma$ , in that conduction can still take place even before an infinite cluster of low impedance bonds are formed and; ii)  $p_c$  is effectively increased for  $I_{av}$ , in that the clusters loosely coupled to the infinite cluster are now also included in the calculation of  $I_{av}$ . These concepts are shown in Fig.6.19. Now if we associate increasing hydrogen with decreasing  $p$ , and confine our region of interest between the threshold for  $\sigma$  and the threshold for  $I_{av}$ , the correlation length decreases with an increasing hydrogen content.

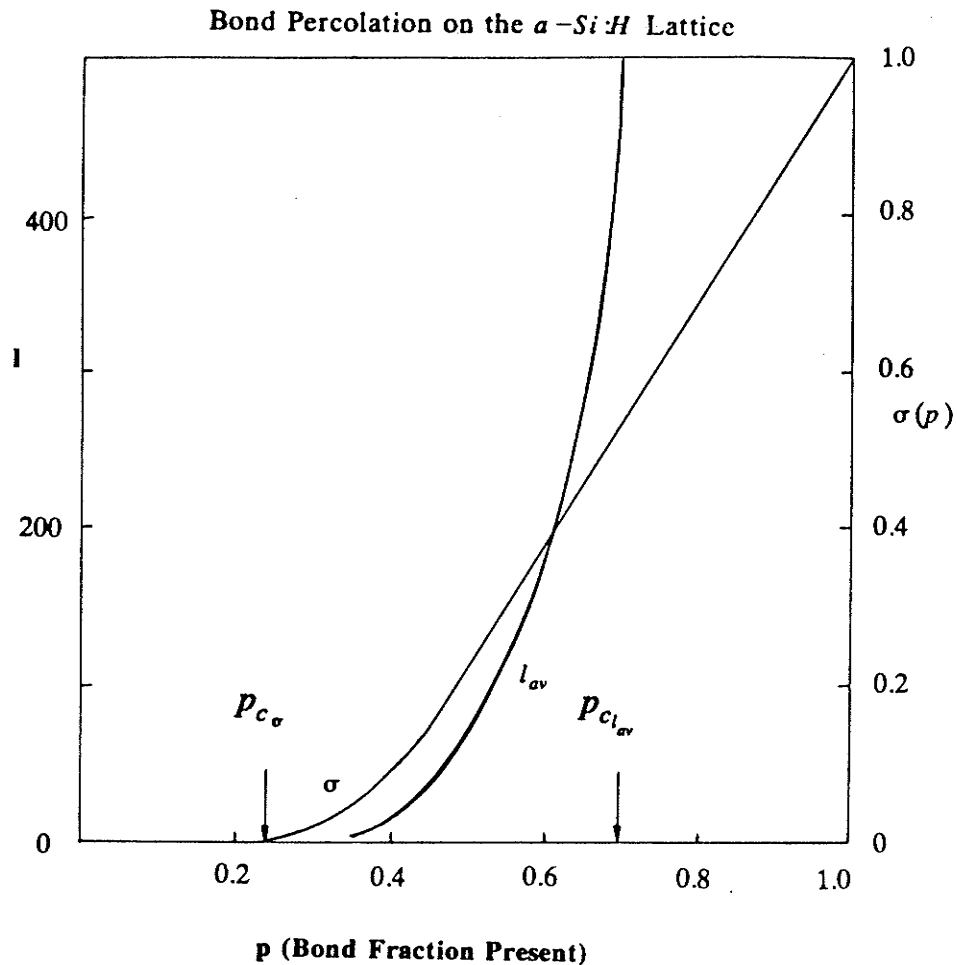


Figure 6.19: The modified percolation model for  $a-Si:H$

In conclusion, we have shown in this section that the dc conductivity of  $a-Si:H$  maps well into a percolation problem. The percolation model has associated with it a Euclidean-fractal crossover consistent with the type of structure we were looking for. Directly applying the percolation model one is led to conclude that as a higher degree of hydrogen is incorporated into the amorphous network the correlation length governing the Euclidean-fractal crossover is found to increase. These findings are yet to be borne out by experiment. If the experimental results are found to be at variance with the predictions of the direct percolation model a modified percolation model was suggested to account for the variance. The modifications were based upon

associating finite impedances with the presence or absence of bonds, and associating a degree of coupling between the newly acquired finite clusters and the infinite cluster. These modifications led to associating distinct percolation thresholds for both  $\sigma$  and  $I_{av}$ . We did not discuss cluster growth methods but suspect a variation of multi-particle diffusion limited aggregation.

## 6.5. Conclusions of Chapter 6

We have shown in this Chapter that  $a-Si:H$  can be described in terms of fractal geometry. We have presented an alternative perspective for the understanding of physical phenomena not well described by methods based upon translational invariance. The anomalous photo-conductivity suggested that spatial disorder associated with a fractal lattice should also be incorporated in future studies. The experimentally observed linear variation in the density of electronic states indicated that, if fractal geometry were to play a role in describing  $a-Si:H$ , the presence of a Euclidean-fractal crossover was required. Based upon these ideas the percolation model was introduced which not only supported the experimentally observed dc conductivity, but also supported the notion of a Euclidean-fractal crossover. We have attempted to illustrate several of the areas which must be addressed if fractal geometry is to play a role in describing  $a-Si:H$ . We have also tried to provide a forum for further discussion relating fractals to actual materials such as  $a-Si:H$ . In summary, we have drawn attention to some of the most compelling consequences of disorder which must be addressed by any theory which attempts to describe hydrogenated amorphous silicon.

## 6.6. References for Chapter 6

- [6.1] B. Mandelbrot, *The Fractal Nature of Geometry*, W.H. Freeman, San Francisco, (1982).
- [6.2] S. Havlin, D. Ben-Avraham and D. Movshovitz, *Phys. Rev. Lett.* 51, 2347 (1983).
- [6.3] T.A. Witten and L.M. Saunders, *Phys. Rev. Lett.*, 47, 1400 (1981).
- [6.4] Y. Termonia, *J. Stat. Phys.*, 36, 1356 (1984).
- [6.5] L. Niemeyer, L. Pietronero and H.J. Wiesmann, *Phys. Rev. Lett.* 52, 1033 (1984).
- [6.6] H.E. Stanley, *J. Stat. Phys.*, 36, 843 (1984).
- [6.7] S. Alexander and R. Orbach, *J. Physique*, L43, 625 (1982).
- [6.8] R.F. Voss and M. Tomkiewicz, *J. Electrochem. Soc.*, 132, 371 (1985).
- [6.9] W.B. Jackson, S.J. Oh, C.C. Tsai and J.W. Allen, *Phys. Rev. Lett.*, 53, 1481 (1984).
- [6.10] J. Reichardt, L. Ley and R.L. Johnson, *Non-Cryst. Solids*, 59&60, 329 (1983).
- [6.11] R.H. Klazes, M.H.L.M. van den Broek, J. Brezemor and S. Radelaar *Philos. Mag. B*, 45, 377 (1982).
- [6.12] J. Shirafuji and Y. Inuishi, *Amorphous Semiconductor Technologies and Devices*, Y. Hamakawa (ed.), 6, 47 (1983).
- [6.13] H. Scher and E.W. Montroll, *Phys. Rev. B.*, 12, 2455 (1975).
- [6.14] R.D. McLeod, W. Pries and H.C. Card, in preparation.
- [6.15] W.T. Elam, S.A. Wolf, J. Sprague, D.U. Gubser, D. Van Vechten, G.L. Barz and P. Meakin, *Phys. Rev. Lett.*, 54, 701 (1985).
- [6.16] J.D. Joannopoulos and M.L. Cohen, in *Solid State Physics: Advances in Research and Applications*, H.E. Ehrenreich, F. Seitz and D. Turnbull (Academic Press, N.Y., 1976), vol. 31.
- [6.17] R. Orbach, preprint from Proc. of NATO Advanced Study Inst. on Scaling Phen. in Disordered Systems (Geilo, Norway, April 1985).
- [6.18] W.A. Kamitakahara, H.R. Shanks, J.F. McClelland, U. Buchanan, F. Gompf and L. Pintschovius, *Phys. Rev. Lett.*, 52, 644 (1984).

- [6.19] Y. Gefen, A. Aharony and S. Alexander, Phys. Rev. Lett., 50, 77 (1983).
- [6.20] F. Leyvraz and H.E. Stanley, Phys. Rev. Lett., 51, 2048 (1983).
- [6.21] B. Derrida, R. Orbach, Kin-Wah Yu, Phys. Rev. B., 29, 6645 (1984).
- [6.22] A.F. Ioffe and A.R. Regel Prog. Semicond. 4, 237 (1960) replotted in [6.17].
- [6.23] N.F. Mott and E.A. Davis, *Electronic Processes in Non-Crystalline Materials*, (2nd. ed. Clarendon Press, Oxford, 1979).
- [6.24] G. Pfister and H. Scher, Phys. Rev. B., 15, 2062 (1977).
- [6.25] R. Zallen, *The Physics of Amorphous Solids*, (Wiley, New York 1983).
- [6.26] A. Blumen, J. Klafter and G. Zumofen, Phys. Rev. B., 27, 3429 (1983).

# CHAPTER 7

## CONCLUSIONS

Although detailed conclusions are presented at the end of each chapter, Chapter 7 will delineate the most important findings of the overall study.

In Chapter 2 we presented a study of the effect of incorporation of nitrogen into the  $a-Si:H$  network. Nitrogen did not act as a donor impurity and is most probably trivalently bonded in the network. The photoconductivity to dark conductivity ratio is improved by nitrogen incorporation but to a lesser extent than when both nitrogen and weak boron doping are present. The material is rapidly developing into a thin film suitable for xerography as the improved photo- to dark conductivity ratio is primarily a result of a decreased dark conductivity.

In Chapter 3 we presented a study of  $a-Si:H$  fabricated by microwave glow discharge. The primary results of that work demonstrated that microwave plasma processing for the fabrication of  $a-Si:H$  thin films presents a viable alternative to conventional rf plasma processing techniques. The development of the deposition system included magnetic confinement of the plasma, which allowed the exploitation of plasma processing under conditions of electron cyclotron resonance; specifically the power requirements were reduced by an order of magnitude as compared to non-resonant plasmas. The variation of the magnetic field confinement manifested itself in a transition from microcrystalline to an amorphous structure for the thin films fabricated under conditions described in the text. The microwave plasma processing system has application in both thin film deposition as well as reactive-ion-etching.

In Chapter 4 we presented a study of  $a-Si:H$  fabricated by electron beam evaporation. Hydrogen incorporation was facilitated by evaporation under high partial pressures of  $H_2$ . To further facilitate the incorporation of atomic hydrogen a probe was placed in the reaction zone which drew primary and secondary electrons into the reaction zone in an attempt to ionize and dissociate the molecular hydrogen. The system was moderately successful and demonstrated that the electron beam evaporation system may be a viable system if hydrogen could be more effectively incorporated into the  $a-Si$  network.

In Chapter 5 we presented a study of  $a-Si:H$  as an alternative material for archival storage. The material is found to be well suited for both optical and electron beam interrogated systems. The differentiation between a stored 0 or 1 is a result of either a change in the absorption coefficient and hence reflectivity or the conductivity which accompanies the concomitant evolution of hydrogen as a result of either laser or electron beam processing.

In Chapter 6 we presented a discussion of fractal geometry as an alternative or complementary perspective for the study of disordered systems, in particular of  $a-Si:H$ . We have shown that  $a-Si:H$  can be described in terms of fractal geometry. We have presented an alternative perspective for the understanding of physical phenomena not well described by methods based upon translational invariance. The anomalous photo-conductivity suggested that spatial disorder associated with a fractal lattice should also be incorporated in future studies. The experimentally observed linear variation in the density of electronic states indicated that, if fractal geometry were to play a role in describing  $a-Si:H$ , the presence of a Euclidean-fractal crossover was required. Based upon these ideas the percolation model was introduced which not only supported the experimentally observed dc conductivity, but also supported the notion of a Euclidean-fractal crossover. We have attempted to illustrate several of the areas which must be addressed if fractal geometry is to play a role in describing  $a-Si:H$ . We have also tried to provide a forum for further discussion relating fractals to actual materials such as  $a-Si:H$ . In summary, we have drawn attention to some of the most compelling consequences of disorder which must be addressed by any theory which attempts to describe hydrogenated amorphous silicon.